Topological bifurcations in fluid flows with application to boundary layer eruption, vortex pair interactions and exotic wakes

Nielsen, Anne Ryelund

Publication date:
2021

Document Version
Publisher's PDF, also known as Version of record

Topological bifurcations in fluid flows with application to boundary layer eruption, vortex pair interactions and exotic wakes

Anne Ryelund Nielsen

Kongens Lyngby 2021

Technical University of Denmark
Department of Applied Mathematics and Computer Science
Richard Petersens Plads, building 324,
2800 Kongens Lyngby, Denmark
Phone +45 4525 3031
compute@compute.dtu.dk
www.compute.dtu.dk

Summary (English)

The overall goal of this thesis is to introduce a systematic approach for analysing spatial structures in fluid dynamical problems. The approach describes how to interpret a flow that is already known from experiments or from solving Navier-Stokes equations analytically or numerically. In other words, we introduce a detailed method for post-processing of velocity or vorticity fields. A natural starting point for the analysis of a fluid dynamical problem is to make it clear what parameters the problem depends on. Under variation of these external parameters, a flow may undergo some qualitative changes. In this thesis, we analyse such qualitative changes with tools from bifurcation theory. We mainly focus on describing the flow structure based on the vortices that are present in the fluid. In this context, a qualitative change in the flow occurs when a new vortex is created or destroyed. We apply some well known results from the field of topological fluid dynamics to analyse the changes in the topology of the vorticity field - more specifically, we analyse the creation and destruction of extremal points of vorticity, which we consider to be feature points for vortices. Furthermore, we ask ourselves how the framework we know from topological fluid dynamics can be extended to deal with topological changes of other quantities describing the structure of a flow.

As an example of a different quantity describing the flow structure, we consider the regions of a fluid where the rotation dominates the strain. These regions are by the Q-criterion defined as vortices [29]. Since the Q-vortex is defined as a region instead of a critical point, the framework we know from topological fluid dynamics can not be directly applied. In this thesis, we extend the framework by continuing the development of a complete bifurcation theory for Q-vortices. The theory describes the qualitative changes that may occur when we allow several parameters to vary. In addition, we analyse a special bifurcation that occurs only in a flow with a line of symmetry. All our theoretical results are topological in nature, meaning that we do not distinguish between vortex patterns which

can be continuously deformed into each other.

The thesis is built around three specific case studies, in which we analyse three classical fluid mechanical problems using bifurcation theory. In all three cases, the dynamics of the vortices are simulated on a computer and we obtain a very accurate description of the flow. The bifurcation theory we develop in this thesis provides a list of possible vortex bifurcation events. The individual bifurcation events are analysed along the way when they are observed in one of the three case studies. The application of our theoretical results leads to the following main insights into the case studies:

Case I. A vortex convected close to a no-slip wall induces a viscous response from the boundary layer. The boundary layer may organise itself into secondary vortex structures which may erupt from the wall. We study this phenomenon in two dimensions and show that the eruption process can be described as a sequence of four possible bifurcations of vortices defined by the Q-criterion. Furthermore, we show that most of these bifurcation events appear to be very robust to variations in the Reynolds number.

Case II. When several vortices are present in a flow at the same time, they will naturally interact with each other. We study the simplest possible case where two vortices interact in a two dimensional flow. By applying the Q-criterion, we show that two co-rotating vortices merge only if their relative strength ratio is below a certain threshold. Furthermore, we show that this threshold can be identified as a bifurcation phenomenon itself. Finally, we show that for sufficiently small Reynolds numbers, the so-called core growth model can be used instead of Navier-stokes simulations as a simple, analytically tractable model with low dimension.

Case III. At a sufficiently high Reynolds number, the flow around a stationary cylinder results in the formation of the famous von Kármán vortex street. When the cylinder starts oscillating transverse to the flow direction, the vortex shedding pattern becomes significantly more complex. When the amplitude increases the pattern changes from two single vortices (2S mode) to a pair and a single vortex (P+S mode) being shed per oscillation cycle. In a two dimensional flow, we study the topological changes of the wake pattern when vortices are defined as extremal points of the vorticity field. We identify four values of the amplitude that define critical stages in the transition from 2S to P+S wake mode.

Summary (Danish)

Det overordnede mål med denne afhandling er at introducere en systematisk tilgang til at analysere rumlige strukturer i fluid dynamiske problemer. Metoden beskriver, hvordan man fortolker en strømning, der allerede er kendt fra eksperimenter eller fra analytiske/numeriske løsninger til Navier-Stokes ligninger. Med andre ord introducerer vi en detaljeret metode til efterbehandling af hastigheds- eller vorticitetsfelter. Et naturligt udgangspunkt for analysen af et fluid dynamisk problem er at gøre det klart, hvilke parametre problemet afhænger af. Under variation af disse eksterne parametre kan en strømning gennemgå nogle kvalitative ændringer. I denne afhandling analyserer vi sådanne kvalitative ændringer med værktøjer fra bifurkationsteori. Vi fokuserer primært på at beskrive strømningsstrukturen ud fra de hvirvler, der er tilstede i væsken. I denne sammenhæng sker der en kvalitativ ændring i strømningen, når en ny hvirvel opstår eller forsvinder. Vi anvender nogle kendte resultater inden for topologisk fluid dynamik til at analysere ændringerne i topologien af vorticitetsfeltet - mere specifikt analyserer vi hvordan ekstremumpunkter for vorticitetsfeltet opstår of forsvinder, da vi anser disse punkter for at være de karakteristiske punkter for hvirvlerne. Desuden spørger vi os selv, hvordan den teori, vi allerede kender fra topologisk fluid dynamik, kan udvides til at håndtere topologiske ændringer af andre størrelser, der også beskriver strukturen i en strømning.

Som et eksempel på en anden størrelse, der beskriver strømningsstrukturen, betragter vi områder i en strømning, hvor rotation er dominerende i forhold til deformation. Disse områder er ved hjælp af Q-kriteriet defineret som hvirvler [29]. Da en Q-hvirvel er defineret som et område i stedet for et kritisk punkt, kan den teori, vi kender fra topologisk fluid dynamik, ikke anvendes direkte. I denne afhandling fortsætter vi udviklingen af en bifurkationsteori, der kan benyttes til Q-hvirvler. Teorien beskriver de kvalitative ændringer, der kan opstå, når vi tillader flere parametre at variere. Derudover analyserer vi en særlig bifurkation, der kun forekommer i en strømning med en symmetri linje. Alle vores

teoretiske resultater er topologiske, hvilket betyder, at vi ikke skelner mellem hvirvelstrukturer, som kontinuerligt kan deformeres til hinanden.

Afhandlingen er bygget op omkring tre specifikke casestudier, hvor vi analyserer tre klassiske fluid mekaniske problemer ved hjælp af bifurkationsteori. I alle tre tilfælde simuleres hvirvlernes dynamik på en computer, og vi får en meget nøjagtig beskrivelse af strømningen. Den bifurkationsteori, vi udvikler i denne afhandling, giver os en liste over de mulige bifurkationer vi kan observere i hvirvelstrukturen. Vi analyserer de enkelte bifurkationer undervejs, når vi observerer dem i en af de tre casestudier. Anvendelsen af vores teoretiske resultater fører til følgende hovedindsigt i tre cases:

Case I. En hvirvel der bevæger sig over en væg forårsager et viskøst respons nær væggen. Vorticiteten i grænselaget kan løsrive sig fra væggen og danne sekundære hvirvler. Vi studerer dette fænomen i to dimensioner og viser, at processen kan beskrives som en sekvens af fire mulige bifurkationer når hvirvelstrukturen er defineret af Q-kriteriet. Desuden viser vi, at de fleste af disse bifurkationshændelser ser ud til at være meget robuste over for variationer i strømningens Reynolds tal.

Case II. Når flere hvirvler er til stede i en strømning på samme tid, vil de naturligt interagere med hinanden. Vi studerer det simplest mulige tilfælde, hvor to hvirvler interagerer i et todimensionalt flow. Ved at anvende Q-kriteriet viser vi, at to hvirvler med samme rotationsretning kun fusionere, hvis deres relative styrkeforhold er under en bestemt tærskelværdi. Desuden viser vi, at denne tærskelværdi kan identificeres som et bifurkationsfænomen i sig selv. Endelig viser vi, at for tilstrækkeligt små værdier af Reynolds tal kan den såkaldte core growth model bruges i stedet for Navier-stokes-simuleringer som en simpel, analytisk model med et lavt antal frie parametre.

Case III. Ved et tilstrækkeligt højt Reynolds tal opstår von Kármáns berømte hvirvelallé i kølvandet bag en stationær cylinder. Når cylinderen begynder at oscillere på tværs af strømningsretningen, bliver hvirvelstrukturen betydeligt mere kompleks. Når amplituden øges, ser vi et skift fra to enkelte hvirvler (2S-mode) til et par, og en enkelt hvirvel (P + S-mode) der dannes i hver oscillations cyklus. I en todimensionel strømning studerer vi de topologiske ændringer i kølevandets mønster, når hvirvler defineres som ekstremumspunkter for vorticitetsfeltet. Vi identificerer fire værdier af amplituden, der definerer kritiske stadier i overgangen fra 2S-mode til P+S-mode.

Preface

This thesis is submitted in partial fulfilment of the requirements for obtaining the degree of Ph.D. at the Technical University of Denmark (DTU). The project was funded by the Independent Research Fund Denmark (grant no. 6108-0024613) and were primarily carried out at the department of Applied Mathematics and Computer Science (DTU Compute) from the 1st of September 2017 to the 4th of June 2021. The Ph.D. project was supervised by Professor Morten Brøns from DTU Compute and Professor Matthias Heil from School of Mathematics at University of Manchester.

The Ph.D. studies have included two short-term external research stays at:

- The University of Manchester with Professor Matthias Heil.
- Virginia Tech with Professor Mark Stremler.

The results presented in this thesis is to the best of our knowledge original work, except where acknowledgements and references are made to previous work. During the Ph.D. study the following manuscripts has been written:

Paper I *Nielsen, A. R., Heil, M., Andersen, M., & Brøns, M. (2019). Bifurcation theory for vortices with application to boundary layer eruption. Journal of Fluid Mechanics, 865(865), 831–849. doi.org/10.1017/jfm.2019.97*

Paper II *Nielsen, A. R., Andersen, M., Hansen, J. S.& Brøns, M. (2021). Topological bifurcations of vortex pair interactions. Journal of Fluid Mechanics, 917, A11. doi.org/10.1017/jfm.2021.191*

Paper III *Nielsen, A. R., Matharu, P. S. & Brøns, M. (2021). Topological bifurcations in the transition from 2S to P+S mode in the wake behind an oscillating cylinder. Unpublished manuscript*

We want to make it clear that Paper I is partly based on ideas from my master thesis [45] and partly based on results that are original work done during the PhD period. It is specified in chapter 3 which parts of the results originate from the PhD period. Paper II and Paper III are only based on results that are original work done during the PhD period. The thesis consist of the three manuscripts listed above and some additional unpublished work. It also includes a synopsis stating the relationship between the papers and summarizing the results.

Lyngby, 04-June-2021

Anne Ryelund Nielsen

Acknowledgements

First of all I would like to thank my main supervisor Professor Morten Brøns, who has given me an excellent guidance and support during the entire process. He always had the time to discuss my project and every discussion has been a pleasure. I would also like to thank my co-supervisor Professor Matthias Heil and his former Ph.D student Puneet Matharu who has supported me with the numerical part of my project. Without their guidance and great help in setting up the code, it would not have been possible to achieve so satisfying numerical results in the oscillating cylinder experiments.

Next I would like to thank Professor Mark Stremler for inviting me to visit him at Virginia Tech. He and his PhD student Emad Masroor both gave me a warm welcome and a thorough introduction to the world of soap film experiments. My external stay at Virginia Tech has clearly contributed to my research with a different perspective.

I would also like to thank my two collaborators, Associate Professor Morten Andersen and Professor Jesper Hansen from Roskilde University for our fruitful discussions and their excellent advices in relation to our joint study on vortex pair interaction.

Finally, I would like to thank my family, friends and fellow Ph.D. colleagues who have supported me through the entire process.

Contents

Chapter 1

Motivation

Fluid dynamics is the discipline in physics that deals with the movement of liquids and gases. Topology is the discipline in mathematics that is concerned with the properties of a geometric object that are preserved under continuous deformations. In topological fluid dynamics, we work at the intersection of the two disciplines by studying the topological structure of a fluid flow - more specifically, we focus on the topological structure of the vortices in a flow. Vortices are fundamental parts of transitional and turbulent flows. Studying the dynamics and interactions of vortices helps us understand the behaviour of the complicated flows which may occur in nature or industry. Let us start by considering some real-life examples of flows where vortices play an important role.

At the tip of an aircraft wing the differences in pressure between the upper and lower surface of the wing generates a trailing vortex as the aircraft move through the air, see figure 1.1(a). The counter-rotating pair of tip vortices persist in the far wake and can represent a potential hazard for a following aircraft. An aircraft wing with lowered flaps generates a pair of co-rotating vortices at each wing. This pair of vortices is present in the near wake until the vortices merge to a single tip vortex [42]. Motivated by the occurence of wing tip vortices, a pair of straight parallel vortices is one of the elementary vortex configurations considered in the literature. In the review in [37], they refer to the elementary problem as the study of *vortex pair interactions*. During take-off and landing the tip vortices induce some vorticity in the boundary layer of the ground which may erupt and form secondary vortices [19]. This is an example of the classical fluid mechanical problem known as *boundary layer eruption*.

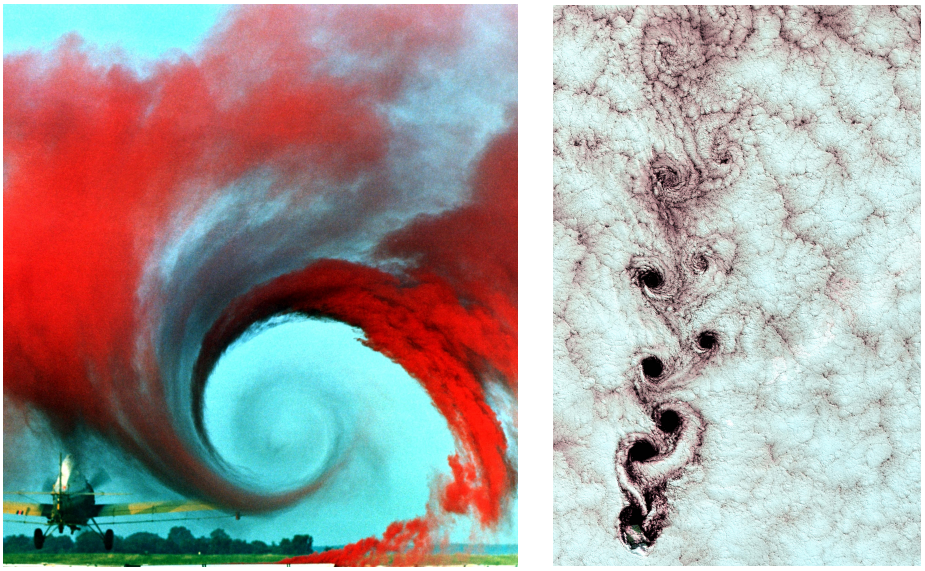

(a) **(b)**

Figure 1.1: (a) A NASA study on wingtip vortices, where the flow around the aircraft wing is made visible by a technique that uses colored smoke rising from the ground [44]. (b) A von Kármán vortex street caused by wind flowing around the Alexander Selkirk Island in the southern Pacific Ocean [7].

Any object moving in a fluid will affect the structure of the flow around it. Due to friction between the object and the fluid, a local rotation of the fluid is induced and vortices are shed at the back of the object and transported away in the wake behind it. When the object is cylindrical the wake pattern is known as the *von Kármán vortex street* - a time-periodic flow in which vortices are shed, alternately on either side of the cylinder. Vortex shedding and the von Kármán vortex street are ubiquitous in nature, and occur at all scales; in arteries where vortices can be generated by a stenosis and in the atmosphere above an island, see figure 1.1(b). If we allow a cylindrical object to move, the vortex shedding pattern becomes significantly more complex. When the cylinder performs forced oscillations transverse to the flow direction, the different vortex shedding patterns have recently become known as *exotic wakes* [48, 3].

In this thesis, we consider boundary layer eruption, vortex pair interactions and exotic wakes as three case studies for the application of our theoretical results. The solution to any fluid dynamical problem typically involves calculating some properties of the fluid as functions of space and time. In all three case studies

we consider an incompressible fluid and the Navier-Stokes equations provide a physical description of the problem. If an incompressible velocity field $\mathbf{u} = (u, v)$ is known either from experiments or from solving Navier-Stokes equations analytically or numerically, then we ask the question, how do we interpret this physical description of a fluid dynamical problem? With the approach we use in this thesis, we believe that the identification of inherent flow patterns and how these changes is key to understanding any fluid dynamical problem. This is where dynamical system theory and in particular bifurcation theory become useful.

The mathematical subject we call a *dynamical system* is completely characterised by its present state and some rules determining how a general state evolve in time. The Navier-Stokes equations are in themselves a dynamical system where the state is given by the velocity and pressure fields. From a solution to Navier-Stokes we can generate several other dynamical systems that describes the evolution of different structures in the physical space. *Bifurcation theory* is the mathematical study of changes in the qualitative or topological structure of a given family, such as the solutions of a family of differential equations. A bifurcation occurs in dynamical systems, when a small smooth change made to the parameter values (the bifurcation parameters) causes a sudden qualitative or topological change in the systems behaviour.

In this thesis we apply well known results from topological fluid dynamics to analyse the dynamics of vortices defined as vorticity extrema. In addition, we expand the theory to include topological changes in the inherent flow pattern defined by the Q-criterion, [29]. Our theory is topological in nature, meaning that we do not distinguish between flow patterns which can be continuously deformed into each other. By applying our theory, we therefore obtain a qualitative but very detailed classification of flow patterns and their bifurcations.

In our studies, we are motivated by a desire to understand the world of fluid dynamics - more specifically, the evolution of the vortices. We hope that the field of dynamical system theory can contribute to this understanding.

1.1 Aims and objectives of this thesis

In my master's thesis [45], we started the investigation on how the approach from topological fluid dynamics can be generalised to describe structural changes of vortices defined by the Q-criterion. The results from my master's thesis include a complete analysis of the possible bifurcations of the Q-vortices that may occur in a robust way when a single parameter is varied. In the first part of this

thesis, we further develop the bifurcation theory for Q-vortices. The first paper we present is partly based on ideas from my master thesis, and partly based on results that are original work done during the PhD period. It therefore introduces the bifurcation theory for Q-vortices from scratch. Within in this thesis we address the following research questions:

- What are the possible bifurcations of the Q-vortices we may observe when we allow several bifurcation parameters to vary? and what are the possible bifurcations of the Q-vortices that may occur in flows with a line of symmetry?
- How can our overall bifurcation theory for Q-vortices contribute to further understanding of classical fluid mechanical problems such as boundary layer eruption and vortex pair interaction?
- How can results from topological fluid dynamics be used to classify exotic wakes patterns behind an oscillating cylinder? and how can a transition in the wake pattern be described in terms of topological bifurcations in the vorticity field?
- How do the topological changes we observe in simulations of the wake pattern agree with similar experiments with an oscillating cylinder in a soap film?

1.2 Outline of the thesis

In chapter 2, we give an introduction to the background knowledge that is needed to understand the results of our research. This includes a brief review of some fundamental concepts in fluid dynamics. The main part of the chapter is an introduction to the mathematical framework in topological fluid dynamics. The simplest possible bifurcation of the streamline pattern is analysed in detail and the necessary tools from bifurcation theory are introduced along the way.

In chapter 3, we present the results of our first paper: *Bifurcation theory for vortices with application to boundary layer eruption.* In this paper we expand the framework of topological fluid dynamics to include an analysis of topological changes in a two-dimensional flow, where the vortex structure is described by the Q-criterion. We apply the theoretical results to analyse the boundary layer eruption problem. The chapter contains an introduction the content of the paper in relation to the rest of the thesis, a reprint of the paper itself and some further perspectives.

In chapter 4, we present the results of our second paper: *Topological bifurcations of vortex pair interactions*. The paper includes a direct continuation of the theoretical results presented in Paper I together with an application to vortex pair interactions. In addition, we discuss the applicability of the analytically traceable core growth model as a replacement for Navier-Stokes simulations. The chapter contains a reprint of the paper itself and a section that summarises the content of the paper in relation to the rest of the thesis.

In chapter 5, we present a manuscript for our third paper: *Topological bifurcations in the transition from 2S to P+S mode in the wake behind an oscillating cylinder*. In this paper, we show that results form topological fluid dynamics can give us a detailed description of the transition between different wake patterns behind an oscillating cylinder. Beside the manuscript itself, the chapter contains an general introduction to the oscillating cylinder problem and a description of some state-of-the-art results.

In chapter 6, we present some result from an experimental study conducted during my external research stay. The physical experiments are performed in a gravity-driven soap film channel where a thin disk is oscillated. The chapter includes an introduction to the experimental setup, and a discussion of whether the conclusions we draw in chapter 5 can be confirmed by the experimental results.

In chapter 7, we conclude the thesis by giving a brief overview of our results and some ideas for future work within this research area.

Chapter 2

Introduction

In this chapter, we want to introduce the background knowledge that is needed to be able to understand the main results of our research. It is our aim that the thesis must be understandable to anyone who has a background in either fluid mechanics or dynamical systems theory. We do not expect the reader to be an expert in both disciplines. We, therefore, give an introduction to some basic concept in fluid dynamics, and show how the framework from dynamical systems theory can be applied to systematically describe structural changes in a flow. The main part of this introductory chapter is a review of some preliminary results from topological fluid dynamics. It is on the basis of these results that our research questions arise.

2.1 Fundamentals of fluid dynamics

In this section, we give a brief introduction to some relevant concepts in fluid dynamics. The derivation of all the presented results can be found in any textbook about fluid dynamics, such as [54], [55] or [35].

The Navier-Stokes equations are the fundamental partial differential equations that is used to describe the motion of viscous fluids. The derivation Navier–Stokes equations is based on the mathematical concept of a fluid parcel which is an amount of fluid that is small enough to be 'infinitesimal' with respect to the length scale and large enough to be distinguished from microscopic particles

such as molecules. By the assumption that a fluid can be considered as a large collection of fluid parcels and by applying *Newton's second law of motion*, one can derive the Navier-Stokes equations that represent the conservation of momentum in a fluid,

$$\frac{\partial \mathbf{u}}{\partial t} + \mathbf{u} \cdot \nabla \mathbf{u} = \frac{1}{\rho} \nabla \cdot (\mu(\nabla \mathbf{u} + (\nabla \mathbf{u})^T - \frac{2}{3}\frac{\mu}{\rho}(\nabla \cdot \mathbf{u})\mathbf{I}) - \frac{1}{\rho}\nabla p. \tag{2.1}$$

At any given time and point, $\mathbf{u}(\mathbf{x}, t)$ is the velocity field, $\rho(\mathbf{x}, t)$ is the density of the fluid and $p(\mathbf{x}, t)$ is the pressure. For a Newtonian fluid the forces acting on the fluid are proportional to the rates of change of the fluid's velocity vector, implying that the dynamic viscosity μ is constant. Although no real fluid can be assumed to be Newtonian, it is a very common assumption for many liquids and gases such as water and air. The Navier-Stokes equation (2.1) is always solved together with the continuity equation,

$$\frac{\partial \rho(\mathbf{x}, t)}{\partial t} + \nabla \cdot (\rho(\mathbf{x}, t)\mathbf{u}(\mathbf{x}, t)) = 0. \tag{2.2}$$

While the Navier-Stokes equations represent the conservation of momentum, the continuity equation represents the conservation of mass. A fluid is said to be incompressible if the density ρ is constant at any given time and point. In reality, all fluids are compressible to some extent but in most situations of general interest a flow can be assumed to be incompressible to a high degree of accuracy. In these cases the continuity equation in (2.2) simplifies to,

$$\nabla \cdot \mathbf{u} = 0. \tag{2.3}$$

Within this thesis, we will only consider fluid mechanical problems with incompressible newtonian fluids. In such problems the Navier–Stokes equations (2.1) simplifies to

$$\underbrace{\frac{\partial \mathbf{u}}{\partial t}}_{(1)} + \underbrace{(\mathbf{u} \cdot \nabla)\mathbf{u}}_{(2)} = \underbrace{\nu \Delta \mathbf{u}}_{(3)} \underbrace{- \frac{1}{\rho}\nabla p}_{(4)}, \tag{2.4}$$

where $\nu = \frac{\mu}{\rho}$ is called the kinematic viscosity of the fluid. The different terms in (2.4) correspond to the unsteady acceleration (1), the advective acceleration (2), the viscous acceleration (3) and the pressure force per unit mass (4). To obtain a particular solution to (2.3) and (2.4) the equations need to be solved with a set of boundary conditions and initial conditions. The complicated nature of

the equations makes it clear that one cannot in general expect to find simple solutions. Exact solutions to the Navier-Stokes equations are very few and they are only found in strongly restricted geometries. In the cases where no analytical solution is known the only options are to perform lab experiments or numerical approximations.

In any classification of a flow the Reynolds number Re is an important dimensionless quantity. The Reynolds number is the ratio of the advective to the viscous forces in a particular flow. One can interpret the Reynolds number as a measure of how lively or sluggish a flow is. By choosing a reference length L and a reference velocity U, that characterise the magnitudes in a particular flow, the Reynolds number is defined as,

$$\mathrm{Re} = \frac{\text{advective acceleration}}{\text{viscous accelaration}} = \frac{U^2/L}{\nu U/L^2} = \frac{UL}{\nu}. \tag{2.5}$$

In this thesis, the goal is mainly to be able to analyse the dynamics of vortices in various fluid mechanical problems. A key concept when analysing the dynamics of vortices is the vorticity field $\boldsymbol{\omega}$, which can be determined directly from the velocity field. The vorticity describes the local spinning motion at a point in the fluid. Mathematically, the vorticity is defined as the curl of the velocity field,

$$\boldsymbol{\omega} = \nabla \times \mathbf{u}. \tag{2.6}$$

Described other in words, the vorticity at a point is a vector representing how the velocity vector will change if we move an infinitesimal distance in a direction that is perpendicular to the velocity vector. As an alternative to the Navier-Stokes equation (2.4), one can use the vorticity transport equation to describe the evolution of the vorticity of a fluid parcel as it moves in a incompressible flow. By taking the curl of Navier-Stokes equation we obtain the vorticity transport equation,

$$\frac{\partial \boldsymbol{\omega}}{\partial t} + \mathbf{u} \cdot \nabla \boldsymbol{\omega} = \boldsymbol{\omega} \cdot \nabla \mathbf{u} + \nu \nabla^2 \boldsymbol{\omega} \tag{2.7}$$

A fluid flow is said to be two-dimensional if the velocity at every point is parallel to a fixed plane. If we choose a coordinate system such that fixed plane is the xy-plane it follows that

$$\mathbf{u}(x, y, z, t) = \begin{pmatrix} u(x, y, t) \\ v(x, y, t) \\ 0 \end{pmatrix}, \tag{2.8}$$

In general, any flow is a three-dimensional problem, but in some cases the velocity field only changes significantly in one or two directions. In these cases, we can ignore the changes in less significant directions and thereby reduce the complexity of the problem. In this thesis, we only deal with problems that can be modelled as being two dimensional. In the analysis of a two-dimensional, incompressible flow, the definition of a stream function ψ is a very useful mathematical tool. For a two-dimensional velocity field defined on a subset U of $\mathbb{R}^2$ a stream function, $\psi : U \to \mathbb{R}$, is a function satisfying the property

$$u = \frac{\partial \psi}{\partial y}, \quad v = -\frac{\partial \psi}{\partial x}. \tag{2.9}$$

By substitution (2.9) into (2.2), we see that a velocity field $\mathbf{u}$ always satisfies the continuity equation when it has an associated stream function ψ,

$$\nabla \cdot \mathbf{u} = \frac{\partial u}{\partial x} + \frac{\partial u}{\partial x} = \frac{\partial}{\partial x}\frac{\partial \psi}{\partial y} + \frac{\partial}{\partial y}\left(-\frac{\partial \psi}{\partial x}\right) = 0. \tag{2.10}$$

The existence of a stream function therefore implies that the flow must be incompressible. Conversely, it can be shown that if a two-dimensional flow is incompressible then there always exist a stream function. The proof of the latter follows from Greens Theorem but will be omitted here.

In the case where we consider a two-dimensional flow the expression for the vorticity field simplifies to

$$\boldsymbol{\omega} = \nabla \times \mathbf{u} = \begin{pmatrix} 0 \\ 0 \\ \frac{\partial v}{\partial x} - \frac{\partial u}{\partial y} \end{pmatrix}, \tag{2.11}$$

which implies that the vorticity field is equivalent to a scalar function ω. By the definition in (2.9), it follows that the vorticity of an incompressible flow is connected to the stream function through following simple relation

$$\omega = -\Delta \psi. \tag{2.12}$$

Since $\boldsymbol{\omega}$ is orthogonal to $\mathbf{u}$ in a two-dimensional flow it follows that $\boldsymbol{\omega} \cdot \nabla \mathbf{u} = 0$, and the vorticity transport equation (2.7) simplyfies to the following scalar equation

$$\frac{\partial \omega}{\partial t} + \mathbf{u} \cdot \nabla \omega = \nu \nabla^2 \omega. \tag{2.13}$$

2.2 Topological fluid dynamics

In the following chapters, we focus on fluid dynamical problems that occur in a two-dimensional incompressible flow. Identifying the inherent flow patterns is the key to understanding of any fluid dynamical problem. Since a fluid flow is described by a continuous deformation of transported scalar or vector fields, it is relevant to consider topological ideas to quantify the changes in a flow field. In the following sections, we assume that an incompressible velocity field $\mathbf{u} = (u, v)$ is known either from experiments or from solving Navier-Stokes equations analytically or numerically. From a given velocity field the motion of any fluid parcel can be determined from the following system of ordinary differential equations

$$\frac{d\mathbf{x}(t)}{dt} = \mathbf{u}(\mathbf{x}(t), t). \tag{2.14}$$

Given a starting point $\mathbf{x}_0$ and a starting time t_0, the solution $\mathbf{x}(t; \mathbf{x}_0, t_0)$ is the the trajectory of the chosen fluid parcel. If we instead consider the instantaneous velocity field $\mathbf{u}(\mathbf{x}, t_0)$ calculated for a fixed time t_0, another system of ordinary differential equations may be defined as

$$\frac{d\mathbf{x}(s)}{ds} = \mathbf{u}(\mathbf{x}(s), t_0). \tag{2.15}$$

The solution curves to this systems are called *streamlines* and they are everywhere tangent to the instantaneous velocity field. Starting at the point $\mathbf{x}_0$ at time t_0 the solution $\mathbf{x}(s; \mathbf{x}_0, t_0)$ determines the path of the streamline passing through the point $\mathbf{x}_0$. Several important topological features of a flow field can be discerned from the local properties of this system, including vortices, stagnation points and recirculation zones [12]. Since the instantaneous velocity does not explicitly depend on s, the system in (2.15) is an autonomous dynamical system. The changes in the streamline structure can therefore be analysed by applying bifurcation theory on the dynamical system. The study of flow patterns described in terms of the topology of the streamlines is called *topological fluid dynamics*. In later studies, the same term has been used when flow patterns is instead described by the the topology of the vorticity field, see e.g. [27],[1]. In the following sections, we give an introduction to the mathematical methods that can be used to analyse structural changes in the of the streamline topology or the vorticity topology.

2.2.1 Streamline topology

Drawing the streamlines is a practical way of visualising a flow. If we observe closed or spiralling streamlines it indicates that the fluid is (instantaneously) moving around a common axis and therefore it is an intuitive way to detect a vortex in a flow. The notion of a vortex is widely used in fluid dynamics, but nevertheless there is no precise mathematical definition of a vortex that is universally accepted. There are many different vortex criteria available in the literature (see [63] for a review) and it is clear that the structural changes in a flow are inextricably linked to the way we identify a given flow pattern. Within this section we focus exclusively on the topology of the streamlines. The streamlines of a flow are closely related to the stream function ψ. For a two-dimensional incompressible velocity field $\mathbf{u} = (u, v)$ there exist a stream function ψ satisfying the property in (2.9). The autonomous dynamical system in (2.15) can therefore be rewritten as

$$\begin{aligned} \frac{dx(s)}{ds} &= \frac{\partial \psi(x(s), y(s), t_0)}{\partial y} \\ \frac{dy(s)}{ds} &= -\frac{\partial \psi(x(s), y(s), t_0)}{\partial x}. \end{aligned} \tag{2.16}$$

where $\psi(x, y, t_0)$ is the instantaneous stream function calculated for a fixed time t_0. We see that the dynamical system in (2.16) is completely described by the scalar function ψ, and it has the structure of a planar Hamiltonian system. We recall that the trajectories of a Hamiltonian system are simply the level sets of the Hamiltonian function. Implying that the stream function is constant along any streamline,

$$\frac{d}{ds}\psi(x(s), y(s)) = \frac{\partial \psi}{\partial x}\frac{dx}{ds} + \frac{\partial \psi}{\partial y}\frac{dy}{ds} = \frac{\partial \psi}{\partial x}\frac{\partial \psi}{\partial y} - \frac{\partial \psi}{\partial y}\frac{\partial \psi}{\partial x} = 0. \tag{2.17}$$

The analysis of a streamline pattern commences by locating the critical points of the system in (2.16), i.e. the points where $\partial_x \psi = \partial_y \psi = 0$. In the context of fluid dynamics, these points are traditionally called stagnation points since they appear when the velocity field is zero, i.e. $u = v = 0$. The type of critical point is determined by the eigenvalues of the Jacobian evaluated at a critical point (further details can be found in e.g. [56],[40]). In our case, where we consider a two-dimensional autonomous Hamiltonian system, the Jacobian simplifies to

$$J = \begin{pmatrix} \frac{\partial u}{\partial x} & \frac{\partial u}{\partial y} \\ -\frac{\partial v}{\partial x} & -\frac{\partial v}{\partial y} \end{pmatrix} = \begin{pmatrix} \frac{\partial^2 \psi}{\partial x \partial y} & \frac{\partial^2 \psi}{\partial y^2} \\ -\frac{\partial^2 \psi}{\partial x^2} & -\frac{\partial^2 \psi}{\partial x \partial y} \end{pmatrix} = \begin{pmatrix} 0 & 1 \\ -1 & 0 \end{pmatrix} \cdot H^{\psi}, \tag{2.18}$$

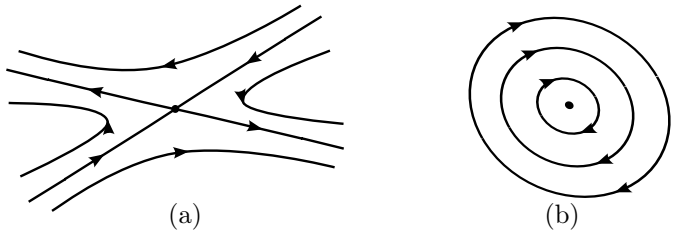

Figure 2.1: Illustration the streamline pattern in a neighbourhood of a non-degenerate critical point in a planar Hamiltonian system: (a) a saddle point, (b) a center.

where H^ψ is the Hessian of the stream function. We notice that $\det(J) = \det(H^\psi)$ and $\mathrm{tr}(J) = \mathrm{tr}(H^\psi) = 0$, and hence it follows that the eigenvalues of J are given as

$$\lambda_{1,2} = \pm\sqrt{-\det(H^\psi)}. \tag{2.19}$$

Since the dynamical system we are considering is a Hamiltonian system, the possible types of critical points are therefore limited to the following three cases:

1. For a critical point where $\det(H^\psi) < 0$, the eigenvalues are real and satisfy that $\lambda_1 = -\lambda_2$. Since both eigenvalues have non-zero real parts the critical point is said to be hyperbolic.

2. A critical point where $\det(H^\psi) > 0$ has non-zero and purely imaginary eigenvalues satisfying that $\lambda_1 = -\lambda_2$. Since the eigenvalues are non-zero and purely imaginary the critical point is said to be elliptic.

3. For a critical point where $\det(H^\psi) = 0$, the eigenvalues are both zero and the critical point is denoted as degenerate.

In the first case the critical point is hyperbolic and we can apply *Hartmann-Grobmans Theorem* that states that the topology of a non-linear system can be determined from the linearised system in a neighbourhood of a hyperbolic critical point [56],[40]. A critical point where $\det(H^\psi) < 0$ is a saddle point for the linearised system and the same therefore applies to our non-linear system (2.16), see figure 2.1(a). A saddle point represents a stagnation point in the flow. Since streamlines cannot intersect each other the stable and unstable manifolds

are dividing the flow in four regions. If ψ takes the value K at a saddle point, the dividing streamlines can be found by solving $\psi(x, y) = K$.

In the second case the critical point in the linearised system is a center, meaning that trajectories are closed elliptical orbits around the critical point. For a general non-linear system we cannot conclude that a center in the linearised system will persists in the non-linear system. In our case where we consider a Hamiltonian system, we recall, however, that the streamlines of the non-linear system (2.16) are level curves for the stream function ψ. A local extremum of the stream function ψ will therefore corresponds to a center in both the non-linear system and the linearised. A center represents a point of stagnation in the fluid where nearby fluid particles instantaneously rotate around the stagnation point, see figure 2.1(b). A streamline center can therefore be interpreted as an indicator of a vortex. Later we will discuss how this vortex criterion may lead to ambiguous results.

In the two cases with non-degenerate critical points we have now found that the topology the non-linear system (2.16) can be deduced from the linearised system. If a critical point is instead degenerate, it is, as we shall see later, the higher order derivatives that become decisive for the streamline pattern. The idea of obtaining a qualitative understanding of a flow by analysing the streamline topology, and especially the critical points, has been seen in early studies such as [18] and [17].

So far, we have only considered the instantaneous streamline topology that can be deduced from the stream function evaluated at a fixed time, i.e. $\psi(x, y, t_0)$. By varying the time t_0 (or any other parameter affecting the flow) the structure of the streamlines might change. P. G. Bakker was the first to use bifurcation theory to systematically describe these changes of flow patterns (for a review of his results see [5]). In the following section, we give an introduction to a mathematical framework that can be used to analyse such bifurcations systematically. The necessary tools from the bifurcation theory are introduced along the way through a complete analysis of the simplest possible bifurcation. In the analysis, we make use of higher order derivatives of ψ and therefore we make the following necessary remark.

Remark 2.1 *We assume that ψ is a continuous function with continuous derivatives to the finite order required in our analysis.*

2.2.1.1 Bifurcations in the streamline topology

Often a dynamical system depends on some external parameters. In the context of fluid dynamics, one could think of the Reynolds number or the aspect ratio of the geometry. In our case we also consider the time t as a parameter since a given streamline topology is associated with a fixed time t_0. To account for this dependence, we rewrite our system in (2.16) as follows

$$\begin{aligned} \frac{dx}{ds} &= \frac{\partial \psi(x, y; \mathbf{p})}{\partial y} \\ \frac{dy}{ds} &= -\frac{\partial \psi(x, y; \mathbf{p})}{\partial x}, \end{aligned} \tag{2.20}$$

where $\mathbf{p} \in \mathbb{R}^n$ is a vector containing all the possible parameters affecting the system. An understanding of changes in the streamline structure can be achieved by applying bifurcation theory to analyse the solutions we obtain by varying parameters in (2.20). To analyse the structural changes we need to specify what we mean by a change in the structure. This is done by first defining that two flow patterns are qualitative alike if their governing Hamiltonian systems are *topological equivalent*.

Definition 2.2 Let ψ and ψ' be two stream functions defined on a open subset of $\mathbb{R}^2$. The two corresponding Hamiltonian systems are *topological equivalent* if there exist a continuous, bijective map h, whose inverse is also continuous, that maps the streamlines of the first system onto streamlines of the second system, preserving the direction of time. If h is only defined in a subset of the flow domain, the two systems are *locally topologically equivalent*.

The concept of topological equivalence can be understood by imagining that a given streamline pattern is printed on a sheet of rubber. Any other streamline pattern that may appear by stretching or compressing the rubber sheet will then be topological equivalent to the original pattern. For two topological equivalent streamline patterns the number of critical points will always be the same as the bijective mapping will map any critical point into a critical point. Having specified what we mean by qualitatively alike streamline patterns, we can discuss whether or not a small perturbation of the parameter values in $\mathbf{p}$ will result in a change in the structure. For any non-critical point the Flow Box theorem gives us an important result

Theorem 2.3 (The Flow Box theorem) *Let H be a Hamiltonian and let (x_0, y_0) be a non-critical point of the corresponding Hamiltonian system.*

Then there exist a neighbourhood of (x_0, y_0) *the Hamiltonian system is topological equivalent to the constant sytem:* $\dot{x} = 0, \dot{y} = 1$.

For a proof see e.g. [38]. Let (x_0, y_0) be a non-critical point of (2.20) when $\mathbf{p} = \mathbf{p}_0$. Then there exist a neighbourhood of (x_0, y_0) where the system is topological equivalent to the constant sytem. The continuity of $\partial_x\psi$ and $\partial_y\psi$ guarantees that (x_0, y_0) will remain non-critical for sufficiently small variations in $\mathbf{p}_0$, and the system will therefore reamin to topological equivalent to the constant sytem in some neighbourhood of (x_0, y_0). Which means that the topology of the local streamline pattern is preserved for sufficiently small variations in the parameter values $\mathbf{p}_0$. To locate any structural changes in the streamline pattern we must therefore look at the flow pattern close to a critical point. An important tool in the following bifurcation analysis is the *Implicit Function Theorem*, which we will use repeatedly throughout the thesis. It can be found in various textbooks, here it is stated as given in [40],

Theorem 2.4 (Implicit Function Theorem) *Let* U *be an open set in* $\mathbb{R}^n \times \mathbb{R}^k$ *and* $F \in C^r(U, \mathbb{R}^n)$ *with* $r \geq 1$. *Suppose there is a point* $(x_0, \mu_0) \in U$ *such that* $F(x_0; \mu_0) = c$ *and* $D_x F(x_0, \mu_0)$ *is a nonsingular* $n \times n$ *matrix. Then there are open sets* $V \subset \mathbb{R}^n$ *and* $W \subset \mathbb{R}^k$ *and a unique* C^r *function* $\xi(\mu) : W \to V$ *for which* $x_0 = \xi(\mu_0)$ *and* $F(\xi(\mu); \mu) = c$.

To locate structural changes in the streamline pattern, we start by considering the simplest case where the critical point is non-degenerate i.e. either a saddle point or a center. Let (x_0, y_0) be a critical point of (2.20) when $\mathbf{p} = \mathbf{p}_0$. Without loss of generality, we can assume that critical point is located at the origin and $\mathbf{p_0} = \mathbf{0}$. We use subscript 0 to denote any function evaluation at $(x, y; \mathbf{p}) = (0, 0; \mathbf{0})$. As described above, a non-degenerate critical point satisfies that

$$\partial_x\psi_0 = \partial_y\psi_0 = 0, \tag{2.21}$$

and

$$H_0^\psi = \begin{pmatrix} \partial_{xx}\psi_0 & \partial_{xy}\psi_0 \\ \partial_{xy}\psi_0 & \partial_{yy}\psi_0 \end{pmatrix} \text{ is non-singular.} \tag{2.22}$$

It follows from the Implicit Function Theorem that there exist unique local functions $X(\mathbf{p}) = x$ and $Y(\mathbf{p}) = y$ for which

$$X(\mathbf{0}) = 0 \text{ and } Y(\mathbf{0}) = 0, \tag{2.23}$$

and

$$\partial_x\psi(X(\mathbf{p}), Y(\mathbf{p}); \mathbf{p}) = 0 \tag{2.24}$$

$$\partial_y\psi(X(\mathbf{p}), Y(\mathbf{p}); \mathbf{p}) = 0. \tag{2.25}$$

The fact that X and Y are local functions means that they are defined for $\mathbf{p}$ in some neighbourhood of $\mathbf{0}$. The uniqueness of X and Y implies that there is exactly one critical point in the neighbourhood of $(x, y) = (0, 0)$. Furthermore, the continuity of H_0^ψ guarantees that $\det(H_0^\psi)$ will not change sign. Hence, it is not difficult to see that any sufficiently small variation in $\mathbf{p}$ will only make the critical point move slightly, keeping its type. Hence, we say that any non-degenerate critical point is *structurally stable*. To locate any structural changes in the streamline pattern we must therefore look for flow patterns with degenerate critical points satisfying that

$$\partial_x \psi_0 = \partial_y \psi_0 = 0 \tag{2.26}$$

and

$$H_0^\psi = \begin{pmatrix} \partial_{xx}\psi_0 & \partial_{xy}\psi_0 \\ \partial_{xy}\psi_0 & \partial_{yy}\psi_0 \end{pmatrix} \text{ is singular.} \tag{2.27}$$

The analysis consist of two subcases, either H_0^ψ is the zero matrix or zero is an eigenvalue of H_0^ψ with geometric multiplicity one. Here we will elaborate on the latter case which is the simplest degeneracy. Without loss of generality, we assume that the coordinate system is chosen such that

$$\partial_{xx}\psi_0 = \partial_{xy}\psi_0 = 0 \quad \text{and} \quad \partial_{yy}\psi_0 \neq 0 \tag{2.28}$$

In the following analysis the higher order derivatives become decisive for the streamline pattern. As we will see, the simplest case occurs when

$$\partial_{xxx}\psi_0 \neq 0 \tag{2.29}$$

From the conditions in (2.26)-(2.29) we want to determine the local structure of the streamlines close to a degenerate critical point located at the origin when $\mathbf{p} = \mathbf{0}$. If ψ takes the value K at the degenerate critical point the structure of the streamlines can be found by solving $\psi(x, y, \mathbf{0}) = K$. A Taylor expansion of the stream function at the origin simplifies to

$$\psi(x, y, \mathbf{0}) = K + a_{0,2}y^2 + a_{3,0}x^3 + a_{2,1}x^2y + a_{1,2}xy^2 + a_{0,3}y^3 + \mathcal{O}(\|(x, y)\|^4), \tag{2.30}$$

where

$$\begin{aligned} a_{0,2} &= \frac{1}{2}\partial_{yy}\psi_0 \neq 0 \\ a_{3,0} &= \frac{1}{6}\partial_{xxx}\psi_0 \neq 0. \end{aligned} \tag{2.31}$$

Hence, the structure of the level curve of ψ passing through the degenerate critical point can be determined by solving the equation

$$0 = a_{0,2}y^2 + a_{3,0}x^3 + a_{2,1}x^2y + a_{1,2}xy^2 + a_{0,3}y^3 + \mathcal{O}(\|(x,y)\|^4). \tag{2.32}$$

To obtain a parametric representation of the streamline, we make a change of coordinates, $y = mx$, which is well-defined and invertible for any $x \neq 0$. Furthermore we define

$$F(x,m) = a_{0,2}m^2 + a_{3,0}x + a_{2,1}xm + a_{1,2}xm^2 + a_{0,3}xm^3 + \cdots . \tag{2.33}$$

From this definition of F, (2.32) can be rewritten as

$$0 = x^2F(x,m). \tag{2.34}$$

For any m, $x = 0$ is a solution with multiplicity two. To obtain a parametric representation of the rest of the solution curve we must solve $F(x,m) = 0$. We notice that $F(0,0) = 0$ and as a result of the inequality assumption in (2.29),

$$\partial_x F(0,0) = a_{3,0} \neq 0. \tag{2.35}$$

Hence, it follows from the Implicit Function Theorem that there exist a unique local function $X(m) = x$ for which $X(0) = 0$ and

$$F(X(m),m) = 0. \tag{2.36}$$

Form the local function X we can determine a parametric representation of the level curve given as $\mathbf{r}(m) = (X(m), Y(m))$, where $Y(m) = mX(m)$. By implicit differentiation of (2.36) we obtain

$$\partial_x F(X(m),m)X'(m) + \partial_m F(X(m),m) = 0, \tag{2.37}$$

which evaluated in $m = 0$ gives us that $X'(0) = 0$ and $Y'(0) = 0$. As expected the origin is a singular point on the level curve of ψ, to classify the the singularity we compute the second order derivative, which are found by implicit differentiating (2.37), and evaluating the derivatives in $m = 0$

$$\partial_x F(0,0)X''(0) + \partial_{mm}F(0,0) = 0. \tag{2.38}$$

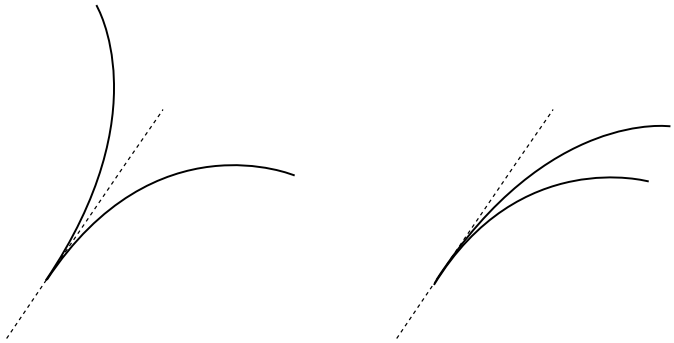

(a) (b)

Figure 2.2: Illustration of the streamline pattern in a neighbourhood of a degenerate critical point being: (a) an ordinary cusp singularity, (b) a rhamphoid cusp singularity.

Implying that

$$\begin{aligned} X''(0) &= -\frac{2a_{0,2}}{a_{3,0}} \neq 0, \\ Y''(0) &= 2X'(0) + 0 \cdot X''(0) = 0 \\ Y'''(0) &= 3X''(0) + 0 \cdot X'''(0) = -\frac{6a_{0,2}}{a_{3,0}} \neq 0. \end{aligned} \tag{2.39}$$

Since $\mathbf{r}''(0) \neq \mathbf{0}$, the critical point is a *quadratic cusp*. There are two possible types of quadratic cusp singularities: *ordinary* and *rhamphoid*, see illustrations of the two types in figure 2.2. Since $\mathbf{r}'''(0)$ is not parallel to $\mathbf{r}''(0)$, we can conclude that two streamlines meet at the origin in a ordinary cusp singularity, as illustrated in figure 2.2(a). Further details can be found in various text books such as [50]. Having described the qualitative structure of the streamline pattern exactly at the degenerate critical point we are interested in structural changes of the pattern that occur at the degenerate critical point when external parameters are varied. The question that then arises is, what new structures can we expect after a given perturbation of the system? and is there a way to classify all possible patterns that appear?

We find the answers by applying tools from bifurcation theory. Let us again consider the system in (2.20). Let $(x, y) = (0, 0)$ be a degenerate critical point of the stream function $\psi_0(x, y)$, we say that the parametric family of stream functions $\psi(x, y, \mathbf{p})$ is an *unfolding* of the degenerate critical point if $\psi(x, y, \mathbf{0}) = \psi_0(x, y)$ in a neighbourhood of $(0, 0)$. In other words, the unfolding represents all

possible changes of the streamline structure that may occur for sufficiently small changes of $\mathbf{p}$. We start by considering the case where ψ depend on variations in a single parameter $p \in \mathbb{R}$ and assume that $(x, y) = (0, 0)$ is a degenerate critical point when $p = 0$. Based on the discussion above, the critical point must fulfil

$$\partial_x \psi_0 = 0, \;\; \partial_y \psi_0 = 0, \;\; \partial_{xx} \psi_0 = 0, \;\; \partial_{xy} \psi_0 = 0, \tag{2.40}$$

Together with the following non-degeneracy conditions,

$$\partial_{yy} \psi_0 \neq 0, \;\; \partial_{xxx} \psi_0 \neq 0, \;\; \partial_{xp} \psi_0 \neq 0. \tag{2.41}$$

The last condition in (2.41) is introduced to ensure that the degenerate streamline pattern changes with variations in p, it will become clear from the analysis below why it is exactly $\partial_{xp}\psi_0$ that is chosen to be non-degenerate. We now want to investigate what happens to the number and the type of critical points in a neighbourhood of $(0, 0)$ for sufficiently small changes in p. As we want to employ the Implicit Function Theorem we consider the following Jacobian

$$J = \frac{\partial(\partial_x \psi, \partial_y \psi)}{\partial(y, p)} = \begin{pmatrix} \partial_{xy}\psi & \partial_{xp}\psi \\ \partial_{yy}\psi & \partial_{yp}\psi \end{pmatrix}. \tag{2.42}$$

Since $\det(J_0) = \partial_{yy}\psi_0 \partial_{xp}\psi_0 \neq 0$, J_0 is non-singular and it follows from the Implicit Function Theorem that there exist unique local functions $Y(x) = y$ and $P(x) = p$ for which

$$Y(0) = 0 \text{ and } P(0) = 0, \tag{2.43}$$

and

$$\begin{aligned} \partial_x \psi(x, Y(x), P(x)) &= 0 \\ \partial_y \psi(x, Y(x), P(x)) &= 0 \end{aligned} \tag{2.44}$$

Let $p^* \neq 0$ be sufficiently small. By solving $P(x^*) = p^*$ we can determine the x-coordinate(s) of the critical point(s) of $\psi(x, y, p^*)$ in a neighbourhood of $(x, y) = (0, 0)$. The derivatives of P can be found by implicit differentiation of (2.44)

$$J \begin{pmatrix} Y'(x) \\ P'(x) \end{pmatrix} = \begin{pmatrix} \partial_{xx}\psi \\ \partial_{xy}\psi \end{pmatrix}, \tag{2.45}$$

which evaluated in $x = 0$ gives us

$$\begin{pmatrix} Y'(0) \\ P'(0) \end{pmatrix} = J_0^{-1} \begin{pmatrix} \partial_{xx}\psi_0 \\ \partial_{xy}\psi_0 \end{pmatrix} = \begin{pmatrix} 0 \\ 0 \end{pmatrix}. \tag{2.46}$$

The second order derivative is found by implicit differentiating (2.45) and evaluating the derivatives in $x = 0$:

$$\begin{pmatrix} Y''(0) \\ P''(0) \end{pmatrix} = -J_0^{-1} \left(\begin{pmatrix} \partial_{xxx}\psi_0 \\ \partial_{xxy}\psi_0 \end{pmatrix} + 2J_0' \begin{pmatrix} Y'(0) \\ P'(0) \end{pmatrix} \right) = -J_0^{-1} \begin{pmatrix} \partial_{xxx}\psi_0 \\ \partial_{xxy}\psi_0 \end{pmatrix} \tag{2.47}$$

where

$$J_0' = \left(\frac{\partial J}{\partial x} + \frac{\partial J}{\partial y} Y'(x) + \frac{\partial J}{\partial p} P'(x) \right) \Big|_0 = \frac{\partial J}{\partial x} \Big|_0 . \tag{2.48}$$

Hence, it follows that

$$\begin{aligned} Y''(0) &= \frac{\partial_{yp}\psi_0 \partial_{xxx}\psi_0 - \partial_{xp}\psi_0 \partial_{xxy}\psi_0}{\partial_{xp}\psi_0 \partial_{yy}\psi_0} \\ P''(0) &= -\frac{\partial_{xxx}\psi_0}{\partial_{xp}\psi_0 \partial_{yy}\psi_0} \neq 0 \end{aligned} . \tag{2.49}$$

By Taylor expanding P at the origin, we get that

$$P(x) = -\frac{\partial_{xxx}\psi_0}{2\partial_{xp}\psi_0 \partial_{yy}\psi_0} x^2 + \mathcal{O}(x^3). \tag{2.50}$$

For sufficiently small values of p^*, the x-coordinate(s) of the critical point(s) can be approximated as,

$$x^* \approx \pm \sqrt{-p^* \frac{\partial_{xxx}\psi_0}{2\partial_{xp}\psi_0 \partial_{yy}\psi_0}}. \tag{2.51}$$

The equation in (2.51) implies that the sign of p^* changes the number of critical points. If $\text{sign}(\partial_{xxx}\psi_0) = \text{sign}(\partial_{xp}\psi_0 \partial_{yy}\psi_0)$ there are two critical points when $p^* < 0$ and no critical point when $p^* > 0$. In the other case where $\text{sign}(\partial_{xxx}\psi_0) \neq \text{sign}(\partial_{xp}\psi_0 \partial_{yy}\psi_0)$ there are no critical points when $p^* < 0$ and two critical point when $p^* > 0$. As discussed above, the type of critical point is determined by the sign of $\det(H^\psi)$ evaluated at the critical point. We notice that

$$\frac{d \det(H(x, Y(x), P(x))}{dx} \Big|_0 = \partial_{xxx}\psi_0 \partial_{yy}\psi_0 \neq 0. \tag{2.52}$$

Since $\det(H_0^\psi) = 0$, the result in (2.52) implies that the determinant of the Hessian changes sign when x changes sign. For a sufficiently small value of

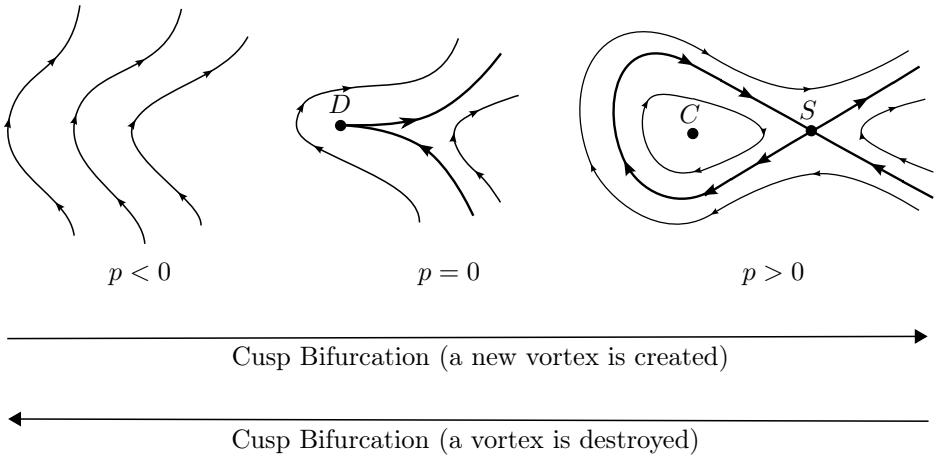

Figure 2.3: Illustration of the streamline pattern during a cusp bifurcation in the case where $\text{sign}(\partial_{xxx}\psi_0) = \text{sign}(\partial_{xp}\psi_0\partial_{yy}\psi_0)$. For increasing p the streamlines deform to create an ordinary cusp singularity at the degenerate critical point (D). When increasing p further a saddle (S) and a center (C) emerge which result in the formation of a vortex.

p^* where two critical points located approximately at $\pm x^*$, it follows that one critical point is a saddle and the other is a center. When p is varied through $p = 0$ the center and saddle point coalesce and disappear. The streamline pattern at a degenerate critical point is called *structurally unstable* because an arbitrarily small perturbation in p may lead to different dynamics in the system (2.20). The change of structure is denoted a *cusp bifurcation* or a *saddle-center bifurcation*. The streamline structure in a neighbourhood of the bifurcation point is illustrated in figure 2.3.

So far we have only considered a flow pattern depending on a single parameter p. If we instead consider the case where ψ depends on k parameters, one could ask how variations in the remaining $k - 1$ parameters would affect the cusp bifurcation. Let us assume that $\mathbf{p} \in \mathbb{R}^k$ and that $(x, y) = (0, 0)$ is a degenerate critical point when $\mathbf{p} = \mathbf{0}$. Again we consider the simplest possible degeneracy where

$$\partial_x\psi_0 = 0, \;\; \partial_y\psi_0 = 0, \;\; \partial_{xx}\psi_0 = 0, \;\; \partial_{xy}\psi_0 = 0, \tag{2.53}$$

and

$$\partial_{yy}\psi_0 \neq 0, \;\; \partial_{xxx}\psi_0 \neq 0, \tag{2.54}$$

Without loss of generality, we assume that the parameter that satisfies the required non-degeneracy condition is the first element in the parameter vector

p, i.e.

$$\partial_{xp_1}\psi_0 \neq 0 \tag{2.55}$$

To investigate how variations in the remaining parameters $\mathbf{q} = (p_2, \ldots, p_k) \in \mathbb{R}^{k-1}$ affect the cusp bifurcation we consider the following Jacobian

$$J = \frac{\partial(\partial_x\psi, \partial_y\psi, |H^\psi|)}{\partial(x, y, p_1)} = \begin{pmatrix} \partial_{xx}\psi & \partial_{xy}\psi & \partial_{xp_1}\psi \\ \partial_{xy}\psi & \partial_{yy}\psi & \partial_{yp_1}\psi \\ \partial_x|H^\psi| & \partial_y|H^\psi| & \partial_{p_1}|H^\psi| \end{pmatrix}. \tag{2.56}$$

Where $|H^\psi|$ denotes the determinant of the Hessian matrix of ψ. Evaluated at $(x, y; \mathbf{p}) = (0, 0; \mathbf{0})$, J simplifies to

$$J_0 = \begin{pmatrix} 0 & 0 & \partial_{xp_1}\psi_0 \\ 0 & \partial_{yy}\psi_0 & \partial_{yp_1}\psi_0 \\ \partial_x|H^\psi|_0 & \partial_y|H^\psi|_0 & \partial_{p_1}|H^\psi|_0 \end{pmatrix}. \tag{2.57}$$

Since $\partial_x|H^\psi|_0 = \partial_{xxx}\psi_0\partial_{yy}\psi_0 \neq 0$, J_0 is non-singular and it follows from the Implicit Function Theorem that there exist unique local functions $X(\mathbf{q}) = x$, $Y(\mathbf{q}) = y$ and $P(\mathbf{q}) = p_1$ for which

$$X(\mathbf{0}) = 0, Y(\mathbf{0}) = 0 \text{ and } P(\mathbf{0}) = 0 \tag{2.58}$$

and

$$\partial_x\psi(X(\mathbf{q}), Y(\mathbf{q}); P(\mathbf{q}), \mathbf{q}) = 0 \tag{2.59}$$

$$\partial_y\psi(X(\mathbf{q}), Y(\mathbf{q}); P(\mathbf{q}), \mathbf{q}) = 0 \tag{2.60}$$

$$|H^\psi(X(\mathbf{q}), Y(\mathbf{q}); P(\mathbf{q}), \mathbf{q})| = 0 \tag{2.61}$$

The uniqueness of X, Y and P implies that there is exactly one degenerate critical point in the neighbourhood of $(x, y) = (0, 0)$. The continuity of $\partial_{xxx}\psi$, $\partial_{yy}\psi$ and $\partial_{xp_1}\psi$ guarantees that they will remain non-zero for sufficiently small changes in $\mathbf{q}$. The degenerate critical at $(X(\mathbf{q}), Y(\mathbf{q}); P(\mathbf{q}), \mathbf{q})$ therfore satisfies the conditions for a cusp bifurcation point, and hence we conclude that any cusp bifurcation is robust to variations in the remaining $k-1$ parameters. The equation $P(\mathbf{q}) = p_1$ defines a surface with dimension $k-1$ in the parameter space on which the cusp bifurcation occur. Since the parameter space has dimension k we say that the cusp bifurcation as *codimension one*. In general, any bifurcation that occur in a robust way when a single parameter is varied is referred to as having codimension one. We have now made a complete analysis of the structural changes near a degenerate critical point satisfying the three non-degeneracy conditions in (2.41). Any of these non-degeneracy conditions

may, of course, turn out to be violated. To analyse the structural changes in one of these cases, we should insist on the violation and turn the relevant non-degeneracy condition into an additional degeneracy condition. This imposition provides an additional equation that describes the location of a degenerate critical point. To fulfil the set of new degeneracy conditions an extra parameter is require to take on a particular value and the bifurcation that occur when these parameters are varied is referred to as having codimension two. The purpose of the analysis in this section was to introduce a general method and the necessary framework through an example. Therefore, we will not analyse any higher order bifurcations in detail. These results can be found in [26] together with the analysis of bifurcations in flows with symmetry and flows near a no-slip wall.

The above analysis of the cusp bifurcation is mainly driven by the Implicit Function Theorem. In many previous studies the possible bifurcations of the streamline pattern have been investigated systematically using simplifying normal form transformations [26], [25], [12], [9]. With this approach a normal form of the stream function is constructed from a truncated Taylor expansion. The dependence of the parameters $\mathbf{p}$ is incorporated in the coefficients of the Taylor series and the normal form is a simplification of the stream function that is equivalent up to a coordinate transformation [40]. The non-linear transformations result in a much simplified stream function which still represents the local flow qualitatively correct. The advantage of using the normal form approach is the possibility to find simplified systems which generalises to bifurcations with higher codimension. A complete analysis with the normal form approach should include a proof that the truncated normal form is topologically equivalent to the full normal form. This proof is in some cases very technically demanding and therefore left out in many previous studies [9]. By using a more direct approach based mainly on the Implicit Function Theorem, we completely avoid these theoretical considerations. Another disadvantage of the normal form approach is that it is not always clear how the coefficients in the normal form relate to real physical parameters. With our approach, the requirements for a particular type of bifurcation are precisely defined in terms of the derivatives of the physical parameters.

In the original research we are to present in this thesis, we analyse the possible bifurcation events with an approach similar to the analysis of the cusp bifurcation that was reviewed earlier in this section. Since we are not going to use normal form approach, we will not make any further introduction to the method here. All previous studies focusing on bifurcations in the streamline pattern contribute to an overall toolbox that can be used to study qualitative changes in the streamline topology in various flows. Some examples of previous applications can be found in the following studies [6], [10], [14].

2.2.2 Vorticity topology

The stream function is not Galilean invariant, and the streamline pattern may therefore be affected by changing the frame of reference. In order to ensure that a vortex is visible in the streamlines, it is necessary to choose a frame moving with the speed of the vortex center. The use of closed or spiral streamlines as a definition of a vortex will clearly fail in a flow containing several vortices advecting at different speeds. Among others, Jeong & Hussain [30] argue that an objective vortex definition must be Galilean invariant. The vorticity field ω depends only on the derivatives of the velocity field is and hence it is invariant under any Galilean transformation. It is therefore common to analyse the structure of the flow field by studying the topology of its vorticity field. We recall that the vorticity describes the local spinning motion at a point in the fluid and in the core of a vortex we expect the magnitude of vorticity to attain high values relative to its environment. Assuming the flow is two-dimensional, the vorticity is a scalar field. If a critical point of ω is an extremum, it is encircled by closed level curves, and such a region can be thought of as a vortex core. In other words, an extremum of vorticity is a so-called feature point for a vortex [33].

The topology of the scalar vorticity field can be analysed by the exact same approach as described for the topology of the stream function. Brøns & Bisgaard were the first to extend the concept of topological fluid dynamics to also include qualitative studies where the flow pattern is described by the topology of the vorticity field [11]. This is done by considering the following planar Hamiltonian system,

$$\begin{aligned} \frac{dx}{ds} &= \frac{\partial \omega(x, y; \mathbf{p})}{\partial y} \\ \frac{dy}{ds} &= -\frac{\partial \omega(x, y; \mathbf{p})}{\partial x}, \end{aligned} \tag{2.62}$$

where ω is now the governing the Hamiltonian function. We see that a critical point of the dynamical system in (2.62) corresponds to critical point for ω. Assuming that ω is known either from experiments or from solving Navier-Stokes equations, the results from the previous section can be applied directly in the analysis of vorticity topology. A local extremum of the vorticity will thus correspond to a center in Hamiltonian system (2.62). In general, it is difficult to explain the physical significance of a saddle point in the vorticity field, but in the previous section we saw how a saddle point play an important role in the creation of a new center (i.e. a new vortex) through a cusp bifurcation. As mentioned above, the cusp bifurcation is the simplest possible topological bifurcation and

the only one with codimension one. However, all other bifurcations described for the stream function can also be used directly in the context of vorticity. Where the level curves of the stream function, in themselves, have a physical interpretation, we are only interested in the critical points when studying the topology of the vorticity field. Several studies have already taken advantage of the framework to study qualitative changes in the vorticity topology. Heil et al. use the framework to describe the creation of the von Kármán vortex street [27] and Andersen et al. analyse the interaction of two vortices [1]. In chapter 5 we apply the framework to analyse the topological bifurcations in the wake of an oscillating cylinder.

2.2.3 Topology of other inherent flow structures

It is clear that any description of the structural changes in a flow must be inextricably linked to the way we define the flow structure, in particular how a vortex is defined. In the previous section we described how the framework within topological fluid dynamics has been extended to include qualitative studies where flow pattern is described by the topology of the vorticity field. We believe, however, that the concept could just as well be extended to cover topological changes of any quantity describing the flow structure. In this project, we mainly focus on describing the flow structure based on the vortices present in the fluid. So far we have touched upon two different definitions of vortices: streamline centers and extremal points of the vorticity field. There are, however, many other vortex criteria available in the literature (see [63] for a review) and new ideas are continuously being proposed, e.g. [24] and [64]. By taking a brief look at the literature, we realise that it is not a trivial task to define a vortex unambiguously [23]. Most commonly, vortices are defined as regions with closed or spiralling streamlines, regions with low pressure or regions where the velocity gradient tensor has complex eigenvalues. In [23], Haller argues that an objective vortex criteria should not only be Galilean invariant but also rotationally invariant. As a result, he introduces the M_Z criterion, where a vortex is a set of fluid trajectories along which the strain acceleration tensor is indefinite over directions of zero strain. Yet there is not a generally accepted definition of a vortex, but to analyse the structural changes in a flow it is necessary to choose a precise mathematical definiton. Within this thesis we will not try to evaluate which criterion one should choose. Instead, we will analyse the structural changes that occur as a result of a specific choice. Besides defining vortices as vorticity extrema, we will mainly consider the widely used Q-criterion by Hunt et al.[29]. The Q-criterion locates regions in a flow where the rotation dominates

the strain, i.e. regions where

$$Q = \frac{1}{2}(\|\mathbf{\Omega}\|^2 - \|\mathbf{S}\|^2) > 0. \tag{2.63}$$

Here $\mathbf{S} = \frac{1}{2}(\nabla\mathbf{u} + \nabla\mathbf{u}^T)$ is the symmetric strain rate tensor, $\mathbf{\Omega} = \frac{1}{2}(\nabla\mathbf{u} - \nabla\mathbf{u}^T)$ is the skew-symmetric vorticity tensor and $\|\mathbf{X}\| = \sqrt{\text{tr}(\mathbf{X}\mathbf{X}^T)}$. In the two dimensional setting we consider in this thesis, the Q-criterion is equivalent the Δ-criterion, the λ_2-criterion [30] and the λ_{ci}-criterion [65]. All of these simplify to the determinant of the velocity gradient being positive, i.e.

$$Q(x, y) = \det(\nabla\mathbf{u}(x, y)) > 0. \tag{2.64}$$

It is possible to construct a planar Hamiltonian system where Q is the governing Hamiltonian function, but a Q-vortex is not defined as a critical point of Q, and the framework we already know from topological fluid dynamics can not be directly applied in this setting. Instead of a feature point for a vortex, the Q-criterion defines a vortex as a region. A bifurcation theory for Q-vortices is presented in Paper I and further developed in Paper II. The overall approach in these papers is similar to the one presented in section 2.2.1. The topological changes of the $Q = 0$ contour curves are analysed by locating structurally unstable flow patterns. Since the analysis makes use of higher order derivatives of Q the following assumption applies throughout the analysis.

Remark 2.5 *We assume that Q is a continuous function with continuous derivatives to the finite order required in our analysis.*

Chapter 3

Bifurcation theory for vortices with application to boundary layer eruption

3.1 Introduction

The primary focus of the paper presented in the following section is to develop a bifurcation theory for Q-vortices. The paper contributes to the field of topological fluid dynamics and expands the framework by including an analysis of topological changes in the vortex structure described by the Q-criterion [29]. The topology of a Q-vortex is completely determined by the topology of the $Q = 0$ level set, that encircles a vortex region with positive Q-value. In the paper, we develop a bifurcation theory for these level curves. The theory describes under which conditions we see creation/destruction and merging/splitting of Q-vortices. It turns out that the critical points again become important in the analysis. This time, it is the critical points of Q that are located exactly on the zero level curves that are the key to locate any structural changes. The main argument in the bifurction analysis is based on the fact that a function near a non-degenerate critical point can be represented in a convenient way by an appropriate choice of local coordinates. This result is known as *the Morse lemma* and can be found in various textbooks, such as [56]. The Morse lemma generalises to functions defined on a differentiable manifold of any dimension, but for the purpose required in this paper, the following version is sufficient.

Theorem 3.1 (The Morse lemma) *Let $V \subseteq \mathbb{R}^2$ be open and let F be a real-valued smooth function on V. If (x_0, y_0) is a non-degenerate critical point for F, then there exists a coordinate chart $(\hat{x}, \hat{y})$ in a neighbourhood U of (x_0, y_0) such that $\hat{x}(x_0, y_0) = 0$, $\hat{y}(x_0, y_0) = 0$ and*

$$F(\hat{x}, \hat{y}) = F(x_0, y_0) \pm \hat{x}^2 \pm \hat{y}^2, \tag{3.1}$$

where the signs depend on the Hessian matrix, H, of F at (x_0, y_0) in the following way.

$$F(\hat{x}, \hat{y}) = F(x_0, y_0) + \hat{x}^2 - \hat{y}^2 \quad \text{if } H_0^F \text{ is indefinite} \tag{3.2}$$

$$F(\hat{x}, \hat{y}) = F(x_0, y_0) + \hat{x}^2 + \hat{y}^2 \quad \text{if } H_0^F \text{ is positive definite} \tag{3.3}$$

$$F(\hat{x}, \hat{y}) = F(x_0, y_0) - \hat{x}^2 - \hat{y}^2 \quad \text{if } H_0^F \text{ is negative definite.} \tag{3.4}$$

Based on the Morse lemma and the Implicit Function Theorem, we prove that there are two different types of local changes in the vortex structure that may occur when the parameter t is varied. We denote these structural changes as *pinching* and *punching* bifurcations. As we want to analyse the flow pattern in cases where the fluid interact with a structure, we extend the theory to include bifurcation points located at a no-slip boundary. The boundary condition implies, however, that any point on no-slip wall is a critical point for Q lying on the zero level curve. To locate any possible bifurcation points we therefore have to perform a higher order derivative test which result in two different types of local changes. We denote these structural changes as *wall-pinching* and *wall-punching* bifurcations.

Besides its primary focus on developing a bifurcation theory for Q-vortices, the paper also contains a substantial analysis of the early stages in boundary layer eruption. This numerical part of our study shows that there is a single codimension two point within our parameter range. This codimension two point correspond to the coalescence of two codimension one bifurcations which are associated with the creation and subsequent destruction of one of the vortices. We extend our theory to include this codimension two phenomenon and show that it occurs at a critical point of Q, where the non-degeneracy condition $\partial_t Q \neq 0$ is violated. In our theoretical description of the phenomenon, we turn the non-degeneracy condition into an additional degeneracy condition by insisting on its violation. With an additional degeneracy condition the bifurcation point will not be robust to variations in other parameters. To represent all possible changes in the vortex structure, it is therefore necessary to introduce a second parameter, r, and analyse the parametric family of level curves $Q(x, y, t, r) = 0$ for sufficiently small variations in (t, r).

The application to the boundary layer eruption problem illustrates how numerical simulations can be interpreted within the framework of our bifurcation

theory. Boundary layer eruption is a classical fluid mechanical problem where a large vortex is convected close to a no-slip wall. The vortex induces some vorticity in the boundary layer, which may erupt and form secondary vortices. We investigate this process at moderate Reynolds numbers in the range from $\mathrm{Re} = 750$ to $\mathrm{Re} = 2250$ and show that boundary layer eruption can be described as sequences of the four possible bifurcations with codimension one. The main result of the numerical part of the study is a bifurcation diagram showing that the final outcome of the evolution is the same: two vortices emerge from the erupting boundary layer for all values of the Reynolds numbers in the considered range. In addition, the bifurcation diagram makes it clear that most of the bifurcations seem very robust to variations in Reynolds numbers. The only exception is the codimension two point that separates the the parameter space in two regions with distinct evolution of the topology of the vortices. The robustness of the process and its simple description in terms of bifurcations call for further studies either with higher Reynolds numbers or a more complex flow geometry. This is exactly what follows in the chapter 4 where our second paper is presented. In this paper, the bifurcation theory is further developed to be able to describe the codimension two phenomenon associated with vortex merging.

3.2 Paper I

The paper in this section is a reprint of the version that has been accepted for publication in Journal of Fluid Mechanics. The original publication can be found here:

Nielsen, A. R., Heil, M., Andersen, M., & Brøns, M. (2019). Bifurcation theory for vortices with application to boundary layer eruption. Journal of Fluid Mechanics, 865(865), 831–849. https://doi.org/10.1017/jfm.2019.97 [47]

We want to make it clear that the paper is partly based on ideas from my master thesis [45] and partly based on results that are original work done during the Ph.D period.

The analysis of the bifurcations with codimension one and the majority of the simulations are results from the master's thesis. The extension of the theory with a codimension two analysis is original work done during the Ph.D period. The same is true for the entire analysis of the numerical results in the context of this new theory. All figures and the final wording of the paper are also made as part of the Ph.D work.

Bifurcation theory for vortices with application to boundary layer eruption

Anne R. Nielsen[1], Matthias Heil[2], Morten Andersen[3] and Morten Brøns[1]

[1]*Department of Applied Mathematics and Computer Science, Technical University of Denmark, 2800 Lyngby, Denmark*

[2]*School of Mathematics, University of Manchester, Oxford Road, Manchester M13 9PL, UK*

[3]*Department of Science and Environment, Roskilde University, 4000 Roskilde, Denmark*

Abstract

We develop a bifurcation theory describing under which conditions vortices are created or destroyed in a two dimensional incompressible flow. We define vortices using the Q-criterion and analyse the vortex structure by considering the evolution of the zero contours of Q. The theory identifies topological changes of the vortex structure and classifies these as four possible types of bifurcations, two occurring away from boundaries, and two occurring near no-slip walls. Our theory provides a description of all possible codimension-one bifurcations where time is treated as the bifurcation parameter. To illustrate our results we consider the early stages of boundary layer eruption at moderate Reynolds numbers in the range from $\mathrm{Re} = 750$ to $\mathrm{Re} = 2250$. By analysing numerical simulations of the phenomenon we show how to describe the eruption process as sequences of the four possible bifurcations of codimension one. Our simulations show that there is a single codimension-two point within our parameter range. This codimension-two point arises at $\mathrm{Re} = 1817$ via the coalescence of two codimension-one bifurcations which are associated with the creation and subsequent destruction of one of the vortices that erupt from the boundary layer. We present a theoretical description of this process and explain how the occurrence of this phenomenon separates the parameter space into two regions with distinct evolution of the topology of the vortices.

1. Introduction

Vortices are coherent structures in a fluid flow, and much of basic fluid dynamics research is focused on understanding their dynamics, interaction, creation and destruction. By our intuitive understanding it might not be difficult to identify a strong vortex in a flow. It is, however, harder to locate its boundaries and to explain how it was created. To answer these questions we need a precise mathematical definition of a vortex. There are many different vortex criteria available in the literature (see Zhang *et al.* (2018) for a review) and new ideas are continuously being proposed, e.g. Haller *et al.* (2016) and Zhong *et al.* (2017). Each of these criteria identify different structures as vortices and as yet there is no generally accepted definition of a vortex. In the present paper we identify vortices based on the widely used Q-criterion (Hunt *et al.* 1988). The Q-criterion locates regions in a flow where the rotation dominates the strain. As a variety of other Galilean-invariant vortex criteria it is based on a decomposition of the velocity gradient tensor, $\nabla\mathbf{u}$. In its general form, Q is defined as the following measure of stretching relative to

rotation,

$$Q = \frac{1}{2}(\|\boldsymbol{\Omega}\|^2 - \|\mathbf{S}\|^2), \tag{1.1}$$

where $\mathbf{S} = \frac{1}{2}(\nabla\mathbf{u} + \nabla\mathbf{u}^T)$ is the symmetric strain rate tensor, $\boldsymbol{\Omega} = \frac{1}{2}(\nabla\mathbf{u} - \nabla\mathbf{u}^T)$ is the skew-symmetric vorticity tensor and $\|\mathbf{X}\| = \sqrt{\mathrm{tr}(\mathbf{X}\mathbf{X}^T)}$. The criterion defines a vortex as a region with positive Q-value. In a two dimensional setting the Q-criterion is equivalent to other frequently used vortex criteria such as the Δ-criterion, the λ_2-criterion (Jeong & Hussain 1995) and the λ_{ci}-criterion (Zhou *et al.* 1999). All of these simplify to the determinant of the velocity gradient being positive, i.e.

$$Q(x, y) = \det\left(\nabla\mathbf{u}(x, y)\right) > 0. \tag{1.2}$$

In practice it is common to choose a non-zero threshold to identify the vortex boundaries. The threshold is ideally chosen such that strong vortices are captured while small spurious vortices (e.g. those arising as artefacts in data from numerical simulations) are ignored. Unfortunately, it is very difficult, if not impossible, to determine a suitable threshold value *a priori* because the optimal threshold value tends to be problem dependent (see Chen *et al.* (2015) and Chakraborty *et al.* (2005)). In this paper we therefore consider the Q-criterion with zero threshold as defined in (1.2).

Having established a criterion that identifies vortices in a precise mathematical way, we employ bifurcation theory to analyse under which conditions vortices are created, destroyed, merge or split. This is done by considering Q as a function of time, t, which we treat as the primary bifurcation parameter. The main result of our studies is a detailed analysis of the creation, destruction or merging of vortices in terms of changes in the topology of the level set $Q = 0$. Previous topological studies of bifurcations of structures in flows have focused on critical points for either the velocity (see e.g. Brøns 2007; Balci *et al.* 2015) or the vorticity (Brøns & Bisgaard 2006; Heil *et al.* 2017). Here we are concerned with bifurcations of curves rather than critical points, and a different mathematical approach is needed. The overall strategy is, however, the same: A bifurcation is characterized by a number of degeneracy conditions which state that certain combinations of derivatives of Q must be zero. These are combined with non-degeneracy conditions which are inequalities ensuring that certain higher-order derivatives are non-zero. The degeneracy conditions are equations that make it possible to locate a bifurcation point. To be able to determine where in space and time a certain bifurcation occurs, three degeneracy conditions are needed. The non-degeneracy conditions ensure a certain regularity of the Q function allowing us to employ the Implicit Function Theorem to determine the properties of the level curve $Q = 0$ close to the bifurcation point. The bifurcations obtained in this way are denoted codimension-one bifurcations. If an additional parameter, such as the Reynolds number Re, is varied, one of the non-degeneracy conditions may be violated at a given value of that parameter. Subject to further non-degeneracy conditions, a two-parameter bifurcation diagram can be established, and the bifurcation is then said to have codimension two. Adding more parameters, this procedure can then be repeated, but the number of possible bifurcations and the complexity of the bifurcation diagrams increase rapidly with the codimension.

In the present paper we obtain a complete list of codimension-one bifurcations. There are four types, *Pinching* and *punching* bifurcations occur away from boundaries, while *wall-pinching* and *wall-punching* are bifurcations of vortices attached to a no-slip wall.

To illustrate how our theory can be used, we apply it to the classical fluid mechanics problem of boundary layer eruption. In this problem a large vortex is convected close to a no-slip wall. This vortex induces vorticity in the boundary layer which may, or may

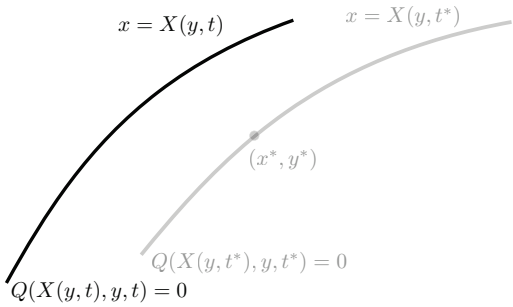

Figure 1: Illustration of how a small change in time away from t^* affects the topological structure of the contour curve, $Q = 0$, close to a non-critical point (x^*, y^*). Since the topological structure is unchanged, (x^*, y^*) is not a bifurcation point.

not, erupt and form secondary vortices. This process has previously been studied by Doligalski & Walker (1984), Obabko & Cassel (2002), Kudela & Malecha (2009) and Andersen (2013) among others. We consider the early stages of boundary layer eruption at moderate Re. By tracking the flow structures for fixed Re we show that our approach allows a rigorous description of the creation of vortices as a series of bifurcations of the zero contours of Q. The bifurcations are generally of codimension one, but a single codimension-two point is found. The corresponding value of Re marks a change in the topology of the vortex pattern, and in an appendix we provide a detailed analysis of this case.

2. Bifurcations of $Q = 0$ curves away from boundaries

We start by considering a region of fluid which is not in the vicinity of any boundary. Our goal is to characterize under which conditions we see topological changes in the local structure of the zero contour curves of Q. As a starting point we consider a non-critical point on the zero contour curve, i.e. a point (x^*, y^*, t^*), where

$$Q(x^*, y^*, t^*) = 0 \tag{2.1}$$

and

$$\partial_x Q(x^*, y^*, t^*) \neq 0 \quad \text{or} \quad \partial_y Q(x^*, y^*, t^*) \neq 0. \tag{2.2}$$

In the case where $\partial_x Q(x^*, y^*, t^*)$ is non-zero it follows from the Implicit Function Theorem that there exist a unique local function $X(y,t) = x$ satisfying $X(y^*, t^*) = x^*$ and $Q(X(y,t), y, t) = 0$. The uniqueness of X implies that we only have a single zero contour curve close to (x^*, y^*) at time $t = t^*$. Furthermore, the continuity of X guarantees that the zero contour curve will not change its topological structure for any sufficiently small changes in time, as illustrated in figure 1. We therefore conclude that (x^*, y^*) cannot be a bifurcation point at time t^*. If we consider the case where $\partial_x Q(x^*, y^*, t^*) = 0$ we can give a completely similar argument based on the fact that $\partial_y Q(x^*, y^*, t^*)$ is non-zero. This implies that we must look for critical points of Q to identify any possible bifurcation points on the zero contour curve.

For simplicity we choose a coordinate system such that the critical point is located at $(x, y) = (0, 0)$ at time $t = 0$ and we use subscript 0 to denote any function evaluation at $(x, y, t) = (0, 0, 0)$. Based on the discussion above, bifurcation points must fulfil

$$Q_0 = 0, \;\; \partial_x Q_0 = 0, \;\; \partial_y Q_0 = 0. \tag{2.3}$$

If the Hessian matrix is non-singular at $(x, y, t) = (0, 0, 0)$, it can be used to classify the type of critical point. Hence we take as the first non-degeneracy condition

$$H_0^Q = \begin{pmatrix} \partial_{xx} Q_0 & \partial_{xy} Q_0 \\ \partial_{xy} Q_0 & \partial_{yy} Q_0 \end{pmatrix} \text{ is non-singular.} \tag{2.4}$$

As the second non-degeneracy condition we assume

$$\partial_t Q_0 \neq 0, \tag{2.5}$$

which will be needed to apply the Implicit Function Theorem later in the analysis.

Based on the above assumptions, we will now show that a bifurcation occurs at $(x, y, t) = (0, 0, 0)$. Applying that $Q_0 = 0$ and $\partial_t Q_0 \neq 0$, it follows from the Implicit Function Theorem that there exist a unique local function $T(x, y) = t$ satisfying that $T_0 = T(0, 0) = 0$ and $Q(x, y, T(x, y)) = 0$. The equation $t = T(x, y)$, for a given t, will therefore determine the zero contour curve of Q at that time. In order to characterize the topological structure of the contour curves we need some properties of the function T. By implicit differentiation of Q, we obtain that

$$\partial_x T_0 = -\frac{\partial_x Q_0}{\partial_t Q_0} = 0, \quad \partial_y T_0 = -\frac{\partial_y Q_0}{\partial_t Q_0} = 0 \tag{2.6}$$

and the Hessian

$$H_0^T = \begin{pmatrix} \partial_{xx} T_0 & \partial_{xy} T_0, \\ \partial_{xy} T_0 & \partial_{yy} T_0 \end{pmatrix} = -\frac{1}{\partial_t Q_0} H_0^Q. \tag{2.7}$$

Equation (2.6) shows that $(x, y) = (0, 0)$ is a critical point for T. Since $\partial_t Q_0$ is nonzero and H_0^Q is non-singular, it follows from (2.7) that H_0^T is also non-singular and the critical point is therefore a saddle point, a local maximum or a local minimum. With these conditions we can apply the Morse Lemma (Wiggins 2003) on T and conclude that in a neighbourhood of the critical point there exists a, possibly nonlinear, coordinate change, $\hat{x} = \hat{x}(x, y)$, $\hat{y} = \hat{y}(x, y)$, such that

$$\hat{x}(0, 0) = 0, \quad \hat{y}(0, 0) = 0 \tag{2.8}$$

and

$$T(\hat{x}, \hat{y}) = \hat{x}^2 + \hat{y}^2 \qquad \text{if } H_0^T \text{ is positive definite,} \tag{2.9a}$$

$$T(\hat{x}, \hat{y}) = -\hat{x}^2 - \hat{y}^2 \qquad \text{if } H_0^T \text{ is negative definite,} \tag{2.9b}$$

$$T(\hat{x}, \hat{y}) = \hat{x}^2 - \hat{y}^2 \qquad \text{if } H_0^T \text{ is indefinite.} \tag{2.9c}$$

These three cases correspond to the critical point being a local maximum, a local minimum or a saddle point of T. We now consider these cases in separate sections.

2.1. H_0^Q *definite: punching bifurcation*

First we consider the case where H_0^Q is positive or negative definite. We see from (2.7) that H_0^T is definite as well. In order to determine if H_0^T is positive or negative definite, we consider the sign of the trace of H_0^T,

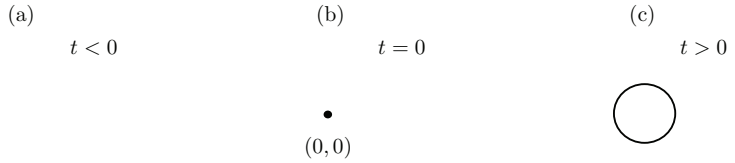

Figure 2: Illustration of the local changes in structure of the $Q = 0$ contour curve during a punching bifurcation. The figure shows the forward version where $\text{sign}(\partial_t Q_0) \neq \text{sign}(\text{tr}(H_0^Q))$. At the bifurcation value $t = 0$, $(0, 0)$ is the only point where $Q = 0$.

$$\text{sign}(\text{tr}(H_0^T)) = -\text{sign}(\partial_t Q_0)\text{sign}(\text{tr}(H_0^Q)). \tag{2.10}$$

In the case where $\text{sign}(\partial_t Q_0) \neq \text{sign}(\text{tr}(H_0^Q))$, H_0^T is positive definite and it follows from $(2.9a)$ that in a neighbourhood of $(0, 0)$ there exists a coordinate system $(\hat{x}, \hat{y})$ where the zero contour curve of Q is given by

$$T(\hat{x}, \hat{y}) = \hat{x}^2 + \hat{y}^2 = t. \tag{2.11}$$

For $t < 0$, the right-hand side of (2.11) is negative. In this case there cannot be any point $(\hat{x}, \hat{y})$ close to $(0, 0)$ which is part of the zero contour curve of Q. This situation is illustrated in figure 2 (a). For $t = 0$ the only possible solution to this equation is $(\hat{x}, \hat{y}) = (0, 0)$. In the original coordinates this solution corresponds to the critical point. The zero contour curve of Q at $t = 0$ is therefore only a single point as illustrated in figure 2 (b). On the other hand, if $t > 0$, the right-hand side of (2.11) is positive and the solution curve is a circle with radius $\sqrt{t}$. If t is chosen sufficiently close to 0 we ensure the circle is contained in the neighbourhood where T is defined. In this case the zero contour curve of Q is topologically equivalent to the illustration in figure 2 (c). We will denote this kind of local changes in the structure a *punching bifurcation* of the contour curve, since the graph of Q punches through the level $Q = 0$ at the bifurcation point. From a physical point of view a punching bifurcation corresponds to a vortex being created at the bifurcation point. We notice, however, that the result does not tell us anything about the sign of Q inside the zero contour. A punching bifurcation could therefore also correspond to the creation of a "hole" inside a vortex region. It is easy to see that the two different scenarios are distinguished by the sign of $\partial_t Q_0$.

If we instead consider the case where $\text{sign}(\partial_t Q_0) = \text{sign}(\text{tr}(H_0^Q))$, then H_0^T is negative definite and there exists a coordinate system $(\hat{x}, \hat{y})$ where the zero contour curve of Q is given as

$$T(\hat{x}, \hat{y}) = -\hat{x}^2 - \hat{y}^2 = t, \tag{2.12}$$

or equivalently,

$$-T(\hat{x}, \hat{y}) = \hat{x}^2 + \hat{y}^2 = -t. \tag{2.13}$$

We notice that this equation is similar to (2.11) except for the sign of t. The change of sign gives us the time-reversed dynamics. By an analysis completely similar to the one above, a punching bifurcation happens at the critical point but in this case the bifurcation happens "backwards" meaning that a vortex disappears at the bifurcation point.

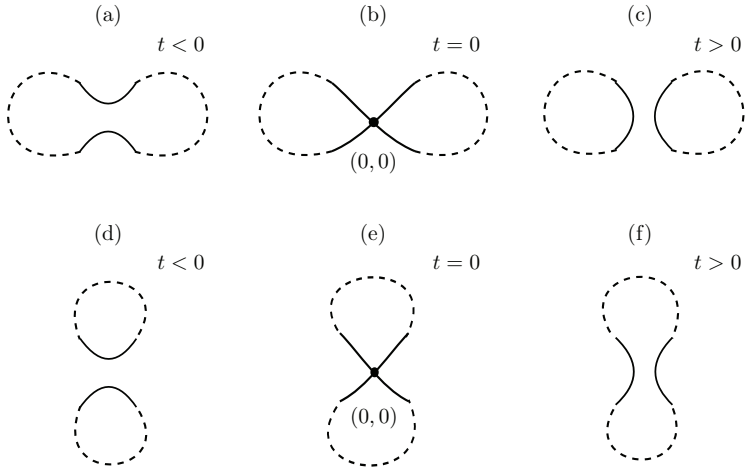

Figure 3: Illustration of the local changes in structure of the $Q = 0$ contour curves during a pinching bifurcation. The solid lines illustrate the topology in a neighbourhood of the bifurcation point $(0, 0)$. The dashed lines in Figs. (a-c) show an example of a possible global structure for the case where the bifurcation results in the splitting of a single vortex into two; Figs. (d-f) illustrate the case when two vortices merge.

It is worth noting that the above analysis is done in the $(\hat{x}, \hat{y})$-coordinate system. In the original coordinates the topology is the same but the vortex would instead approximately be an ellipse. The shape and orientation of this ellipse can be determined by the eigenvalues and eigenvectors of H_0^Q.

2.2. H_0^Q *indefinite: pinching bifurcation*

Now we consider the case where H_0^Q is indefinite. Then H_0^T is also indefinite according to (2.7). It follows from (2.9c) that in a neighbourhood of $(0, 0)$ there exists a coordinate system $(\hat{x}, \hat{y})$ where the zero contour curve of Q is given by

$$T(\hat{x}, \hat{y}) = \hat{x}^2 - \hat{y}^2 = t. \tag{2.14}$$

For $t < 0$, the solution to this equation is a hyperbola with the $\hat{y}$-axis as the principal axis; the zero contour curve of Q is illustrated in figure 3 (a). At $t = 0$ the solution is the pair of straight lines given by $\hat{y} = \hat{x}$ and $\hat{y} = -\hat{x}$ which intersect at $(0, 0)$ as shown in figure 3 (b). If $t > 0$, the solution curve is a hyperbola with the $\hat{x}$-axis as the principal axis; see figure 3 (c) for a sketch of the zero contour curve of Q. We will denote this kind of local change in structure a *pinching bifurcation* of the $Q = 0$ curve. The dashed lines in figures 3(a-c) illustrate how the pinching bifurcation can represent a vortex splitting into two. If the local level curves are connected globally up/down rather than left/right, the bifurcation represents the merging of two vortices, as shown in figures 3(d-f).

3. Bifurcations of $Q = 0$ curves at a no-slip boundary

In this section we consider a region of a fluid where a stationary no-slip boundary is present. We aim to describe under which conditions the zero contours of Q occur and how they erupt from that boundary. For simplicity we consider a boundary which coincides with the x-axis. The theory can easily be generalized to any boundary described by a smooth curve. We choose the coordinate system such that fluid is present in the region where $y > 0$. The imposed no-slip conditions are then given by

$$\begin{aligned} u(x,0,t) &= \partial_y \psi(x,0,t) = 0, \\ v(x,0,t) &= -\partial_x \psi(x,0,t) = 0, \end{aligned}$$

where ψ is the stream function. We notice that the velocities do not change along the boundary and all the higher order derivatives in the x direction are therefore equal to zero,

$$\partial_{xx}\psi(x,0,t) = \partial_{xxx}\psi(x,0,t) = \partial_{xxxx}\psi(x,0,t) = \cdots = 0, \tag{3.1}$$

and

$$\partial_{xy}\psi(x,0,t) = \partial_{xxy}\psi(x,0,t) = \partial_{xxxy}\psi(x,0,t) = \cdots = 0. \tag{3.2}$$

Since the Q-value is defined as the determinant of the velocity gradient it can be expressed in terms of the stream function as

$$Q(x,y,t) = \partial_{yy}\psi(x,y,t)\partial_{xx}\psi(x,y,t) - \partial_{xy}\psi(x,y,t)^2. \tag{3.3}$$

From this expression it is clear that $Q(x,0,t) \equiv 0$, implying that any point on a no-slip boundary will be part of the zero contour curve for Q at any time t. By differentiating (3.3) and exploiting that the higher order derivatives in (3.1) and (3.2) are zero, we find that

$$\partial_x Q(x,0,t) = 0, \quad \text{and} \quad \partial_y Q(x,0,t) = 0, \tag{3.4}$$

and

$$\det\left(H^Q(x,0,t)\right) = \partial_{xx}Q(x,0,t)\partial_{yy}Q(x,0,t) - \partial_{xy}Q(x,0,t)^2 = 0. \tag{3.5}$$

Thus, for any time t, every point on a no-slip boundary is a critical point for Q lying on the zero contour curve. Since the second derivative test is inconclusive according to (3.5), we need to perform a higher order derivative test in order to locate possible bifurcation points. By Taylor's Theorem with integral remainder, we have for any fixed x and any fixed t

$$\begin{aligned} Q(x,y,t) &= Q(x,0,t) + \partial_y Q(x,0,t)y + \widetilde{Q}(x,y,t)y^2 \\ &= \widetilde{Q}(x,y,t)y^2, \end{aligned} \tag{3.6}$$

where $\widetilde{Q}$ is the continuous function defined as

$$\widetilde{Q}(x,y,t) = \int_0^1 \partial_{yy} Q(x, y(1-s), t)s \, \mathrm{d}s. \tag{3.7}$$

From (3.6) we notice that $Q = 0$ if $y = 0$ or if $\widetilde{Q} = 0$. We can therefore determine the non-boundary part of the line where $Q = 0$ by finding the zero contour curve of $\widetilde{Q}$. Furthermore, we see that the sign of Q is determined by the sign of $\widetilde{Q}$ for $y \neq 0$. A region with positive $\widetilde{Q}$-value is therefore classified as a vortex region. Hence, we will focus on the characteristics of $\widetilde{Q}$ instead of Q. We are especially interested in finding the zeros of $\widetilde{Q}$ and it is therefore natural to ask under which physical conditions $\widetilde{Q}$ actually has zeros

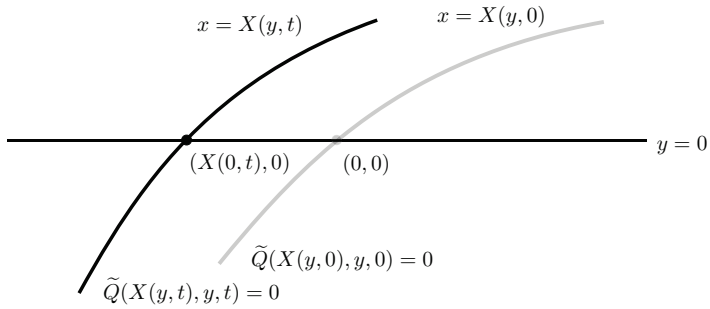

Figure 4: Illustration of how a small change in time affects the topological structure of the contour curve, $\widetilde{Q} = 0$, close to a non-critical boundary point $(0,0)$. Since the topological structure is unchanged, $(0,0)$ is not a bifurcation point.

on the boundary. Since

$$\omega(x,0,t) = -\nabla^2\psi(x,0,t) = -\partial_{yy}\psi(x,0,t), \tag{3.8}$$

it follows from (3.7) and (3.3) that

$$\begin{aligned}\widetilde{Q}(x,0,t) &= \frac{1}{2}\partial_{yy}Q(x,0,t)\\ &= \frac{1}{2}\partial_{yy}\psi(x,0,t)\partial_{xxyy}\psi(x,0,t) - \partial_{xyy}\psi(x,0,t)^2\\ &= \frac{1}{2}\omega(x,0,t)\partial_{xx}\omega(x,0,t) - \partial_x\omega(x,0,t)^2.\end{aligned} \tag{3.9}$$

This shows that $\widetilde{Q}$ on the boundary depends only on the vorticity and its derivatives along the boundary. Hence, bifurcations of $Q = 0$ at the wall can be expressed in terms of the vorticity. There is no similar connection between Q and ω away from the boundary. In the rest of this section we consider zero points of $\widetilde{Q}$ on the boundary and prove under which conditions these correspond to bifurcation points of the zero contour curves of Q. For simplicity we choose a coordinate system such that zero points are located at $(x,y) = (0,0)$ at time $t = 0$ and, as before, we use the subscript 0 to denote any function evaluation at $(x,y,t) = (0,0,0)$. First we consider a point on the no-slip boundary satisfying

$$\widetilde{Q}_0 = 0, \tag{3.10}$$

$$\partial_x\widetilde{Q}_0 \neq 0. \tag{3.11}$$

By the Implicit Function Theorem it then follows that there exists a unique local function $X(y,t) = x$ satisfying $X(0,0) = 0$ and $\widetilde{Q}(X(y,t),y,t) = 0$. The continuity of X implies that, for any fixed t sufficiently close to $t = 0$, there is a unique curve $x = X(y,t)$, which intersects the boundary at $(x,y) = (X(0,t),0)$. Since $\widetilde{Q} = 0$ along this curve, it follows that for any t sufficiently close to $t = 0$ the zero contour curve of $\widetilde{Q}$ has a unique intersection with the boundary in a neighbourhood of $(x,y) = (0,0)$. Figure 4 illustrates how the zero contour of $\widetilde{Q}$ will maintain its intersection with the boundary for sufficiently small changes in time. To identify possible bifurcation points, we must therefore consider

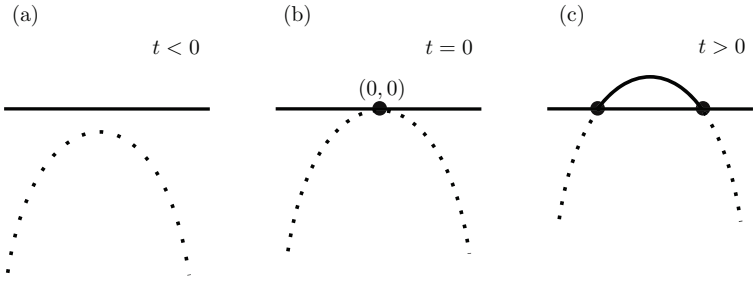

Figure 5: Illustration of the local changes in structure under a wall-punching bifurcation. The figure illustrates the forward version where $\text{sign}(\partial_t \widetilde{Q}_0) \neq \text{sign}(\partial_y \widetilde{Q}_0)$. The solid lines are the visible zero contour curves of Q, while the dotted lines are outside the region containing the fluid.

a boundary point $(x, y) = (0, 0)$ satisfying that

$$\widetilde{Q}_0 = 0, \quad \partial_x \widetilde{Q}_0 = 0. \tag{3.12}$$

To characterize bifurcations of codimension one we assume that $\widetilde{Q}$ satisfies the simplest non-degeneracy conditions

$$\partial_y \widetilde{Q}_0 \neq 0, \quad \partial_{xx} \widetilde{Q}_0 \neq 0, \quad \text{and} \quad \partial_t \widetilde{Q}_0 \neq 0. \tag{3.13}$$

At such a point it follows from the Implicit Function Theorem that there exists a unique local function $Y(x, t) = y$ such that $Y_0 = Y(0, 0) = 0$ and $\widetilde{Q}(x, Y(x, t), t) = 0$. This implies that for any fixed t sufficiently close to $t = 0$, the zero contour curve of $\widetilde{Q}$ is given by the unique curve $y = Y(x, t)$. By implicitly differentiating $\widetilde{Q}$, we obtain that

$$\partial_x Y_0 = -\frac{\partial_x \widetilde{Q}_0}{\partial_y \widetilde{Q}_0} = 0 \tag{3.14}$$

and

$$\partial_t Y_0 = -\frac{\partial_t \widetilde{Q}_0}{\partial_y \widetilde{Q}_0} \neq 0 \qquad \partial_{xx} Y_0 = -\frac{\partial_{xx} \widetilde{Q}_0}{\partial_y \widetilde{Q}_0} \neq 0. \tag{3.15}$$

Equations (3.14) and (3.15) show that the local behaviour of Y around $(x, t) = (0, 0)$ will now depend on the sign of the terms $\partial_y \widetilde{Q}_0$, $\partial_{xx} \widetilde{Q}_0$ and $\partial_t \widetilde{Q}_0$. In the two sections below we consider the case where $\partial_{xx} \widetilde{Q}_0$ and $\partial_y \widetilde{Q}_0$ have the same sign and and the case where their signs are different. As we will see these cases result in two different types of bifurcations.

3.1. *Wall-punching bifurcation*

We first consider the case where

$$\text{sign}(\partial_{xx} \widetilde{Q}_0) = \text{sign}(\partial_y \widetilde{Q}_0). \tag{3.16}$$

Furthermore, we assume that $\partial_t \widetilde{Q}_0$ has the opposite sign of $\partial_{xx} \widetilde{Q}_0$ and $\partial_y \widetilde{Q}_0$. Then $\partial_{xx} Y_0 < 0$ and there is an interval around $x = 0$ where $Y(x, 0)$ is a strictly concave function with maximum value in $x = 0$. The corresponding zero contour curve of Q is

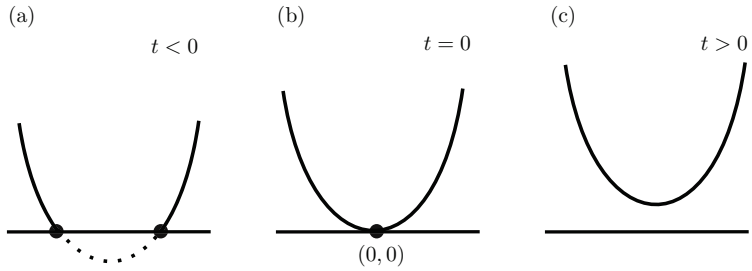

Figure 6: Illustration of the local changes in structure under a wall-pinching bifurcation. The figure illustrates the forward version where $\text{sign}(\partial_t \widetilde{Q}_0) \neq \text{sign}(\partial_y \widetilde{Q}_0)$. The solid lines are the visible zero contour curves of Q, while the dotted line is outside the region containing the fluid.

illustrated in figure 5(b). To investigate what happens to the curve for $t \neq 0$ we apply the Implicit Function Theorem yet again. By the conditions in (3.14) and (3.15) there exists a unique function $T(x) = t$, such that $T_0 = T(0) = 0$ and $Y(x, T(x)) = 0$ for any x sufficiently close to 0. By implicit differentiation of Y, we obtain that

$$\partial_x T_0 = -\frac{\partial_x Y_0}{\partial_t Y_0} = 0 \quad \text{and} \quad \partial_{xx} T_0 = -\frac{\partial_{xx} Y_0}{\partial_t Y_0} > 0.$$

These conditions imply that T is a strictly convex function with minimum value at $x = 0$. Hence, there are no solutions to the equation $T(x) = t$ if $t < 0$ and two solutions if $t > 0$. Since T is a unique function we conclude that in a neighbourhood of $x = 0$, Y has no zero points for $t < 0$ and two zero points for $t > 0$. These two scenarios are illustrated in figure 5(a) and 5(c). The structural change we observe corresponds to the zero contour of $\widetilde{Q}$ breaking through the boundary at the bifurcation point $(x, y, t) = (0, 0, 0)$. We denote this kind of structural change a *wall-punching bifurcation*. From a physical point of view, a wall-punching bifurcation corresponds to a vortex being created attached to the wall. If we instead consider the situation where

$$\text{sign}(\partial_{xx} \widetilde{Q}_0) = \text{sign}(\partial_y \widetilde{Q}_0) = \text{sign}(\partial_t \widetilde{Q}_0), \tag{3.17}$$

an entirely similar argument shows that the wall-punching bifurcation will occur backwards and describes the case where a vortex disappears through the boundary.

3.2. *Wall-pinching bifurcation*

So far we have only considered the case where (3.16) is satisfied. If we instead consider the case where

$$\text{sign}(\partial_{xx} \widetilde{Q}_0) \neq \text{sign}(\partial_y \widetilde{Q}_0), \tag{3.18}$$

$Y(x, 0)$ is strictly convex. From arguments similar to the above it is easy to prove that if $\text{sign}(\partial_t \widetilde{Q}_0) \neq \text{sign}(\partial_y \widetilde{Q}_0)$, the zero contour curve will intersect the wall in two points for $t < 0$ and will pinch off the wall for $t > 0$, as shown in figure 6. For $\text{sign}(\partial_t \widetilde{Q}_0) = \text{sign}(\partial_y \widetilde{Q}_0)$ the reverse change occurs. We denote this type of structural change a *wall-pinching bifurcation*. From a physical point of view a wall-pinching bifurcation corresponds to a vortex detaching from or attaching to the wall.

4. Degeneracies and codimension-two bifurcations

In the previous sections we have provided a complete analysis of all possible bifurcations of codimension one, i.e. bifurcations that occur at a specific value of the bifurcation parameter which we chose to be time. Each of the four bifurcations occur under a specific set of degeneracy conditions (equalities) and non-degeneracy conditions (inequalities). The non-degeneracy conditions may, of course, turn out to be violated. To determine under which conditions this occurs we turn the relevant non-degeneracy condition into an additional degeneracy condition by insisting on its violation. This imposition then provides an additional equation that allows us to determine particular values of some additional parameter (e.g. the Reynolds number) at which this degeneracy occurs. Such points are known as codimension two points because they require two parameters (here time and the Reynolds number) to take on particular values for the degenerate behaviour to occur.

For the bifurcations away from boundaries the non-degeneracy conditions (2.4) and (2.5) require that the Hessian of Q is non-singular and that $\partial_t Q_0 \neq 0$, respectively. In Appendix A we analyse the case where the second non-degeneracy condition is broken, such that the degeneracy conditions are

$$Q_0 = \partial_x Q_0 = \partial_y Q_0 = \partial_t Q_0 = 0. \tag{4.1}$$

The first non-degeneracy condition is kept, and other conditions will be imposed to allow the use of the Implicit Function Theorem. We choose this case as it appears in the application we study below. The analysis shows that close to the codimension-two point (t_0, Re_0) there is a bifurcation curve in the (t, Re) parameter plane given by

$$\mathrm{Re} = \mathrm{Re}_0 + C(t - t_0)^2 + \mathcal{O}(t^3), \tag{4.2}$$

where C is a constant. If $C > 0$, and Re is slightly larger than Re_0, there are punching bifurcations when the bifurcation curve is crossed, i.e. when $t = t_0 \pm \sqrt{\mathrm{Re} - \mathrm{Re}_0}/\sqrt{C} + \mathcal{O}(\mathrm{Re} - \mathrm{Re}_0)$. The first crossing is the creation of a vortex by a punching bifurcation, the latter is the destruction of a vortex by a backward punching bifurcation. If $\mathrm{Re} < \mathrm{Re}_0$ the bifurcation curve is not crossed, and no bifurcations occur near t_0.

5. Application to boundary layer eruption

5.1. *Problem setup*

As a case study we consider a vortex convected close to a no-slip wall. Such a vortex induces a viscous response from the boundary layer close to the wall. The vorticity in the boundary layer may organise itself into new vortex structures that erupt from the surface. This phenomenon is known as boundary layer eruption (Kudela & Malecha 2009), unsteady separation (Williams 1977) or bursting (Robinson 1991). To give a mathematical formulation of the phenomenon we choose a coordinate system fixed to the no-slip wall as shown in figure 7. The initial configuration is a Gaussian vortex with characteristic length c and negative vorticity $-\omega_0$ at the vortex center. The Gaussian vortex is placed at distance d from the wall and an image vortex with opposite vorticity is placed below the wall. Due to symmetry the velocity field satisfies the non-penetration condition on the wall. A boundary layer is created when, at $t = 0$, we impose the no-slip condition. We non-dimensionalize our problem by choosing the reference length $L = d$ and the reference velocity $U = \frac{1}{2}\omega_0 c$. For our choice of non-dimensionalization the Reynolds

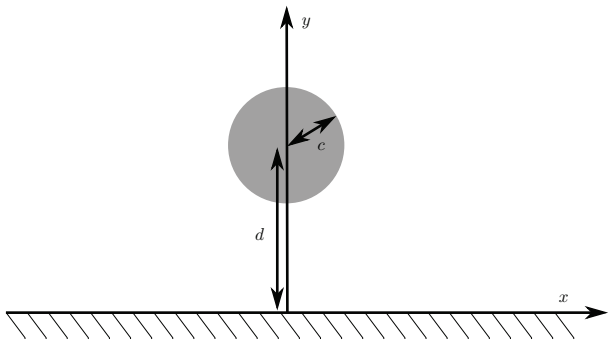

Figure 7: Initial configuration of the boundary layer eruption problem. A Gaussian vortex is placed at a distance d from the no-slip wall. c is the characteristic length for the Gaussian distribution.

number is given by

$$\mathrm{Re} = \frac{LU}{\nu} = \frac{\omega_0 dc}{2\nu}, \tag{5.1}$$

where ν is the kinematic viscosity of the fluid. We specify the initial vortex by the dimensionless parameter a that represents the ratio between the size of the initial vortex and the distance to the wall, i.e. $a = \frac{c}{d}$. In order to be consistent with earlier studies by Kudela & Malecha (2009) and Andersen (2013) we have chosen the parameter value $a = 0.3$. We note that our choice of non-dimensionalization gives us a Reynolds number that is a scaled version of the Reynolds number, $\widehat{\mathrm{Re}}$, used by Kudela & Malecha (2009) and Andersen (2013). The scaling is $\mathrm{Re} = \frac{1}{2}\Omega_0 a\widehat{\mathrm{Re}}$, with $\Omega_0 = 1.25$.

5.2. *Numerical method*

We performed our numerical simulations using the open-source finite element-library `oomph-lib` (Heil & Hazel 2006), dicretising the Navier-Stokes equations with LBB-stable quadrilateral Taylor-Hood (Q2Q1) elements and employing a BDF2 scheme for the time-integration. The vortex-wall interaction results in a net advection of the initial vortex in the negative x-direction. To avoid the need for a large computational domain we performed the computations in a domain that moves steadily with the initial velocity of the advecting vortex. This allowed us to restrict the computational domain to the region $x \in [-3.63, 3.63]$ and $y \in [0, 5.13]$. The computations were started from an initial velocity field given by the Gaussian vortex and its mirror image below the y-axis. During a short initial period we only enforced the non-penetration condition and then imposed the no-slip condition on the wall to initiate the formation of the boundary layer. On the remaining boundaries we imposed the velocity associated with the initial vortex (corrected for the moving frame of reference). To resolve the boundary layer we decomposed the mesh into two regions: within a thin layer close to the wall we decreased the distance between the mesh points exponentially towards the wall; a uniform mesh spacing was used in the rest of the domain. The Q-field and its derivatives were computed using `oomph-lib`'s (Heil & Hazel 2006) derivative recovery techniques to obtain smooth approximations of the required derivatives (see Heil *et al.* (2017) for details). To confirm

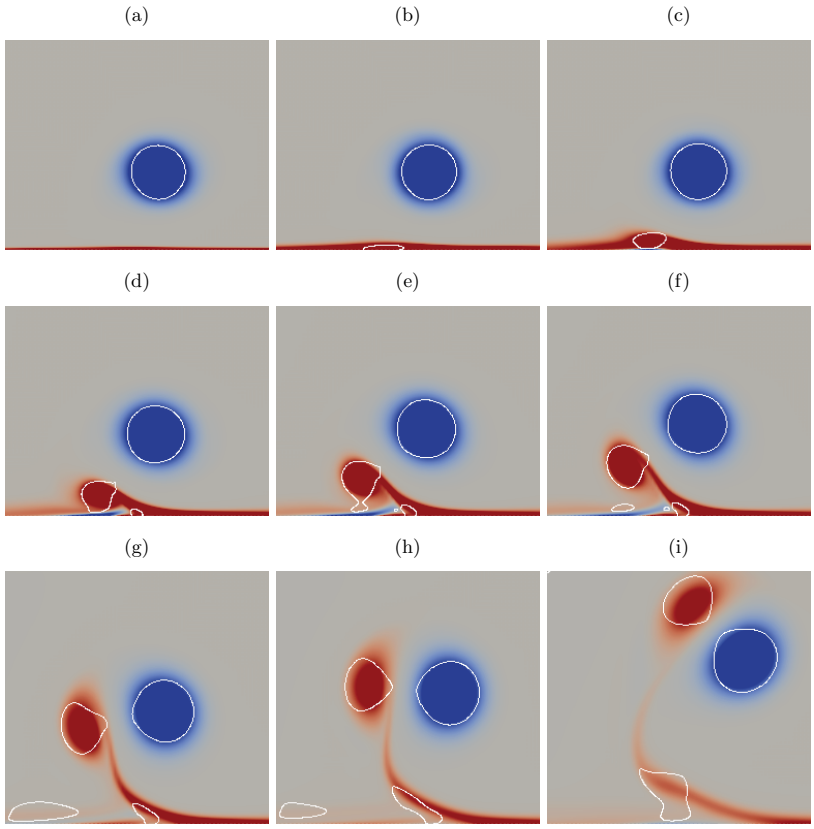

Figure 8: Numerical results for Re = 2063 at the following time steps (a) $t = 11$ (b) $t = 48$ (c) $t = 117$ (d) $t = 197$ (e) $t = 256$ (f) $t = 293$ (g) $t = 395$ (h) $t = 464$ (i) $t = 597$. Each figure shows a zoom in on the region close to the initial vortex, where $x \in [-2, 1.5]$. The vorticity contours with values from -0.3 to 0.3 are colored in blue and red. Regions with positive Q-value are encircled by white lines which correspond to the zero contour curves of Q.

that our results were fully converged we recomputed selected cases on refined meshes and with smaller time steps.

5.3. *Numerical results*

We simulated the early stages of boundary layer eruption at moderate Reynolds numbers in the range between Re = 750 and Re = 2250. Figure 8 shows snapshots from a simulation with Re = 2063. The zero contour curves of Q are drawn on top of the vorticity field to provide a basis for comparison. Each of the nine subfigures represents a topological vortex structure observed in the simulation. In figure 8(a) the initial vortex

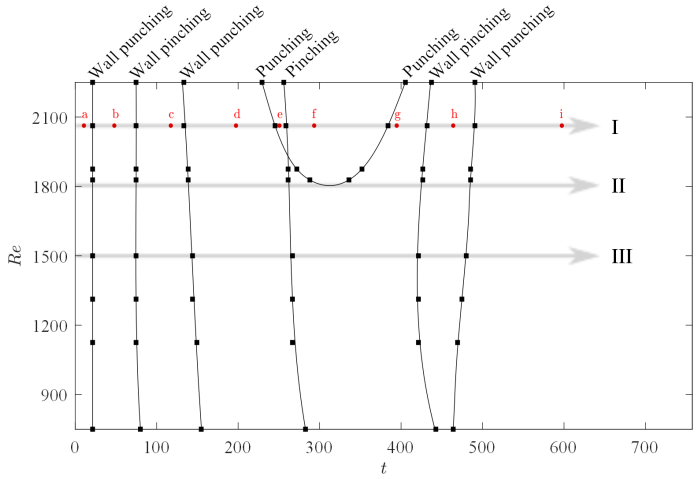

Figure 9: Bifurcation diagram of the eruption process. The red dots marked with a letter correspond to the plots shown in figure 8. The black squares, connected by solid lines, mark the bifurcation points observed in the simulations. The translucent arrows indicate in which sequence the bifurcations are encountered in a flow with a given Reynolds number.

is the only region with positive Q-value. At this early stage the shape of the vortex is very close to a perfect circle. This is consistent with a result by Elsas & Moriconi (2017), who showed that a Gaussian vortex will have a positive Q-value in a circular region with radius $r \approx \frac{c}{0.89}$. For a Gaussian vortex, the radius grows like $\sqrt{t}$, which is identical to the initial growth rate we found for a vortex generated in a punching bifurcation (see §2).

The overall changes in the vortex structure in figure 8 can be described as eight separate bifurcations of the zero contour curves. In the time span between (a) and (b) we see an example of a wall-punching bifurcation that causes a new vortex to form in the boundary layer. In (c) this new vortex has detached from the wall as the result of a wall-pinching bifurcation. After another wall-punching bifurcation a second vortex is formed in the boundary layer, as shown in (d). In the time span between (d) and (e) a punching bifurcation takes place and a small vortex develops in the part of the boundary layer with negative vorticity. Between (e) and (f) we observe a pinching bifurcation where the largest vortex splits into two vortices. In the last three steps, two vortices disappear as a result of two punching bifurcations and the vortex at the wall detaches via a wall-pinching bifurcation. The structure shown in figure 8(i) then persists for the rest of the simulated time span, implying that at this Reynolds number two long-lasting vortices emerge from the boundary layer. In the course of their formation, several transitional vortex structures appear and our theory is able give a complete description of the topological changes in the flow field as a series of bifurcations in the Q-contours.

To illustrate how the formation of the vortices depends on the Reynolds number we construct a bifurcation diagram of the eruption process (see figure 9). The black squares in the diagram mark the times at which the various bifurcations are observed in the simulations. The thick translucent lines trace out the temporal evolution at fixed

Reynolds numbers. Line I corresponds to the case just discussed (Re = 2063), with the circular symbols indicating the times at which the snapshots in figure 8 were taken. We have connected bifurcation points of the same type by solid lines to indicate that we expect a similar evolution in between the simulations presented in the diagram.

However, the U-shaped curve tracing out the punching bifurcation is an exception. The bifurcation points on this curve do not satisfy the same non-degeneracy conditions. The squares on the left branch of the curve mark a forward punching bifurcation where $\partial_t Q_0 > 0$ and the squares on the right branch mark a backward punching bifurcation where $\partial_t Q_0 < 0$. This change of sign of $\partial_t Q$ indicates the existence of a codimension-two point (t_0, Re_0) where $\partial_t Q_0 = 0$. According to (4.2) the bifurcation curve close to such a point is approximately parabolic. Making a least-square fit to a parabola of the four nearest data points yields the expression

$$\mathrm{Re} = 1817 + 0.0458(t - 312)^2, \tag{5.2}$$

from which we get the estimate of the codimension-two point $(t_0, \mathrm{Re}_0) = (312, 1817)$.

It is important to notice that we have estimated the codimension-two point without actually solving the equations (4.1) that characterize it. The simulation results are interpreted within the framework of the bifurcation theory we have developed, and are consistent with the codimension-two case we have analysed.

In summary, over the range of Reynolds numbers considered in the bifurcation diagram, the final outcome of the evolution is the same: Two vortices emerge from the erupting boundary layer and the time at which the various bifurcations occur only changes very little with Re. The only exception is the co-dimension two phenomenon at Re = 1817 (Line II in figure 9) that separates the parameter space into two regions with distinct evolution of the topology of the vortices. For Re > 1817, exemplified by Line I in figure 9, a small vortex appears and disappears again close to the wall. As Re is decreased, its lifetime diminishes and for Re < 1817, exemplified by Line III, the vortex does not appear at all.

6. Discussion

Using the Q-criterion we have formulated a theory describing the evolution of vortices in two-dimensional incompressible flow. The theory is complete in the sense that it identifies all possible codimension-one bifurcations of the $Q = 0$ contour curves. Our theory provides a systematic approach to describing topological changes associated with the creation/destruction and the merging/splitting of vortices. The possible types of bifurcations serve as templates that facilitate the construction of a bifurcation diagram. Despite the fact that the mathematical analysis is technical the results are easy to apply: A vortex bifurcation event occurs when $Q = \partial_x Q = \partial_y Q = 0$ and the type of event depends only on higher order derivatives of Q. At a no-slip wall $y = 0$ the corresponding conditions are $\widetilde{Q} = \partial_x \widetilde{Q} = 0$, where $\widetilde{Q} = Q/y^2$. The degeneracy and non-degeneracy conditions required to locate and identify each type of bifurcation can therefore be computed directly from derivatives of the velocity field.

Numerical simulations of boundary layer eruption at moderate Reynolds numbers showed that all four types of codimension-one bifurcations occur in that flow. We also observed the occurrence of a codimension-two bifurcation at Re = 1817. It arises via the coalescence of two codimension-one bifurcations that are associated with the creation/destruction of a particular vortex. This vortex does not develop for smaller Reynolds numbers but has an increasing lifespan as the Reynolds number increases above 1817. We were able to infer the existence of the codimension-two point and showed how

to determine its location using only knowledge about the $Q = 0$ contour, i.e. without requiring derivatives of Q. This may be the most important message of the present paper: Bifurcation theory provides a list of possible vortex bifurcation events. Observations of changes in the topology of the $Q = 0$ contour in specific computational or experimental data can be matched with a bifurcation event which is mathematically well understood, leading to an interpretation of the data which rests on a solid theoretical basis.

If the Reynolds number is increased beyond the range considered in our case study, additional codimension-two points are likely to arise. If that is the case it would be useful to give a complete analysis of all codimension-two cases, as outlined in § 4. Another important extension would be to generalize the theory to three-dimensional flows. In this case the zero contours of Q are surfaces in three dimensions. Much of our analysis will carry over, using the three-dimensional version of the Morse Lemma. In particular, a vortex bifurcation event will occur when $Q = \partial_x Q = \partial_y Q = \partial_z Q = 0$.

Finally, we note that the bifurcations in the topology of the $Q = 0$ curves are much simpler than those found by Balci *et al.* (2015) in the topology of the instantaneous streamlines. When studying the boundary layer eruption process using the latter approach, a bifurcation diagram of codimension three was needed to describe the eruption process completely. We therefore believe that the concepts proposed in the present paper will be helpful for interpreting and classifying vortex interactions in a large range of flows obtained either numerically or experimentally.

Appendix A. Analysis of a particular codimension-two bifurcation

In this appendix we analyse the codimension-two bifurcation that arises when a forward and a reverse punching bifurcation coalesce at a particular value of the Reynolds number, leading to the violation of the non-degeneracy condition $\partial_t Q_0 \neq 0$.

To identify the time and Reynolds number at which this scenario arises we introduce a second parameter, r, representing the deviation of the Reynolds number from the value at which the codimension-two bifurcation occurs. We then choose a coordinate system such that a bifurcation point is located at $(x, y, t, r) = (0, 0, 0, 0)$ and, as before, we use subscript 0 to denote evaluation at the bifurcation point. We consider a bifurcation point that is characterized by the following set of degeneracy conditions

$$Q_0 = 0, \;\; \partial_x Q_0 = 0, \;\; \partial_y Q_0 = 0, \;\; \partial_t Q_0 = 0. \tag{A 1}$$

The first three of these are simply the conditions (2.3) required for the occurrence of a punching bifurcation. The final condition ensures that the first of the two non-degeneracy conditions, equation (2.5), is violated.

We now augment these conditions by the following non-degeneracy conditions

$$\partial_r Q_0 > 0, \;\; \partial_{tt} Q_0 < 0 \tag{A 2}$$

and

$$H_0^Q = \begin{pmatrix} \partial_{xx} Q_0 & \partial_{xy} Q_0 & \partial_{xt} Q_0 \\ \partial_{xy} Q_0 & \partial_{yy} Q_0 & \partial_{yt} Q_0 \\ \partial_{xt} Q_0 & \partial_{yt} Q_0 & \partial_{tt} Q_0 \end{pmatrix} \text{ is negative definite.} \tag{A 3}$$

Using these conditions we will now show that there is a bifurcation curve $r(t) = Ct^2 + \mathcal{O}(t^3)$, where C is a positive constant, which separates the (t, r) parameter space into two regions, one where a vortex is present and one where there is none. Thus, for a small fixed $r > 0$, a vortex is created in a punching bifurcation at $t \approx -\sqrt{r/C}$. The

vortex disappears again in a reverse punching bifurcation at $t \approx \sqrt{r/C}$ – exactly as seen in figure 9.

We start by observing that, since $Q_0 = 0$ and $\partial_r Q_0 \neq 0$, it follows from the Implicit Function Theorem that there exist a unique local function $R(x, y, t) = r$ satisfying that $R_0 = 0$ and $Q(x, y, t, R(x, y, t)) = 0$. By implicit differentiation of Q, we obtain that

$$\partial_x R_0 = -\frac{\partial_x Q_0}{\partial_r Q_0} = 0, \quad \partial_y R_0 = -\frac{\partial_y Q_0}{\partial_r Q_0} = 0, \quad \partial_t R_0 = -\frac{\partial_t Q_0}{\partial_r Q_0} = 0, \tag{A 4}$$

and the Hessian

$$H_0^R = \begin{pmatrix} \partial_{xx} R_0 & \partial_{xy} R_0 & \partial_{xt} R_0 \\ \partial_{xy} R_0 & \partial_{yy} R_0 & \partial_{yt} R_0 \\ \partial_{xt} R_0 & \partial_{yt} R_0 & \partial_{tt} R_0 \end{pmatrix} = -\frac{1}{\partial_r Q_0} H_0^Q. \tag{A 5}$$

Since $\partial_r Q_0 > 0$ and H_0^Q is negative definite, it follows from (A 5) that H_0^R is positive definite. Hence, it follows by Sylvester's criterion that the upper left 2×2 corner of H_0^R is also positive definite. The conditions in (A 4) and (A 5), therefore, allow us to apply the Implicit Function Theorem, this time on the gradient of R. Hence, we conclude that there exist unique local functions $X(t) = x$, $Y(t) = y$ satisfying that $X_0 = 0$, $Y_0 = 0$ and

$$\begin{pmatrix} \partial_x R(X(t), Y(t), t) \\ \partial_y R(X(t), Y(t), t) \end{pmatrix} = \mathbf{0}. \tag{A 6}$$

The generalized version of the Morse Lemma depending on parameters (Hörmander 2007) implies that in a neighbourhood of the critical point $(x, y) = (0, 0)$ there exist a, possibly nonlinear, coordinate change, $\hat{x} = \hat{x}(x, y)$, $\hat{y} = \hat{y}(x, y)$, such that

$$\hat{x}(0, 0) = 0, \quad \hat{y}(0, 0) = 0, \tag{A 7}$$

and

$$R(\hat{x}, \hat{y}, t) = R(X(t), Y(t), t) + \hat{x}^2 + \hat{y}^2. \tag{A 8}$$

In the new coordinate system the zero contour curve of Q is therefore given by the equation,

$$\hat{x}^2 + \hat{y}^2 = r - R(X(t), Y(t), t). \tag{A 9}$$

The right-hand side of (A 9) determines whether or not there exist any points, sufficiently close to $(\hat{x}, \hat{y}) = (0, 0)$, which are part of the zero contour curve of Q. The curve $r(t) = R(X(t), Y(t), t)$, therefore separates the parameter space in two regions one where a vortex region is present, and one where it is not. We find

$$\begin{aligned} r'(t) &= \nabla R(X(t), X(t), t) \cdot \mathbf{x}'(t), \\ r''(t) &= \mathbf{x}'(t)^T \cdot H^R(X(t), Y(t), t) \cdot \mathbf{x}'(t) + \nabla R(X(t), Y(t), t) \cdot \mathbf{x}''(t), \end{aligned}$$

where

$$\mathbf{x}(t) = \begin{pmatrix} X(t) \\ Y(t) \\ t \end{pmatrix}. \tag{A 10}$$

By (A 4) and (A 5) it follows that $\nabla R_0 = \mathbf{0}$ and H_0^R is positive definite. Since $\mathbf{x}'(t)$ is non-zero for all t it follows that

$$\begin{aligned} r'(0) &= 0, \\ r''(0) &= \mathbf{x}'(0)^T \cdot H_0^R \cdot \mathbf{x}'(0) > 0. \end{aligned}$$

By Taylor expansion of r at $t = 0$ we get the desired result

$$r(t) = Ct^2 + \mathcal{O}(t^3), \tag{A 11}$$

where $C = \frac{1}{2}\mathbf{x}'(0)^T \cdot H_0^R \cdot \mathbf{x}'(0) > 0$.

We have proved that in a neighbourhood of a codimension-two point the curve $r(t) = Ct^2 + \mathcal{O}(t^3)$ is a bifurcation curve. The non-degeneracy condition $\partial_{tt}Q_0 < 0$ and the continuity of $\partial_t Q$ implies that $\partial_t Q$ is positive on the left branch of the curve and negative on the right branch. The only point on the curve satisfying the conditions in (A 1) is therefore the bifurcation point at $(x, y, t, r) = (0, 0, 0, 0)$ and all other points on the curve must be bifurcation points with codimension one.

By Sylvester's criterion the upper left 2×2 corner of H_0^Q is negative definite when H_0^Q is negative definite. By continuity, it therefore follows for all other points on the bifurcation curve that

$$Q = 0, \;\; \partial_x Q = 0, \;\; \partial_y Q = 0, \;\; \partial_t Q \neq 0, \tag{A 12}$$

and

$$\begin{pmatrix} \partial_{xx}Q & \partial_{xy}Q \\ \partial_{xy}Q & \partial_{yy}Q \end{pmatrix} \text{ is negative definite.} \tag{A 13}$$

These conditions are identical to the conditions in §2, implying that a punching bifurcation occurs forward on the left-hand side of the bifurcation curve, where $\partial_t Q$ is positive. In contrast $\partial_t Q$ is negative on the right-hand side of the curve and here a punching bifurcation occurs backward at any point. This is completely consistent with the behaviour observed in figure 9.

REFERENCES

Andersen, M. 2013 Topology of streamlines and vorticity contours for two - dimensional flows. PhD thesis, Technical University of Denmark.

Balci, A., Andersen, M., Thompson, M. C. & Brøns, M. 2015 Codimension three bifurcation of streamline patterns close to a no-slip wall: A topological description of boundary layer eruption. *Physics of Fluids* **27** (5), 53603.

Brøns, M. 2007 Streamline topology: Patterns in fluid flows and their bifurcations. *Advances in Applied Mechanics* **41**, 1–42.

Brøns, M. & Bisgaard, A. 2006 Bifurcation of vortex breakdown patterns in a circular cylinder with two rotating covers. *Journal of Fluid Mechanics* **568**, 329–349.

Chakraborty, P., Balachandar, S. & Adrian, R. J. 2005 On the relationships between local vortex identification schemes. *Journal of Fluid Mechanics* **535**, 189–214.

Chen, Q., Zhong, Q., Qi, M. & Wang, X. 2015 Comparison of vortex identification criteria for planar velocity fields in wall turbulence. *Physics of Fluids* **27** (8), 085101.

Doligalski, T. L. & Walker, J. D. A. 1984 The boundary layer induced by a convected two-dimensional vortex. *Journal of Fluid Mechanics* **139**, 1–28.

Elsas, J. H. & Moriconi, L. 2017 Vortex identification from local properties of the vorticity field. *Physics of Fluids* **29** (1), 015101.

Haller, G., Hadjighasem, A., Farazmand, M. & Huhn, F. 2016 Defining coherent vortices objectively from the vorticity. *Journal of Fluid Mechanics* **795**, 136–173.

Heil, M. & Hazel, A. L. 2006 oomph-lib - an object-oriented multi-physics finite-element library. *Lecture Notes in Computational Science and Engineering* **53**, 19–49.

Heil, M., Rosso, J., Hazel, A. L. & Brøns, M. 2017 Topological fluid mechanics of the formation of the Kármán-vortex street. *Journal of Fluid Mechanics* **812**, 199–221.

Hunt, J. C. R, Wray, A. A. & Moin, P. 1988 Eddies, streams, and convergence zones

in turbulent flows. Tech. Rep. CTR-S88. Center for Turbulence Research, Stanford University.

Hörmander, L. 2007 *The Analysis of Linear Partial Differential Operators III*. Springer Berlin Heidelberg.

Jeong, J & Hussain, F 1995 On the identification of a vortex. *Journal of Fluid Mechanics* **285**, 69–94.

Kudela, H. & Malecha, Z. M. 2009 Eruption of a boundary layer induced by a 2d vortex patch. *Fluid Dynamics Research* **41** (5), 055502.

Obabko, A. V. & Cassel, K. W. 2002 Navier-Stokes solutions of unsteady separation induced by a vortex. *Journal of Fluid Mechanics* **465**, 99–130.

Robinson, S.K. 1991 Coherent motions in the turbulent boundary-layer. *Annual Review of Fluid Mechanics* **23** (1), 601–639.

Wiggins, S. 2003 *Introduction to Applied Nonlinear Dynamical Systems and Chaos*. Springer New York.

Williams, J. C. 1977 Incompressible boundary-layer separation. *Annual Review of Fluid Mechanics* **9** (1), 113–144.

Zhang, Y., Liu, K., Xian, H. & Du, X. 2018 A review of methods for vortex identification in hydroturbines. *Renewable and Sustainable Energy Reviews* **81**, 1269–1285.

Zhong, Q., Chen, Q., Chen, H. & Li, D. 2017 A topological method for vortex identification in turbulent flows. *Fluid Dynamics Research* **49** (1), 015509.

Zhou, J., Adrian, R. J., Balachandar, S. & Kendall, T. M. 1999 Mechanisms for generating coherent packets of hairpin vortices in channel flow. *Journal of Fluid Mechanics* **387**, 353–396.

3.3 Epilogue

In the presented paper, we made a comprehensive description of the early stages in the eruption process based on the Q-criterion. Further to this, it is natural to ask what the description would look like for another choice of vortex criterion? The original work presented in this thesis is based on two different criteria, the first and second paper are based solely on the Q-criterion while the results in third paper are based on the vorticity extremum criterion. We notice that Q can be expressed as

$$\begin{aligned} Q &= \partial_x u \partial_y v - \partial_y u \partial_x v \\ &= \partial_x u \partial_y v - \partial_y u(\omega + \partial_y u), \end{aligned} \tag{3.5}$$

indicating that there is no simple connection between the vortices defined as vorticity extrema and vortices defined by the Q-criterion. A comparison of the two criteria is possible by applying both of them to the same problem. In a fourth paper, which is not made as a part of the Ph.D work we study boundary layer eruption with vortices defined as vorticity extrema [13]. Since the results in the two papers on boundary layer eruption are based on the same simulations with different post-processing, we can here make a direct comparison of the two criteria. In figure 3.1 and figure 3.2 we present two sequence of snapshots from simulations with $\mathrm{Re} = 750$ and $\mathrm{Re} = 2063$, respectively. In each snapshot, the vortex structure is marked based on both criteria. The regions with positive Q-value are encircled by white lines which correspond to the zero contour curves of Q and the local extrema of vorticity are marked with white squares. In the time span between the subfigures in each of the two examples, a topological bifurcation occur in either the vorticity field or the $Q = 0$ level curves. In figure 3.1(a) and figure 3.2(a) there is a single local extremum of vorticity inside a region with positive Q-value, corresponding to the initial vortex. The final vortex structure within our time span from $t = 0$ to $t = 747$ is shown in figure 3.1(i) and figure 3.2(n), respectively. In both examples the two vortex criteria agree; the initial vortex is preserved and two secondary vortices are formed from the erupting boundary layer. It is, however, clear that the two criteria do not agree on the temporary vortices leading to the final stage.

In order to give a complete comparison based on the two studies we compare the two final bifurcation diagrams which are presented in [47] and [13], respectively. The two bifurcation diagrams are lined up next to each other in figure 3.3. They show that in general there is no simple connection between our two choices of vortex criteria. We see that the size and the shape of the different regions in the diagrams are highly dependent on the criterion. There are, however, some similarities. In both cases we observe a more complex vortex structure for higher

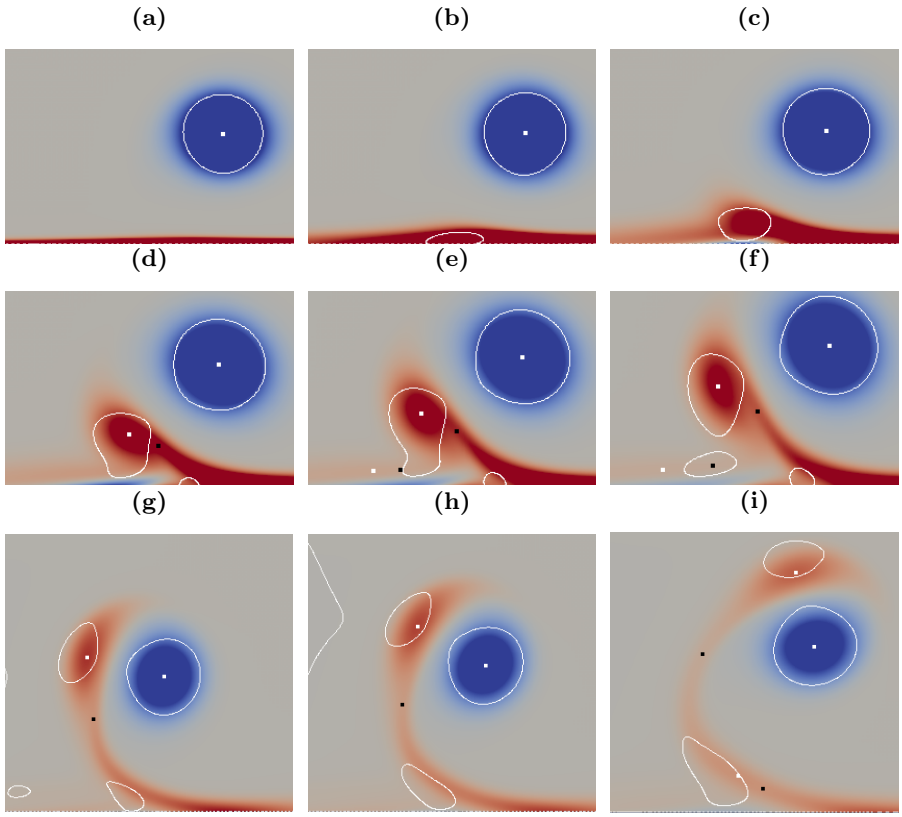

Figure 3.1: Numerical results for Re = 750 at the following time steps (a) $t = 11$ (b) $t = 48$ (c) $t = 117$ (d) $t = 203$ (e) $t = 245$ (f) $t = 293$ (g) $t = 453$ (h) $t = 507$ (i) $t = 640$. Each figure shows a zoom in on a region close to the initial vortex. The vorticity contours with values from -0.3 to 0.3 are colored in blue and red. The regions with positive Q value are encricled by white lines which corresponds to the zero contour curves of Q. The white squares correspond to local extrema of vorticity while the black squares show the location of saddle points.

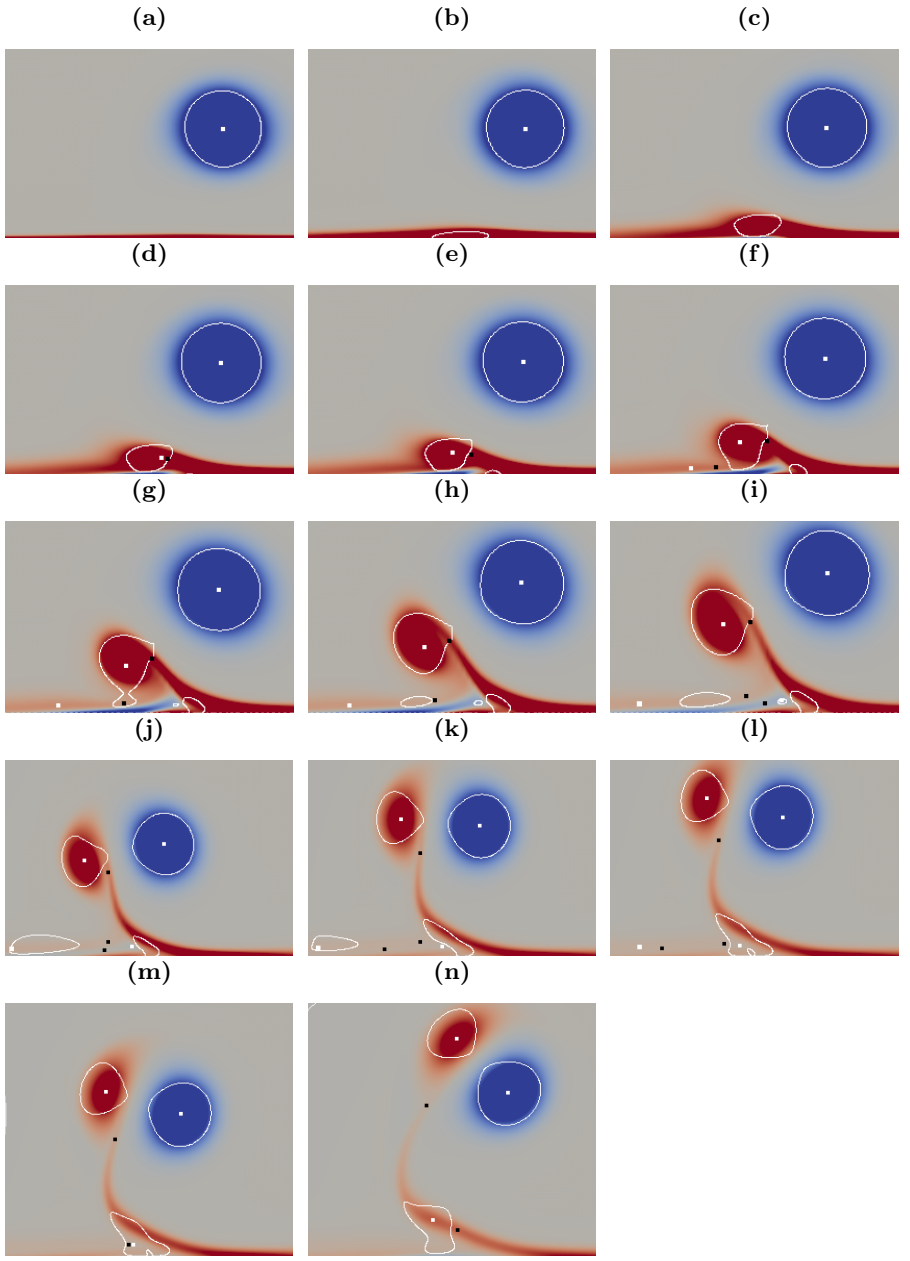

Figure 3.2: Numerical results for Re = 2063 at the following time steps (a) $t = 11$ (b) $t = 48$ (c) $t = 117$ (d) $t = 139$ (e) $t = 160$ (f) $t = 203$ (g) $t = 256$ (h) $t = 293$ (i) $t = 331$ (j) $t = 395$ (k) $t = 464$ (l) $t = 496$ (m) $t = 507$ (n) $t = 597$. The vorticity contours with values from -0.3 to 0.3 are colored in blue and red. Regions with positive Q value are encricled by white lines which corresponds to the zero contour curves of Q.

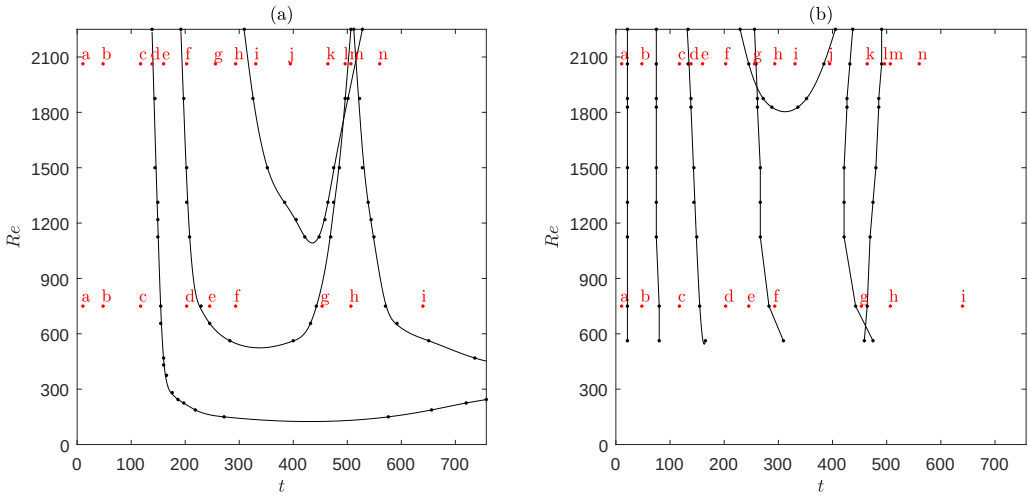

Figure 3.3: Bifurcation diagrams of the eruption process. The small black dots represent our actual observations of bifurcations in the numerical results. (a) is based on the vorticity extremum criterion and (b) is based on the Q criterion. The red dots marked with a letter correspond to the examples shown in figure 3.1 and figure 3.2

Re, and for some of the observed bifurcations the time where the bifurcation occurs tends to be independent of Re for higher values of Re. Our observations lead us to the conclusion that the analysis of vortex formation may be highly dependent on the chosen definition of a vortex. We do, however, see that the final vortex structure within our time span is the same for both criteria. This indicates that the two criteria agree on the long-lasting vortex structures that seem more robust, but they do not agree on the temporary structures leading to the final stage. To understand how we end up at the same final vortex structure it is important to be able to analyse the bifurcations that occur on the way.

Chapter 4

Topological bifurcations of vortex pair interactions

4.1 Introduction

The bifurcation theory formulated in Paper I describes all possible codimension one bifurcations of the $Q = 0$ level curves. Furthermore, it includes an analysis of the codimension two phenomenon that occur when the non-degeneracy condition $\partial_t Q \neq 0$ is violated at a critical point. The paper presented in the following section is a direct continuation of the theoretical results presented in Paper I. In the following paper, we analyse the codimension two phenomenon that occur when the non-degeneracy condition on the Hessian is violated. This means that we analyse the structural changes that occur at a degenerate critical point where H^Q is singular with zero as a simple eigenvalue. Since a degenerate critical point of Q is the starting point for the bifurcation analysis, the approach is quite similar to the analysis of the cusp bifurcation of the stream function ψ which was presented in the introductory section. The degeneracy conditions in (2.26) and (2.28) also apply to Q but we restrict our analysis to bifurcations on the $Q = 0$ level curves. The requirement that $Q = 0$ acts as an additional degeneracy condition which means that the bifurcation phenomenon has codimension two. The result of the analysis is another cusp singularity that appears on the bifurcation curve instead of the level curve. We prove that the two branches meeting at the cusp singularity are respectively a pinching bifurcation curve and a punching bifurcation curve and therefore the codimension two point can be considered as a threshold for vortex merging. In the light of

this theoretical result, we found it natural to apply our bifurcation theory to study vortex pair interactions and in particular vortex merging.

Studying vortex pair interactions leads to an understanding of the basic dynamics in other fluid dynamical problems. The problem is very essential and therefore very well studied (see among others [41, 20, 53, 8]). Most previous studies have focused on inviscid interactions of vortex patches but some also consider vortex merging in a viscous setting. We believe, however, that our approach can contribute with new insights by giving an accurate mathematical description of the problem in a viscous setting. We consider the problem in a two-dimensional setting at low values of Reynolds numbers, i.e. we perform Navier-Stokes simulations with $Re = 10$ and $Re = 100$. The flow is defined with two point vortices as initial condition and we consider their strength ratio $\alpha = \Gamma_1/\Gamma_2$ as one out of two the bifurcation parameters in the problem. The second bifurcation parameter is a non-dimensional time variable σ. For both values of the Reynolds number we observe a threshold for merging that corresponds to the analysed codimension two phenomenon.

In this paper, we do not limit ourselves to analyse numerical simulation of vortex pair interactions. Clearly, the problem we are considering does not have an explicit analytical solution, so in addition we examine the synthetic flow predicted by the core growth model [31, 32, 34, 1]. The core growth model assumes that the vorticity of two initial point vortices diffuses symmetrically as two isolated Lamb-Oseen vortices and the centers of the vortices move in the velocity field induced by the other vortex. From this description we achieve a closed analytical expression for Q depending only on α and σ. Even though the core growth model is not an exact solution to the Navier-Stokes equations we argue that a given accuracy can be achieved for sufficiently small values of Reynolds numbers. In addition to the theoretical contribution, a secondary goal for the paper is to discuss for which values of Reynolds number it is reasonable to use the core growth model instead of numerically solving the Navier-Stokes equation.

By applying the core growth model we introduce a built-in symmetry in the formulation of the problem. The core growth model has the x-axis as a line of symmetry, i.e. $Q(x, y) = Q(x, -y)$. We prove that this line of symmetry lead to a special type of codimension two bifurcation which will not occur in Navier-Stokes simulations where the symmetry is not expected.

The main result of the paper is a complete topological analysis of merging of Q-vortices in the core growth model compared with Navier-Stokes simulations at $Re = 10$ and $Re = 100$. Our overall analysis shows that the merging process can be divided into three different regimes depending on the strength ratio of the vortices. For sufficiently high strength ratio, the weakest vortex is suppressed

by the strong vortex, and no merging as such occurs. For lower strength ratios, there are two different bifurcation sequences leading to merging.

By combining the theoretical results from Paper I and Paper II we have developed an extensive bifurcation theory for Q-vortices. The theory describes all the bifurcations with codimension one or two that may occur away from boundaries. Furthermore, it includes an analysis of the codimension one bifurcations which may occur at no-slip walls and a special type of codimension two bifurcation which only occur in models with a line of symmetry.

Numerical simulations of any fluid dynamical problem can only give us information that is discretised with respect to the parameters in the problem. The possible types of bifurcations serve as a template that facilitates the construction of a bifurcation diagram from the numerical results. We believe that the overall theory and our general approach can be useful for interpreting and classifying a wide range of fluid dynamical problems in two dimensions. Depending on the complexity of the problem, it may be necessary to expand the theory further with bifurcations of higher codimension.

The bifurcation theory for Q-vortices is general in the sense that can immediately be applied to other vortex criteria of the same type. By a vortex criterion of the 'same type', we mean that a vortex is defined as a region encircled by a contour curve of some scalar valued function. This could be, that a vortex is defined as a region with vorticity greater than or pressure lower than some threshold value.

4.2 Paper II

The paper in this section is a reprint of the version that has been accepted for publication in Journal of Fluid Mechanics. The original publication can be found here:

Nielsen, A. R., Andersen, M., Hansen, J. S.& Brøns, M. (2021). Topological bifurcations of vortex pair interactions. Journal of Fluid Mechanics, 917. https://doi.org/10.1017/jfm.2021.191 [46]

The paper is only based on results that are original work done during the Ph.D period.

Topological bifurcations of vortex pair interactions

Anne R. Nielsen[1], Morten Andersen [2], Jesper S. Hansen[2] and Morten Brøns[1]

[1]Department of Applied Mathematics and Computer Science, Technical University of Denmark, 2800 Lyngby, Denmark

[3]Department of Science and Environment, Roskilde University, 4000 Roskilde, Denmark

Abstract

We investigate vortex pair interactions at low Reynolds numbers. Our analysis is based on the two-dimensional Q-criterion and we make use of a topological approach to describe the qualitative changes of the vortex structure. In order to give a complete description of vortex pair interactions we further develop a general bifurcation theory for Q-vortices and prove that a threshold for vortex merging may occur when we allow two parameters to vary. To limit the number of free parameters, we study the interactions with two point vortices as the initial condition and show that the threshold is a codimension two bifurcation that appears as a cusp singularity on a bifurcation curve. We apply the general theory to the analytically tractable core growth model and conclude that a pair of co-rotating vortices merge only if their strength ratio, $\alpha = \Gamma_1/\Gamma_2$ is less than 4.58. Below this threshold value, we observe two different regimes in which the merging processes can be described with different sequences of bifurcations. By comparison with Navier-Stokes simulations at different Reynolds numbers, we conclude that the merging threshold varies only slightly for Reynolds numbers up to 100. Furthermore, we observe an excellent agreement between the core growth model and the numerical simulations for Reynolds numbers below 10. We therefore conclude that, instead of solving the Navier-Stokes equation numerically we can, for sufficiently small Reynolds numbers, apply the core growth model as a simple, analytically tractable model with a low dimension.

1. Introduction

Studying the fundamental interactions of vortices helps us understand the behaviour of complicated flows which can be encountered in nature. A simple example of an interaction is two-dimensional vortex merging, which is a well-studied phenomenon in fluid mechanics. For a general review of dynamics and instabilities of vortex pairs, see e.g. Leweke *et al.* (2016). It is sometimes possible to observe vortex merging visually in experiments and numerical simulations, but it can be difficult to give an accurate mathematical description of the merging process. Early studies of vortex merging mainly focus on merging in inviscid fluids where vortices are defined as vortex patches with constant vorticity (Overman & Zabusky 1982; Dritschel 1985). The jump of vorticity across vortex boundaries is advected by the velocity field and the problem effectively becomes one-dimensional. This approach, known as contour dynamics, was originally proposed by Deem & Zabusky (1978). The conservation of vorticity ensures that the fluid will be divided into regions of uniform vorticity for all time and, in principle, merging is never possible. Dritschel (1986) overcomes this issue by applying contour surgery, which

is an algorithm allowing two contours enclosing the same uniform vorticity to merge into one if they are close enough together. In this study, we will address the problem rigorously in a viscous setting. We identify vortices by the widely used Q-criterion (Hunt *et al.* 1988). In general, a positive Q-value implies that the local rotation dominates the strain. In two dimensions, Q simplifies to the determinant of the velocity gradient tensor $\nabla \mathbf{u}$ and a vortex is therefore defined as a region where

$$Q(x, y) = \det(\nabla \mathbf{u}(x, y)) > 0. \tag{1.1}$$

In this paper, we present a complete topological analysis of merging of Q-vortices in the core growth model. The main result of our analysis is that the merging process can be divided into three different regimes depending on the strength ratio of the vortices. For sufficently high strength ratio, the weakest vortex is supressed by the strong vortex, and no merging as such occurs. For lower strength ratios, there are two different bifurcation sequences leading to merging. The core growth model has previously been used to study vortex merging by Jing *et al.* (2012) and Andersen *et al.* (2019). In the following section we review the model and show that it allows us to write an analytical expression for Q depending on two parameters, the strength ratio of the two vortices and the time.

We monitor the vortex interactions by looking for bifurcations of the curves bounding the vortices, the level curves $Q(x, y) = 0$. Bifurcations occur when singular points appear on these curves. An analysis of all possible perturbations of a given degenerate pattern tells us what we might expect when a given number of parameters are allowed to vary. When only a single parameter is varied, the bifurcations that occur in a robust way are referred to as having codimension one. We have already formulated a complete codimension one theory in earlier studies, see Nielsen *et al.* (2019) or the brief summary in § 3. Our previous study includes an analysis of a single codimension two phenomenon, but as the core growth model has two free parameters, it is necessary to extend the existing theory with an analysis of another codimension two bifurcation. This further development of the theory can be found in § 3.1. The core growth model has a built-in symmetry that may lead to a special type of codimension two bifurcation; this case is analysed in § 3.2. We compare the results for the core growth model with Navier-Stokes simulations in § 4.1, and find good agreement for low values of the Reynolds number. An analysis of the topological structure of vortex pairs is inextricably linked to the way we choose to define vortices mathematically. There are many definitions of vortices available in the literature, see Zhang *et al.* (2018) for a review. To our knowledge, this is the first study to analyse vortex pair interactions based on the topology of the Q-criterion. Andersen *et al.* (2019) have previously studied vortex merging from a topological point of view with vortices defined as local extrema of vorticity. This method identifies a vortex by a feature point that does not provide any information about the shape or size of the vortex. Applying the Q-criterion might therefore provide some opportunities for a more elaborate analysis. In § 5 we comment on the importance of the vortex criterion.

2. The core growth model

We consider an incompressible fluid in an unbounded two dimensional domain governed by the Navier-Stokes equations. In terms of the vorticity, the Navier-Stokes equations can be written as the vorticity transport equation,

$$\frac{\partial \omega}{\partial t} = -\mathbf{u} \cdot \nabla \omega + \nu \Delta \omega, \tag{2.1}$$

where ν is the kinematic viscosity and $\mathbf{u}$ is the fluid velocity. One of the very few known analytic solutions to (2.1) is the Lamb-Oseen vortex (Saffman 1992),

$$\omega(r,\theta,t) = \frac{\Gamma}{\pi\sigma(t)^2} e^{-r^2/\sigma(t)^2}, \quad u_\theta(r,\theta,t) = \frac{\Gamma}{2\pi r}\left(1 - e^{-r^2/\sigma(t)^2}\right), \quad u_r(r,\theta,t) = 0, \tag{2.2}$$

with

$$\sigma(t) = \sqrt{4\nu t}. \tag{2.3}$$

The Lamb-Oseen vortex is the solution corresponding to a single point vortex with strength Γ as initial condition. The vorticity field ω is initially concentrated at the origin and diffuses as a Gaussian distribution. For multiple point vortices as initial condition an analytic solution is not available and one would generally refer to numerical simulations of the vorticity transport equation. Instead we investigate the synthetic flow predicted by the core growth model, also known as the multi Gaussian model (Jing *et al.* 2010; Kim & Sohn 2012; Andersen *et al.* 2019). The model assumes that the vorticity of each initial point vortex diffuses symmetrically as an isolated Lamb-Oseen vortex and the centers of the Gaussian vortices move in the velocity field induced by the other diffusing vortices. For two Gaussian vortices, initially centered at $(-d, 0)$ and $(d, 0)$, one can deduce (Kim & Sohn 2012) that the distance between the centers of the two Gaussian vortices is conserved and the vortices rotate around the a stationary center of vorticity

$$(x_{cv}, y_{cv}) = \left(\frac{d(\Gamma_2 - \Gamma_1)}{\Gamma_1 + \Gamma_2}, 0\right), \tag{2.4}$$

with the same time-dependent angular velocity

$$\frac{d\phi(t)}{dt} = \frac{\Gamma_1 + \Gamma_2}{2\pi(2d)^2}\left(1 - e^{-(2d)^2/\sigma^2}\right). \tag{2.5}$$

We notice that the angular velocity tends to zero as ν or t increases. By integrating $\frac{d\phi(t)}{dt}$ in time we obtain the direction angle as a function of time

$$\phi(t) = \frac{\Gamma_1 + \Gamma_2}{2\pi(2d)^2\nu}\left(\frac{\sigma^2}{4} - \frac{\sigma^2}{4}e^{-(2d)^2/\sigma^2} + d^2\int_{(2d)^2/\sigma^2}^{\infty}\frac{e^{-s}}{s}ds\right). \tag{2.6}$$

We notice that the angular velocity and the direction angle depend on the total of vortex strength $\Gamma_1 + \Gamma_2$ and the distance between the vortices, not on the strength ratio. The positions of the two Gaussian vortex centers $(x_1(t), y_1(t))$, $(x_2(t), y_2(t))$ are given by (2.6), i.e.

$$\begin{pmatrix} x_1(t) \\ y_1(t) \end{pmatrix} = (d - x_{cv})\begin{pmatrix} \cos\phi(t) \\ \sin\phi(t) \end{pmatrix} + \begin{pmatrix} x_{cv} \\ 0 \end{pmatrix}, \tag{2.7}$$

$$\begin{pmatrix} x_2(t) \\ y_2(t) \end{pmatrix} = -(d + x_{cv})\begin{pmatrix} \cos\phi(t) \\ \sin\phi(t) \end{pmatrix} + \begin{pmatrix} x_{cv} \\ 0 \end{pmatrix}. \tag{2.8}$$

Since the core growth model evolves as a superposition of two Lamb-Oseen vortices, the vorticity field is given as

$$\omega(x,y,t) = \frac{\Gamma_1}{\pi\sigma^2}e^{-d_1^2/\sigma^2} + \frac{\Gamma_2}{\pi\sigma^2}e^{-d_2^2/\sigma^2}, \tag{2.9}$$

where

$$d_1^2 = (x - x_1(t))^2 + (y - y_1(t))^2, \tag{2.10}$$

$$d_2^2 = (x - x_2(t))^2 + (y - y_2(t))^2. \tag{2.11}$$

By solving the Poisson equation $\omega = -\Delta\psi$ we obtain the following streamfunction in the core growth model

$$\psi(x, y, t) = -\frac{\Gamma_1}{4\pi}\left(\ln\left(d_1^2\right) + \int_{d_1^2/\sigma^2}^{\infty} \frac{e^{-s}}{s} ds\right) - \frac{\Gamma_2}{4\pi}\left(\ln\left(d_2^2\right) + \int_{d_2^2/\sigma^2}^{\infty} \frac{e^{-s}}{s} ds\right). \tag{2.12}$$

The core growth model is not an exact solution to the vorticity transport equation in (2.1). However, by inserting the synthetic flow into the equation, we can evaluate the error we make when using the core growth model. From (2.7), (2.8), (2.9) and (2.12) all three terms in the vorticity transport equation can be expressed analytically and by evaluating the limit as $\nu \to \infty$ we obtain for a fixed t that

$$\partial_t \omega - \nu\Delta\omega + \mathbf{u} \cdot \nabla\omega = \frac{(\Gamma_1^2 - \Gamma_2^2) y d}{32\pi^2\nu^3 t^3} + \mathcal{O}\left(\frac{1}{\nu^4}\right) \text{ as } \nu \to \infty, \tag{2.13}$$

which implies that the core growth model will be accurate for the viscosity going to infinity, i.e. for the Reynolds number going to zero. This will be confirmed by numerical computations in § 4.3. The quality of the approximation will necessarily depend on the value of the fixed t. For a smaller t value, a lower Reynolds number is required to achieve the given accuracy. Part of the purpose of this study is to establish an upper limit of the Reynolds number under which it is reasonable to use the core growth model instead of numerically solving the Navier-Stokes equation. It is worth noting that Gallay (2011) proved that on a fixed time interval the solution to the vorticity transport equation, with point vortices as initial conditions, converges uniformly in time to a superposition of Lamb-Oseen vortices as $\nu \to 0$. Since the core growth model has point vortices as the initial condition, Gallay's result indicates that the model will be relatively accurate also in weakly viscous flow. The model has previously been studied for $Re >> 1$, see Jing *et al.* (2012) for an example.

For simplicity the core growth model will be studied in a co-rotating frame, such that the centers of the Gaussian vortices are fixed at the initial positions. For a given time t, the transformation from the co-rotating to the initial frame is determined by a rigid rotation with the angle $\phi(t)$ around the center of vorticity. This guarantees that the topology of the vorticity field, the stream function and hence also the Q-field is unchanged when studied in the co-rotating frame. To analyse the core growth model for all possible combinations of vortex strengths and displacements we introduce the following dimensionless variables (denoted with $\sim$), $\tilde{x} = x/d$, $\tilde{y} = y/d$, $\tilde{\omega} = \omega d^2/\Gamma_2$, $\tilde{\sigma} = \sigma/d$, $\tilde{\psi} = \psi d^2/\Gamma_2$ and $\tilde{\psi} = \psi/\Gamma_2$. For simplicity, we are dropping the tildes from now on. In the co-rotating coordinate system the dimensionless vorticity and streamfunction for the core growth model become

$$\omega(x, y, \alpha, \sigma) = \frac{\alpha}{\pi\sigma^2} e^{-\frac{(x+1)^2+y^2}{\sigma^2}} + \frac{1}{\pi\sigma^2} e^{-\frac{(x-1)^2+y^2}{\sigma^2}}, \tag{2.14}$$

and

$$\psi(x,y,\alpha,\sigma) = -\frac{\alpha}{4\pi}\left(\ln\left((x+1)^2+y^2\right) + \int_{\frac{(x+1)^2+y^2}{\sigma^2}}^{\infty} \frac{e^{-s}}{s} ds\right) \\ -\frac{1}{4\pi}\left(\ln\left((x-1)^2+y^2\right) + \int_{\frac{(x-1)^2+y^2}{\sigma^2}}^{\infty} \frac{e^{-s}}{s} ds\right), \tag{2.15}$$

where

$$\alpha = \frac{\Gamma_1}{\Gamma_2}, \quad \sigma^2 = \frac{4\nu t}{d^2} \tag{2.16}$$

are the strength ratio of the two vortices and a dimensionless time variable, respectively. As a result the Gaussian vortices are fixed at $(-1,0)$, $(1,0)$. As described in the introduction we will analyse the topological bifurcations of vortex pair interactions by applying the Q criterion. Using (2.15) a closed analytical expression for Q in the co-rotating frame can be directly computed from

$$Q(x,y,\alpha,\sigma) = \left(\frac{\partial^2\psi}{\partial x^2}\right)\left(\frac{\partial^2\psi}{\partial y^2}\right) - \left(\frac{\partial^2\psi}{\partial x \partial y}\right)^2. \tag{2.17}$$

In § 4.1 we will analyse the zero level curves of this function in detail. We notice that the model has a built-in symmetry. The x-axis is a line of symmetry in the stream function and hence

$$Q(x,-y,\alpha,\sigma) = Q(x,y,\alpha,\sigma) \tag{2.18}$$

for all values of x, y, α and σ. Furthermore, it follows from (2.15) that

$$Q(x,y,\alpha,\sigma) = \alpha Q(-x,y,\frac{1}{\alpha},\sigma), \tag{2.19}$$

which makes it sufficient to investigate the topological bifurcations of the zero level curves of Q for $|\alpha| \geqslant 1$.

3. Bifurcation theory for Q-vortices

A general characterization of zero level curves of Q may be applied to any flow situation, regardless of whether it arises from the core growth model or the Navier-Stokes equations. Nielsen *et al.* (2019) show that there are two types of robust one-parameter bifurcations of the level curves $Q = 0$, the authors denoted these as a *pinching* and a *punching* bifurcation, see figure 1. The bifurcations occur when

$$Q = 0, \quad \partial_x Q = 0, \quad \partial_y Q = 0, \tag{3.1}$$

under the non-degeneracy conditions

$$\partial_t Q \neq 0 \tag{3.2}$$

and

$$H^Q = \begin{pmatrix} \partial_{xx}Q & \partial_{xy}Q \\ \partial_{xy}Q & \partial_{yy}Q \end{pmatrix} \text{ is non-singular.} \tag{3.3}$$

Here, t denotes a free parameter. A pinching (punching) bifurcation occurs when H^Q is indefinite (definite), and the direction of the bifurcation depends on the sign of $\partial_t Q$. A pinching bifurcation is the splitting or merging of two vortices while a punching bifurcation is the creation or disappearance of a single vortex.

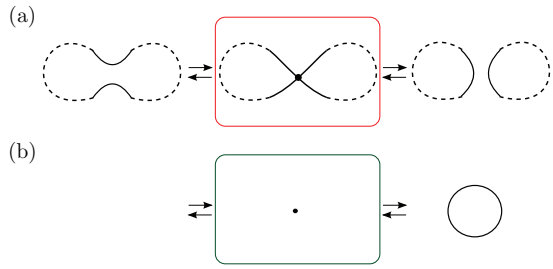

Figure 1: Illustration of the local changes in the structure of the $Q = 0$ contour curves during a (a) pinching and a (b) punching bifurcation. The bifurcation states are depicted in red and green boxes. The dashed lines in (a) show an example of a possible global structure during a pinching bifurcation. Note that the empty left panel in (b) illustrates that there are no $Q = 0$ contour curves.

In general there is no simple connection between the vorticity ω and the Q-value. If we consider an incompressible fluid at a point (x, y) with $\omega = 0$, we notice, however, that

$$Q = \partial_x u \partial_y v - \partial_y u \partial_x v = -(\partial_x u)^2 - (\partial_y u)^2.$$

Since $Q \leqslant 0$ we conclude that a point with zero vorticity will always be located outside or on the boundary of a Q-vortex. By continuity it is therefore impossible to have points with opposite signs of vorticity in the interior of a single vortex. Hence, two vortices can only merge in a pinching bifurcation if they have the same sign of vorticity in the interior.

3.1. *Theoretical description of codimension two bifurcation*

A flow may depend on several parameters, such as the Reynolds number or a parameter that determines the initial geometry. In this section, we consider a flow described as a smooth system depending on two parameters, t and r. In this setting, the two generic types of one-parameter bifurcations occur when crossing a one dimensional bifurcation curve in the (t, r) parameter space. A codimension two point on one of these bifurcation curves is a point where both parameters are required to take on particular values, so that one of the non-degeneracy conditions in (3.2) or (3.3) are violated. The codimension two bifurcation where $\partial_t Q = 0$ is analysed in detail in previous studies (Nielsen *et al.* 2019). In this section, we will analyse the other bifurcation phenomenon that occur when H^Q is singular with 0 as a simple eigenvalue. For simplicity we choose a coordinate system such that the bifurcation point is located at $(x, y, t, r) = (0, 0, 0, 0)$ and the H^Q is a diagonal matrix. We consider a bifurcation point characterized by the following set of degeneracy conditions

$$Q_0 = 0, \;\; \partial_x Q_0 = 0, \;\; \partial_y Q_0 = 0 \tag{3.4}$$

and

$$H_0^Q = \begin{pmatrix} \partial_{xx} Q_0 & \partial_{xy} Q_0 \\ \partial_{xy} Q_0 & \partial_{yy} Q_0 \end{pmatrix} = \begin{pmatrix} 0 & 0 \\ 0 & \lambda \end{pmatrix}, \tag{3.5}$$

where subscript 0 is used to denote an evaluation at the bifurcation point $(x, y, t, r) = (0, 0, 0, 0)$ and λ is a nonzero parameter. To characterize the structure of the bifurcation curves at the bifurcation point we assume some regularity in the form of the following

set of non-degeneracy conditions

$$\partial_t Q_0 \neq 0, \;\; \partial_r Q_0 \neq 0, \;\; \partial_{xxx} Q_0 \neq 0, \tag{3.6}$$

and that

$$\begin{pmatrix} \partial_{xt} Q_0 & \partial_{xr} Q_0 \\ \partial_t Q_0 & \partial_r Q_0 \end{pmatrix} \text{ is non-singular.} \tag{3.7}$$

Based on the above assumptions, we will now analyse the structure of the bifurcation curves in a neighbourhood of the codimension two point. First we consider the following Jacobian

$$J = \frac{\partial(\partial_y Q, \partial_x Q, Q)}{\partial(y, t, r)} = \begin{pmatrix} \partial_{yy} Q & \partial_{yt} Q & \partial_{yr} Q \\ \partial_{xy} Q & \partial_{xt} Q & \partial_{xr} Q \\ \partial_y Q & \partial_t Q & \partial_r Q \end{pmatrix}, \tag{3.8}$$

which simplifies to

$$J_0 = \begin{pmatrix} \lambda & \partial_{yt} Q_0 & \partial_{yr} Q_0 \\ 0 & \partial_{xt} Q_0 & \partial_{xr} Q_0 \\ 0 & \partial_t Q_0 & \partial_r Q_0 \end{pmatrix} \tag{3.9}$$

when it is evaluated at the bifurcation point. Since $\lambda \neq 0$ it follows by the non-degeneracy condition (3.7) that J_0 is non-singular. Hence, we can apply the implicit function theorem to conclude that there exist unique local functions $y = Y(x), t = T(x), r = R(x)$ satisfying

$$Y(0) = 0, \;\; T(0) = 0, \;\; R(0) = 0, \tag{3.10}$$

and

$$\begin{aligned} \partial_y Q(x, Y(x), T(x), R(x)) &= 0, \\ \partial_x Q(x, Y(x), T(x), R(x)) &= 0, \\ Q(x, Y(x), T(x), R(x)) &= 0. \end{aligned} \tag{3.11}$$

The functions T and R give a parametric representation of the bifurcation curve in the (t, r) parameter space. The shape of the bifurcation curve is given by the derivatives of T and R at the bifurcation point $x = 0$. We now set out to compute these derivatives. By implicit differentiation of the equations in (3.11), we obtain that

$$J \begin{pmatrix} Y'(x) \\ T'(x) \\ R'(x) \end{pmatrix} = - \begin{pmatrix} \partial_{xy} Q \\ \partial_{xx} Q \\ \partial_x Q \end{pmatrix}, \tag{3.12}$$

which evaluated in $x = 0$, gives us

$$\begin{pmatrix} Y'(0) \\ T'(0) \\ R'(0) \end{pmatrix} = -J_0^{-1} \begin{pmatrix} \partial_{xy} Q_0 \\ \partial_{xx} Q_0 \\ \partial_x Q_0 \end{pmatrix} = \begin{pmatrix} 0 \\ 0 \\ 0 \end{pmatrix}. \tag{3.13}$$

Since $(T'(0), R'(0)) = (0, 0)$, we have a non-regular point on the bifurcation curve. To classify the singularity we compute the second order derivatives, which are found by implicitly differentiating (3.12) and evaluating the derivatives at $x = 0$:

$$\begin{pmatrix} Y''(0) \\ T''(0) \\ R''(0) \end{pmatrix} = -J_0^{-1} \left(\begin{pmatrix} \partial_{xxy} Q_0 \\ \partial_{xxx} Q_0 \\ \partial_{xx} Q_0 \end{pmatrix} + 2J_0' \begin{pmatrix} Y'(0) \\ T'(0) \\ R'(0) \end{pmatrix} \right) = -J_0^{-1} \begin{pmatrix} \partial_{xxy} Q_0 \\ \partial_{xxx} Q_0 \\ 0 \end{pmatrix},$$

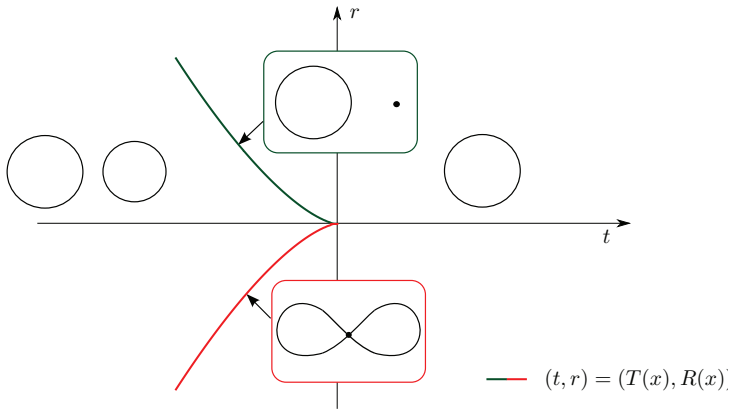

Figure 2: Illustration of a bifurcation curve with a cusp singularity at the codimension two bifurcation point $(t, r) = (0, 0)$ satisfying the assumptions in (3.4)-(3.7). The topological structures of the $Q = 0$ contour curves are shown in the figure and the bifurcation states are depicted in red and green boxes.

where

$$J_0' = \left(\frac{\partial J}{\partial x} + \frac{\partial J}{\partial y}Y'(x) + \frac{\partial J}{\partial t}T'(x) + \frac{\partial J}{\partial r}R'(x)\right)_0 = \left.\frac{\partial J}{\partial x}\right|_0.$$

Hence, it follows that

$$T''(0) = -\frac{\partial_r Q_0 \partial_{xxx} Q_0}{\partial_{xt} Q_0 \partial_r Q_0 - \partial_t Q_0 \partial_{xr} Q_0}, \tag{3.14}$$

$$R''(0) = \frac{\partial_t Q_0 \partial_{xxx} Q_0}{\partial_{xt} Q_0 \partial_r Q_0 - \partial_t Q_0 \partial_{xr} Q_0}. \tag{3.15}$$

From the non-degeneracy conditions (3.6) and (3.7) it is clear that $T''(0)$ and $R''(0)$ are both well-defined and non-zero and hence we have a quadratic cusp at $(r, t) = (0, 0)$ (see e.g. Rutter (2000)). To determine the order n of the cusp we must find the first derivatives of order $n > 2$, such that

$$\frac{T^{(n)}(0)}{R^{(n)}(0)} \neq \frac{T''(0)}{R''(0)} = -\frac{\partial_r Q_0}{\partial_t Q_0}. \tag{3.16}$$

We will show that this holds already for $n = 3$, which makes the cusp singularity an ordinary cusp. By implicitly differentiating (3.12) again we get that

$$\begin{pmatrix} Y'''(0) \\ T'''(0) \\ R'''(0) \end{pmatrix} = -J_0^{-1}\left(3J_0'\begin{pmatrix} Y''(0) \\ T''(0) \\ R''(0) \end{pmatrix} + \begin{pmatrix} \partial_{xxxy} Q_0 \\ \partial_{xxxx} Q_0 \\ \partial_{xxx} Q_0 \end{pmatrix}\right).$$

Hence, it follows that

$$T'''(0) = \frac{-\partial_r Q_0 A + \partial_{xr} Q_0 B}{\partial_{xt} Q_0 \partial_r Q_0 - \partial_t Q_0 \partial_{xr} Q_0}, \tag{3.17}$$

$$R'''(0) = \frac{\partial_t Q_0 A - \partial_{xt} Q_0 B}{\partial_{xt} Q_0 \partial_r Q_0 - \partial_t Q_0 \partial_{xr} Q_0}, \tag{3.18}$$

where

$$A = 3\partial_{xxr} Q_0 R''(0) + 3\partial_{xxt} Q_0 T''(0) + 3\partial_{xxy} Q_0 Y''(0) + \partial_{xxxx} Q_0,$$
$$B = 3\partial_{xr} Q_0 R''(0) + 3\partial_{xt} Q_0 T''(0) + \partial_{xxx} Q_0 = -2\partial_{xxx} Q_0.$$

The last non-degeneracy condition in (3.6) then implies that B is non-zero, and hence it follows from (3.7) that at least one of the quantities $T'''(0)$ and $R'''(0)$ must be non-zero as well. Assume now that $R'''(0) \neq 0$ and consider the ratio

$$\frac{T'''(0)}{R'''(0)} = \frac{-\partial_r Q_0 A + \partial_{xr} Q_0 B}{\partial_t Q_0 A - \partial_{xt} Q_0 B}. \tag{3.19}$$

The following argument is completely identical in the case where $T'''(0) \neq 0$ and the reciprocal (3.19) is considered. We now assume that

$$\frac{T'''(0)}{R'''(0)} = \frac{T''(0)}{R''(0)}. \tag{3.20}$$

However, this implies that

$$\partial_{xr} Q_0 \partial_r Q_0 B - \partial_t Q_0 \partial_{xt} Q_0 B = 0, \tag{3.21}$$

and since $B \neq 0$ this expression violates the non-degeneracy condition (3.7) and we can conclude that

$$\frac{T'''(0)}{R'''(0)} \neq \frac{T''(0)}{R''(0)}. \tag{3.22}$$

This argument concludes the proof that we have an ordinary cusp singularity on a bifurcation curve in the (t, r) parameter space. Since $\partial_{xxx} Q_0 \neq 0$, it also follows for any x sufficiently close to zero that the Hessian H^Q is definite when x has one sign, and indefinite when x has the opposite sign. Hence, the two branches that meet at the cusp singularity are respectively a punching bifurcation curve and a pinching bifurcation curve. A sketch of the bifurcation diagram close to the bifurcation point is shown in figure 2. The orientation of the cusp and the type of bifurcation on each of the two branches will depend on the signs of the non-degenerate quantities in (3.6) and (3.7).

3.2. *Codimension two bifurcation in models with symmetry*

As discussed in § 2 the core growth model has the x-axis as a line of symmetry, i.e. $Q(x, y, r, t) = Q(x, -y, r, t)$. This symmetry may lead to a special type of codimension two bifurcation which only occurs in such models. The reason is that the symmetry implies, for any set of non-negative integers k, l, m and n, that

$$\partial_x^k \partial_y^l \partial_t^m \partial_r^n Q(x, 0, t, r) = 0 \quad \text{if } l \text{ is an odd number.} \tag{3.23}$$

If we consider a bifurcation point satisfying the degeneracy and non-degeneracy conditions described in § 3.1, it would in general not affect the bifurcation phenomenon if we make the analysis in a coordinate system where the x- and y-coordinates are interchanged.

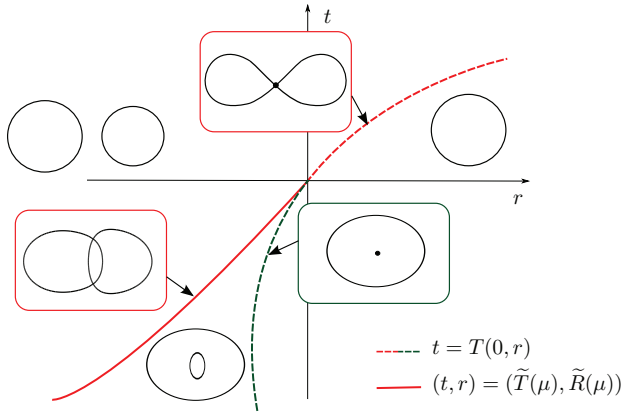

Figure 3: Illustration of a bifurcation diagram in the neighbourhood of a codimension two point satisfying the symmetry condition (3.23). The solid and dashed curves are sketches of the two bifurcation curves meeting with a common tangent line at $(t, r) = (0, 0)$. The topological structures of the $Q = 0$ contour curves are illustrated in the figure and the bifurcation states are depicted in red and green boxes. See appendix A for further details on $T, \widetilde{T}$ and $\widetilde{R}$.

The symmetry in the core growth model implies, however, that $\partial_{yyy}Q$, $\partial_{yt}Q$ and $\partial_{yr}Q$ are all zero at any point on the line of symmetry. The non-degeneracy conditions in (3.6) and (3.7) will therefore be violated if the codimension two point is located at the line of symmetry. In Appendix A we analyse this case in detail. The non-degeneracy conditions

$$\partial_t Q_0 \neq 0, \quad \partial_r Q_0 \neq 0 \tag{3.24}$$

are kept, and other conditions are imposed to ensure a certain regularity (A 5), (A 6). The analysis in Appendix A shows that two distinct branches of bifurcation curves meet with a common tangent line at the codimension two point and separates the parameter space into three different regions. An example of a bifurcation diagram close to the codimension two point $(t, r) = (0, 0)$ is shown in figure 3. The orientation of the curves and the type of bifurcation on each part of the branches will depend on the signs of the non-degenerate quantities.

4. Application to vortex pair interactions

4.1. *Topological bifurcations in the core growth model*

Elsas & Moriconi (2017) showed that a Gaussian vorticity field has a positive Q-value in a circular region with radius $r \approx \sigma/0.89$. As described in § 2 the core growth model evolves as a superposition of two Gaussian vortices, but since Q does not depend linearly on the flow field bifurcations in the vortex structure can occur. These bifurcations can be tracked by solving the degeneracy conditions (3.1) with Q is given by the analytical expression in (2.17). In the case where $\alpha \geqslant 1$, we obtain the bifurcation diagram shown in figure 4 when the solution is projected onto the (σ, α) parameter plane. The bifurcation curves separate the parameter plane into four distinct regions. The vortex structure in each region is illustrated with an example of a $Q = 0$ contour curve. The color of a

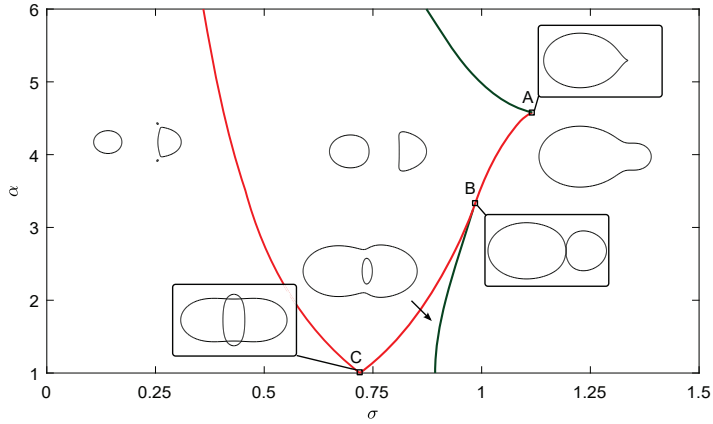

Figure 4: Bifurcation diagram of the merging process in the core growth model for $\alpha \geqslant 1$. The bifurcation curves separate the (σ, α) parameter plane into four distinct regions with different vortex topologies. Crossing a green (red) part of the bifurcation curve results in a punching (pinching) bifurcation.

bifurcation curve indicates whether a pinching or a punching bifurcation occur when crossing the curve. The three points $(\sigma_A, \alpha_A) \approx (1.12, 4.58)$, $(\sigma_B, \alpha_B) \approx (0.98, 3.37)$, and $(\sigma_C, \alpha_C) \approx (0.72, 1)$ mark the places where two bifurcation curves collide. These points divide the flow into three different α-regimes in which the vortex interactions occur through different robust processes. The temporal evolution of the merging process within each of the three regimes are illustrated by the examples in figure 5b,c,d. The figure also includes the symmetric case where $\alpha = 1$. The bifurcation states depicted in the red and green boxes correspond to the vortex structures on the bifurcation curves in figure 4. The top-down symmetry (2.18) implies that any bifurcations away from the line of symmetry occur simultaneously in pairs. For all values of α the initial and final vortex structure are topologically identical but the temporal evolution is quite different. In the low α-regime, $1 \leqslant \alpha < \alpha_A$, figure 5a,b, the merging process proceeds in two steps: first a single vortex with a hole is formed by two simultaneous pinching bifurcations. Subsequently the hole disappears in a punching bifurcation. In the intermediate α regime, $\alpha_B < \alpha < \alpha_A$, figure 5c, the two vortices merge in a single pinching bifurcation. In the high α regime, $\alpha > \alpha_A$, figure 5d, no merging as such occurs, but the weakest vortex is suppressed by the strongest in a punching bifurcation.

When we turn our attention to the common initial vortex structure, we observe two zero level curves of Q located around the Gaussian vortex centers. In addition we notice two smaller vortices that were not immediately expected and grow very slowly in size. For the sake of simplicity, we will only examine them, in the case where $\alpha = 1$. Due to the rotational symmetry in this case, they have a fixed location around $(x, y) = (0, \pm 1)$ and the analytical expression of the Q-field can easily be evaluated

$$Q(0, \pm 1, 1, \sigma) = \frac{e^{-4/\sigma^2}}{\pi^2 \sigma^2}. \tag{4.1}$$

It is clear that $(x, y) = (0, \pm 1)$ are singular points of Q in the initial state where $\sigma = 0$. Furthermore, $Q(\pm 1, 0, 1, \sigma)$ has a positive value for any $\sigma > 0$ and therefore the small

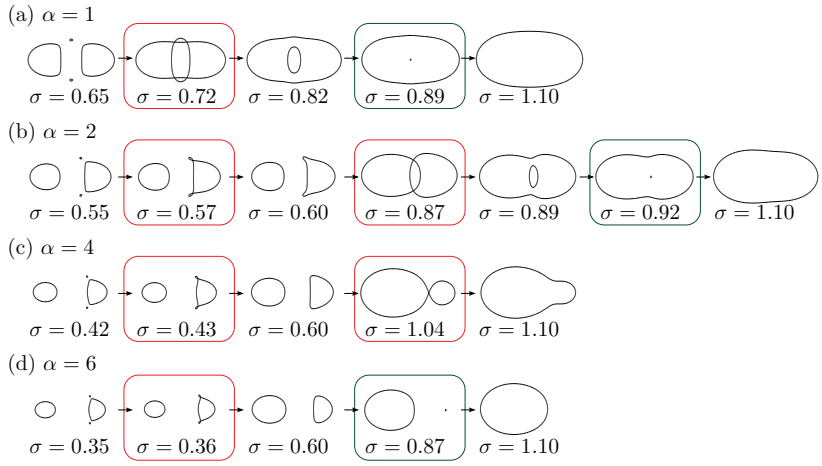

Figure 5: Evolution of the vortex structure at selected values of $\alpha \geqslant 1$. For each value of α, all the observed topologies of the $Q = 0$ contour curves are shown in the order of evolution. The structurally unstable bifurcation states are depicted in red and green boxes.

vortices are indeed present from the beginning. Furthermore, we see that the value of Q increases slower than any power of σ. From the examples in figure 5 we see that the small vortices merge with the weakest of the two main vortices in two simultaneous pinching bifurcations that occur when crossing the far left the bifurcation curve in figure 4.

The key to understanding the complete picture of the vortex pair interactions are the singular points, A, B, C, on the bifurcation curves in figure 4. At these points we observe bifurcations with higher codimension and the corresponding vortex topologies are depicted in black boxes. At A there is a critical point on the zero level curve of Q at $(x_A, y_A) \approx (0.94, 0)$. By evaluating H^Q precisely at this point, we find that the degeneracy condition (3.5) is satisfied and we can employ our codimension two theory in § 3.1. The two parameters t and r are in this case interpreted as $t = \sigma - \sigma_A$ and $r = \alpha - \alpha_A$. Based on theory, we conclude that the singular point at A is an ordinary cusp singularity on the bifurcation curve and the two branches that meet at the cusp singularity are respectively a punching bifurcation curve and a pinching bifurcation curve. This analysis is completely consistent with the result in figure 4 and leads to the same conclusion: a pair of co-rotating vortices merge only if their strength ratio $\alpha = \Gamma_1/\Gamma_2$ is less than $\alpha_A = 4.58$. At B there is a critical point on the zero level curve of Q at $(x_B, y_B) \approx (3.91, 0)$. Since this critical point is located at the line of symmetry and H^Q_B satisfy the degeneracy condition (A 2), we can employ our codimension two theory in Appendix A. Based on theory, we conclude that two distinct branches of bifurcation curves meet with a common tangent at the singular point B. Therefore, the point marks the transition between two regimes where merging proceeds as two different sequences of bifurcations exactly as shown in figure 4. The last singular point at C is solely due to the rotational symmetry of order 2 when $\alpha = 1$ and the point represents a global bifurcation where four distinct bifurcations are restricted to occur simultaneously.

The bifurcation diagram in figure 4 gives us a complete picture of vortex pair inter-

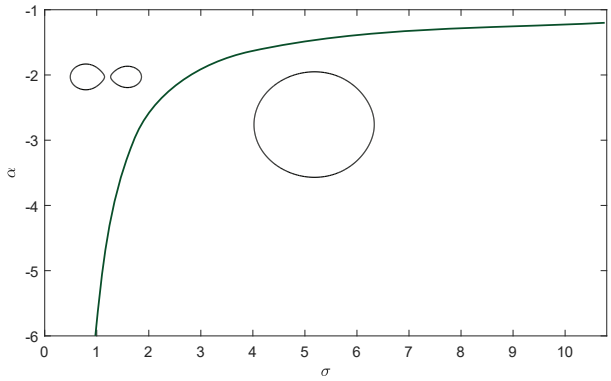

Figure 6: Bifurcation diagram of the merging process in the core growth model for $\alpha < -1$. The green bifurcation curve separates the (σ, α) parameter plane into two distinct regions with different vortex topologies. The topological structures are illustrated with an example of a $Q = 0$ contour curve within each region. On the bifurcation curve one of the vortices disappears in a punching bifurcation.

actions when considering two co-rotating vortices. Since it is only possible to show the diagram for a finite range of α, the upper limit of $\alpha = 6$ is an arbitrary limit. However, by increasing α significantly, we conclude that the qualitative picture is the same for $\alpha > 6$. The limit where α is increased to infinity corresponds to a single Lamb-Oseen vortex, and therefore we expect both bifurcation curves to approach $\sigma = 0$ for $\alpha \to \infty$. For all values of α there is only a single vortex left for $\sigma \geqslant 1.12$. As proven by Gallay & Wayne (2005) the Lamb-Oseen vortex is an attracting solution for any integrable initial vorticity field. Therefore, we expect that the final vortex region converges to a circular region when σ is further increased.

For $\alpha < 0$ the vortices have opposite signs of vorticity, and as discussed in § 3 they cannot merge in a pinching bifurcation. This is confirmed by the bifurcation diagram for $\alpha < -1$ in figure 6. For all values of α, the only event is the disappearance of the weakest vortex in a punching bifurcation. When α approaches -1, the time for the punching bifurcation goes to infinity.

4.2. *Navier-Stokes simulations of vortex pair interactions*

We want to compare the results of the analytical core growth model with Navier-Stokes simulations subject to the same initial condition. This is done by solving the vorticity transport equation (2.1) numerically. Following Andersen *et al.* (2019) we do not reparameterize the vorticity transport equation, but control the Reynolds number directly through the kinematic viscosity, ν. In this study we define the Reynolds number as an average of the individual vortex Reynolds numbers

$$Re = \frac{|\Gamma_1| + |\Gamma_2|}{2\nu}, \tag{4.2}$$

which is consistent with earlier studies by Andersen *et al.* (2019), Meunier *et al.* (2002) and Jing *et al.* (2010). Since our system is isolated the total absolute vorticity

$$\int\int |\omega| dxdy = |\Gamma_1| + |\Gamma_2| \tag{4.3}$$

must be conserved. Therefore, we fix $|\Gamma_1| + |\Gamma_2| = 10$ in all simulations and control the Reynolds number by varying ν. The conservation of the total absolute vorticity is also monitored as a check of the numerical scheme.

As discussed in § 2 we are primarily interested in comparing the models at low values of Reynolds numbers and we choose to make simulations only for $\mathrm{Re} \leqslant 100$. We restrict the computational domain to the region where $(x, y) \in [-9, 9] \times [-9, 9]$. Since $\mathrm{Re} \leqslant 100$ and we have a simple square domain a finite difference method with an explicit Euler integrator scheme suffices (Andersen *et al.* 2019; E & Liu 1996*a*,*b*). If the field variable with index ij is the value at grid point (i, j) we have the iterative scheme

$$\begin{aligned} \omega_{ij}^{n+1}(\Delta t^n) &= \omega_{ij}^n - \left(\mathbf{u}_{ij}^n \cdot (\boldsymbol{\nabla}\omega_{ij}^n) - \nu\nabla^2\omega_{ij}^n\right)\Delta t^n, \\ \nabla^2\psi_{ij}^{n+1} &= -\omega_{ij}^{n+1}, \quad u_{ij}^{n+1} = \frac{\partial\psi_{ij}^{n+1}}{\partial y}, \quad v_{ij}^{n+1} = -\frac{\partial\psi_{ij}^{n+1}}{\partial x}, \end{aligned} \tag{4.4}$$

where n is the integrator iteration index and Δt^n the time step used by the scheme at index n. We apply an adaptive time step method, where the error estimator is given by the supremum of the absolute differences in the vorticity field using Δt^n and $\Delta t^n/2$, i.e. $\mathrm{err} = \sup\{|\omega_{ij}^n(\Delta t^n) - \omega_{ij}^n(\Delta t^n/2)|\}$; the relative maximum tolerance is set to 0.1 %, and with maximum time step of 10^{-3} in simulation time units. The spatial derivatives are approximated by central differences using a 300×300 grid with grid spacing $\Delta x = 0.06$, and we apply periodic boundary conditions. The Poisson problem is solved using the direct method described in Hansen (2011). We note that this simple scheme has been tested against higher order schemes as well as for finite size effects etc. (Andersen *et al.* 2019).

The initial condition for the core growth model is two Dirac-delta distributions located at $(x, y) = (\pm 1, 0)$. Such an initial condition can not be handled by our mesh-based method. Therefore, we consider an initial condition with two slightly diffused Gaussian peaks,

$$\omega_{ij}^0 = \frac{\alpha}{\pi\sigma_0^2} e^{-\frac{(x_i+1)^2+y_j^2}{\sigma_0^2}} + \frac{1}{\pi\sigma_0^2} e^{-\frac{(x_i-1)^2+y_j^2}{\sigma_0^2}}, \tag{4.5}$$

where $\sigma_0 = \Delta x$. From the ω_{ij}^0 the stream function ψ_{ij}^0 can be found, which also gives the initial velocity field.

4.3. *Topological bifurcations in Navier-Stokes simulations*

In figure 7 and figure 8 the topological vortex structure is shown for selected simulations with $\mathrm{Re} = 10$ and $\mathrm{Re} = 100$, respectively. It is important to make clear that the simulations are not performed in a co-rotating frame and we therefore expect the two vortices to rotate relative to each other. In both figures we observe evolution patterns that are qualitatively similar to the ones observed in the core growth model. For $\alpha = 1$, the vortex structure still has a rotational symmetry of order two and for increasing values of α we observe three different sequences of topological structures describing the merging process. For the smallest values of α, the process involves forming a vortex with a hole in it. For intermediate values of α, merging occur as a single pinching bifurcation and no merging is observed for large values of α where the weakest vortex is suppressed in a punching bifurcation. Although there are qualitative similarities, it is clear that

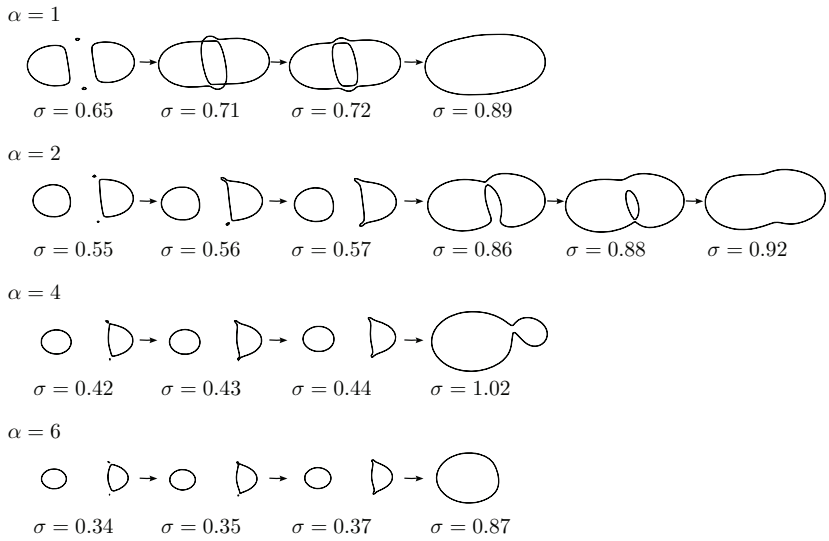

Figure 7: Navier-Stokes simulations at Re = 10. The evolution of the vortex structure is shown at selected values of $\alpha \geqslant 1$. For each value of α, all the structurally stable topologies of the $Q = 0$ contour curve are shown in the order of evolution.

the quantitative picture changes with increasing Reynolds numbers. For both values of Reynolds number there is no line of symmetry in the topological vortex structure. The bifurcations that occur simultaneously in the core growth model are here observed at two distinct values of σ. We notice that the symmetry is only slightly broken in the case of a low Reynolds number.

For each of the two selected Reynolds numbers, we have performed simulations with more than 30 different values of $1 \leqslant \alpha \leqslant 6$. From each simulation, we have marked the observed bifurcation points in the (σ, α) parameter plane and constructed the bifurcation curves shown as the solid lines in figure 9a,b. The color of the bifurcation curves again indicates the type of bifurcation. For the purpose of comparison the bifurcation curves in the core growth are drawn as dashed lines in the background of the bifurcation diagrams. In both cases, we observe that the codimension two point at B has disappeared. However, this was expected as we do not have a line of symmetry in the Navier-Stokes simulations. With the disappearance of B, a new codimension two point D has arisen in both cases. Since a pinching and a punching bifurcation curve meet at D they must form another cusp singularity. The break of symmetry causes the global bifurcation point at C to separate into two singular points C_1, C_2 where rotational symmetry of order 2 is preserved. The codimension two point at A is preserved as a cusp singularity but the exact location varies slightly. By recalling that the cusp singularity represents the merging threshold, we conclude that for Re = 100 vortex merging is only observed if the strength ratio, $\alpha = \Gamma_1/\Gamma_2$ is less than $\alpha_A = 4.05$.

Overall, we observe the same topological structures as seen in the core growth model. Only the bifurcations that were restricted by the built-in symmetry are qualitatively changed. The codimension two points still divide the flow into three different α regimes:

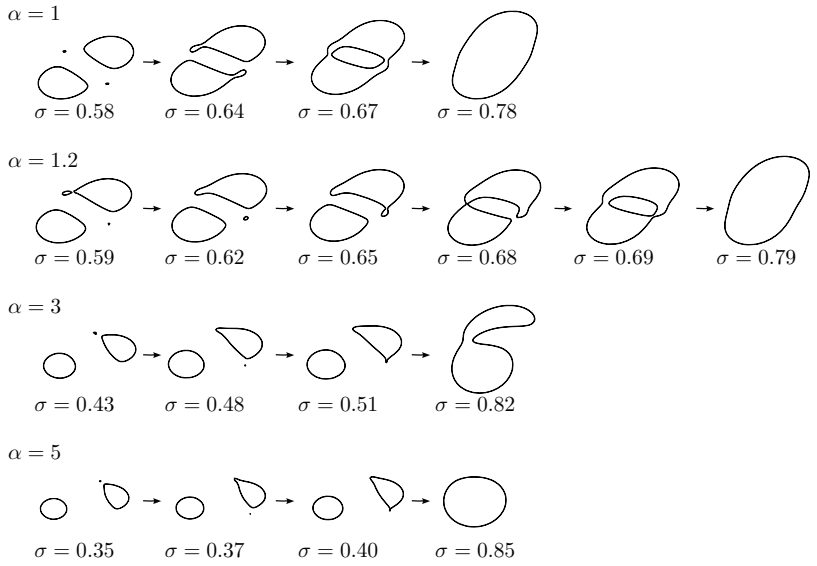

Figure 8: Navier-Stokes simulations at Re = 100. The evolution of the vortex structure is shown at selected values of $\alpha \geqslant 1$. For each value of α, all the structurally stable topologies of the $Q = 0$ contour curve are shown in the order of evolution.

$1 \leqslant \alpha < \alpha_D$, $\alpha_D \leqslant \alpha < \alpha_A$ and $\alpha > \alpha_A$. The examples in figure 7 and 8 are chosen to illustrate the temporal evolution of the merging process within each of the three regimes.

We notice that the small vortices growing around the infinitely degenerate critical points are also present in the Navier-Stokes simulations. Therefore, we conclude that they are not just mathematical artifacts that exist in the core growth model due to a forced symmetry. They, on the other hand, have a significant impact on the observed topological structures. When the small vortices merge with the weaker of the two main vortices, its structure is deformed in a manner that enables the subsequent formation of the interesting vortex structure with a hole inside it. One could argue that the small vortices are artifacts due to the Q-criterion. In practice it is common to choose a non-zero threshold to identify the vortex boundaries. The threshold is ideally chosen such that strong vortices are captured while small spurious vortices are ignored. Unfortunately, it is very difficult, if not impossible, to determine a suitable threshold value a priori because the optimal threshold value tends to be problem dependent (see Chen *et al.* (2015) and Chakraborty *et al.* (2005)). From the present study it is also clear that the infinitely degenerate critical points out of which the small vortices grow have an effect on the shape of the vortices and we have therefore chosen to stick with the original Q-criterion as it is defined in (1.1).

5. Discussion

With a topological approach, we revisited the vortex merger problem. The final state of an interacting pair of vortices is known (Gallay & Wayne 2005) to be a single Lamb-

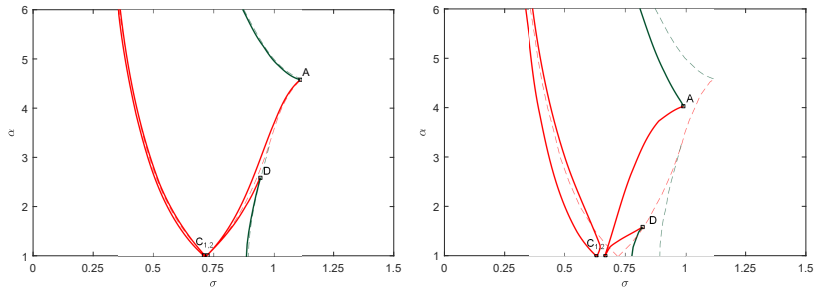

(a) $Re = 10$. (b) $Re = 100$.

Figure 9: Bifurcation diagrams of the merging process in Navier-Stokes simulations with (a) $Re = 10$ and (b) $Re = 100$. The solid curves are the bifurcation curves in the Navier-Stokes simulations. The bifurcation curves in the core growth model are drawn as dashed lines for comparison.

Oseen solution. The focus of our studies has therefore been to elucidate the dynamics that take place as the system evolves into the Lamb-Oseen solution. Based on the Q-criterion, we have completed a mathematical description that tells us which topological bifurcations we can expect when two parameters are allowed to vary. It has proven to be useful to identify the codimension two points as they organize the bifurcation diagram and divide it into different regimes where different sequences of bifurcations form the merging process. The possible types of bifurcations found from theory also serve as a template that facilitate the construction of a bifurcation diagram for a specific value of Reynolds number. As an example, we know that a pinching and a punching bifurcation curve form a cusp singularity where they meet. Therefore, it is possible to accurately construct the bifurcation curves in figure 9 based on a finite number of Navier-Stokes simulations.

One of the main objectives in this study was to investigate vortex pair interactions using the core growth model. The major advantage of the model is the possibility to determine an analytical expression for Q in the co-rotating frame. With this expression the topology of the $Q = 0$ contour curves was easily studied with a precision that made it possible to depict the structurally unstable bifurcation states in figure 5. The utility of the model was examined by comparing it with Navier-Stokes simulations. Except for the bifurcations that were restricted by the built-in symmetry in the core growth model, we observe the same topological structures in the Navier-Stokes simulations. For Reynolds numbers up to at least 100, the qualitative picture was the same. Furthermore, we observe an excellent quantitative agreement with simulations for Reynolds numbers below 10. Thus, depending on the purpose, there are good opportunities to use core growth model instead of solving the Navier-Stokes equation with low Reynolds numbers.

Most previous studies have focused on symmetric merging of two identical vortices or, to a lesser extent, asymmetric merging with a few examples of different strength ratios, see, among others, Melander *et al.* (1988), Meunier *et al.* (2002), Dritschel (1995). In two recent studies by Jalali & Dritschel (2018, 2020) the general inviscid interactions of vortex patches is studied with many examples over a wide parameter space including ratio of sizes and vorticity. Our study is not the first that attempts to describe all interaction scenarios in terms of different flow regimes. Dritschel & Waugh (1992) identify

five different flow regimes to characterize the inviscid interaction of two differently sized vortex patches with equal uniform vorticity. These different flow regimes were based on the "efficiency" of the vortex interactions, which was quantified by computing the ratio of the final to initial circulation for each of the vortices. Trieling *et al.* (2005) show that similar flow regimes can be used to characterize the inviscid interactions of two-dimensional vortices with a continuous vorticity distributions. They notice, however, that the regime boundaries are highly sensitive to the vorticity profile.

It is beyond the scope of this work to study the immediate change in the circulation within the zero level curves of Q during a merging process. A comparison between the initial and long term asymptotic state is, however, possible. We recall that a Gaussian vorticity field has a positive Q-value in a circular region with radius $r \approx \sigma/0.89$ (Elsas & Moriconi 2017). The circulation within the $Q = 0$ level curve of a Gaussian vortex can therefore be directly computed as

$$\int_0^{\sigma/0.89} \omega(r) 2\pi r dr = \int_0^{\sigma/0.89} \frac{\Gamma}{\pi\sigma^2} e^{-r^2/\sigma^2} 2\pi r dr \approx 0.72\Gamma, \tag{5.1}$$

where Γ is the total circulation. Thus, the $Q = 0$ curve expands at a rate that makes the circulation constant within the Q-vortex. For sufficiently small values of σ the vorticity field of each of our two initial vortices can be assumed to be Gaussian distributed. Therefore, before any interaction, the circulation of the vortices must equal $0.72\Gamma_1$ and $0.72\Gamma_2$, respectively. Since the long time asymptotic state of interacting vortices is a single Gaussian vortex with total circulation $\Gamma_1 + \Gamma_2$, no matter how the transient dynamics evolve, the circulation of the final vortex must equal $0.72(\Gamma_1 + \Gamma_2)$. Hence, the circulation of the initial vortices is completely transferred to the final surviving vortex. Therefore, merging of viscous Q-vortices is always completely efficient, and is complete merging in the sense of Dritschel & Waugh (1992).

Brandt & Nomura (2010) use some of the same terms as Dritschel & Waugh (1992) to describe the flow regimes in a viscous setting at $Re = 5000$. All viscous interactions between vortices will eventually result in a single vortex, and therefore only three of the inviscid regimes are considered to occur: complete merger, partial merger and straining out. Brandt & Nomura (2010) specify three times that are important in the merging process, $t_{cr,1}$, $t_{cr,2}$ and $t_{de,2}$. For vortex i, $t_{cr,i}$ indicates the time where the vortex no longer diffuses as a single Gaussian vortex, i.e., the time where the square of the core radius no longer grows linearly. $t_{de,2}$ is the time characterizing the destruction of the weaker vortex 2. The weaker vortex is considered to be destroyed when its core vorticity no longer dominates the imposed strain rate field. This is the case when the Q-value is very small at the maximum point of vorticity for the weaker vortex.

Brandt & Nomura (2010) distinguish between two main regimes, depending on the order of $t_{cr,2}$ and $t_{de,2}$. For large values of α, the weak vortex disappears before it gets close to the strong vortex. This is denoted straining-out by Brandt & Nomura (2010) and characterized by $t_{de,2} < t_{cr,2}$. In our setting, this corresponds to the weakest vortex disappearing in a punching bifurcation. If $t_{cr,2} < t_{de,2}$ the two vortices interact before the weak one disappears. This is denoted merging, and occurs when α is close to 1. We detect merging in this sense when the two $Q = 0$ curves merge in a pinching bifurcation. In both classifications the latter regime is further subdivided. If $t_{cr,2} \approx t_{cr,1}$ (complete merger) Brandt & Nomura (2010) find detrainment of vorticity from both vortices and mutual entrainment of the core into a single vortex. If $t_{cr,2} < t_{cr,1}$ (partial merger) there is detrainment from both vortices, but the weaker vortex is destroyed. In our classification,

there is a regime where a hole is created inside the merged vortex, and one where there is not.

Hence, there are many similarities between the classification by Brandt & Nomura (2010) and the one we propose on the basis of Q alone, even if the flows are studied at very different Reynolds numbers. In the present study the physics is dominated by diffusion, and convection plays a very small role. In particular, there is no significant filamentation of vorticity (Andersen *et al.* 2019), and denoting the high α regime where the weak vortex disappears in a punching bifurcation straining-out does not reflect the actual dynamics. However, for higher Reynolds numbers, filamentation will also be detected by the shape of the $Q = 0$ contours. A first indication is visible for $\alpha = 3$ in figure 8. The transition to regimes with straining-out and detrainment as Reynolds number is increased can possibly be characterized by further bifurcations in the $Q = 0$ contours. From figure 9 we see that the point D moves to lower values of α as Re is increased. We expect that the regime with a vortex with an inner hole may be very small or disappear completely for higher values of Re.

The approach that is common to the studies of Dritschel & Waugh (1992), Trieling *et al.* (2005) and Brandt & Nomura (2010) provides no information about the topological vortex structure during the merging process and it does not define merging as a bifurcation that occurs at a specific time. With our approach, we have the opportunity to connect the process to a rigorous mathematical theory and we avoid a number of choices, such as to define what the core radius is. By using the core growth model we have mapped out all vortex pair interactions with a bifurcation diagram being valid for any choice of vortex strengths with a ratio $|\alpha| = |\Gamma_1/\Gamma_2| \leqslant 6$. To our knowledge, a similar bifurcation diagram has only been established once before in a recent study by Andersen *et al.* (2019). Their results are based on vortices being defined as local extrema of vorticity. Both studies agree that the core growth model matches well with Navier-Stokes simulations for low Reynolds numbers. It is, however, clear that the choice of vortex criterion is crucial to the analysis. While the Q-criterion provides information on the physical extent of a vortex, the vorticity criterion only tells us whether or not a feature point for the vortex exists. With the vorticity criterion, it is impossible to distinguish between vortex merging and what we see in this study as suppression of the weakest vortex. Therefore, the threshold for merging and the observed vortex structure with a hole inside are both completely new results that have provided new insights into the intermediate evolution of vortex merging.

Our study has only focused on mapping out all vortex pair interactions with point vortices as initial condition. Inspired by Folz & Nomura (2017) it would be an obvious continuation of our study to consider two Gaussian vortices with different sizes as initial condition and analyse the effect of differing the vortex area versus the vorticity amplitude. By introducing yet another parameter, the possibility of bifurcations with a higher codimension also arises. It is therefore possible that such a study will require new theoretical considerations.

Acknowledgments. Financial support from Independent Research Fund Denmark, grant no. 6108-00246B, is gratefully acknowledged.

Declaration of Interests. The authors report no conflict of interest.

Appendix A. A theoretical description of codimension two phenomena in a symmetric model

In this appendix we analyse the codimension two bifurcation which is briefly discussed in § 3.2. We consider a flow with symmetry such that $Q(x, y, r, t) = Q(x, -y, r, t)$. For any set of non-negative integers k, l, m and n it then follows that

$$\partial_x^k \partial_y^l \partial_t^m \partial_r^n Q(x, 0, t, r) = 0 \quad \text{if } l \text{ is an odd number.} \tag{A 1}$$

The special codimension two bifurcation will only occur on the line of symmetry, $y = 0$, since the conditions in (A 1) only applies at the line of symmetry. For simplicity we analyse the phenomenon in a coordinate system where the bifurcation point is located at $(x, y, t, r) = (0, 0, 0, 0)$ and, as before, we use subscript 0 to denote evaluation at the bifurcation point. We consider a bifurcation point that is characterized by the following set of degeneracy conditions

$$Q_0 = 0, \;\; \partial_x Q_0 = 0, \;\; \partial_y Q_0 = 0, \tag{A 2}$$

combined with the non-degeneracy condition in (3.3) being violated such that

$$H_0^Q = \begin{pmatrix} \partial_{xx} Q_0 & \partial_{xy} Q_0 \\ \partial_{xy} Q_0 & \partial_{yy} Q_0 \end{pmatrix} = \begin{pmatrix} \lambda & 0 \\ 0 & 0 \end{pmatrix}, \tag{A 3}$$

for some $\lambda \neq 0$. In this section we prove that if the bifurcation point also satisfies the following non-degeneracy conditions

$$\partial_t Q_0 \neq 0, \;\; \partial_r Q_0 \neq 0, \tag{A 4}$$

$$\partial_{xyy} Q_0 \frac{\partial_{xt} Q_0 \partial_r Q_0 - \partial_{xr} Q_0 \partial_t Q_0}{\partial_{xx} Q_0 \partial_t Q_0} - \partial_{yyt} Q_0 \frac{\partial_r Q_0}{\partial_t Q_0} + \partial_{yyr} Q_0 \neq 0 \tag{A 5}$$

and

$$-3 \frac{(\partial_{xyy} Q_0)^2}{\partial_{xx} Q_0} + \partial_{yyyy} Q_0 \neq 0, \tag{A 6}$$

then two distinct branches of bifurcation curves meet tangentially at $(t, r) = (0, 0)$, as illustrated in figure 3.

We begin the proof by considering the following Jacobian

$$J = \frac{\partial(\partial_x Q, Q)}{\partial(x, t)} = \begin{pmatrix} \partial_{xx} Q & \partial_{xt} Q \\ \partial_x Q & \partial_t Q \end{pmatrix}, \tag{A 7}$$

which simplifies to

$$J_0 = \begin{pmatrix} \lambda & \partial_{xt} Q_0 \\ 0 & \partial_t Q_0 \end{pmatrix} \tag{A 8}$$

when it is evaluated at the bifurcation point. Since $\lambda \neq 0$ it follows from the non-degeneracy condition (A 4) that J_0 is non-singular. Hence, we can apply the implicit function theorem to conclude that there exist unique local functions $x = X(y, r), t = T(y, r)$ satisfying

$$X(0, 0) = 0, \;\; T(0, 0) = 0 \tag{A 9}$$

and

$$\partial_x Q(X(y, r), y, T(y, r), r) = 0, \quad Q(X(y, r), y, T(y, r), r) = 0. \tag{A 10}$$

Since Q, and hence also $\partial_x Q$, are symmetric functions in y, it follows that

$$\begin{aligned}\partial_x Q(X(-y,r),-y,T(-y,r),r) = \partial_x Q(X(-y,r),y,T(-y,r),r) = 0,\\ Q(X(-y,r),-y,T(-y,r),r) = Q(X(-y,r),y,T(-y,r),r) = 0.\end{aligned} \tag{A 11}$$

By comparing the expressions in (A 10) and (A 11) and based on the uniqueness of X and T we can conclude that X and T are also symmetric functions in y, i.e. $X(-y,r) = X(y,r)$ and $T(-y,r) = T(y,r)$. In order to give a parametric representation of the bifurcation curves we must solve the equation

$$\partial_y Q(X(y,r),y,T(y,r),r) = 0 \tag{A 12}$$

for y in terms of r. It follows from (A 1) that

$$\partial_y Q(X(0,r),0,T(0,r),r) = 0, \tag{A 13}$$

for any r. It follows that there exists a branch of bifurcation points which will remain on the line of symmetry $y = 0$. The curve, $t = T(0,r)$, gives us a parametric representation of this branch in the (t,r) parameter space. Since T is a continuously differentiable function the slope of the tangent at $r = 0$ can be determined by implicit differentiating (A 10), yielding

$$\partial_r T_0 = -\frac{\partial_r Q_0}{\partial_t Q_0}. \tag{A 14}$$

In figure 3 this branch of bifurcation points is illustrated by the dashed green curve. We expect, however, that there are other solutions of (A 12), where the bifurcation points are leaving the line of symmetry. Since Q is a symmetric function in y, $\partial_y Q$ must be an antisymmetric function in y. Hence, a Taylor expansion of the left hand side of (A 12) based at $(y,r) = (0,0)$ has the form

$$\partial_y Q(X(y,r),y,T(y,r),r) = Ayr + By^3 + Cyr^2 + \mathcal{O}(4), \tag{A 15}$$

where the terms of order 4 (or higher) contains only odd powers of y. The coefficients A, B and C can be expressed solely in terms of derivatives of Q evaluated at the bifurcation point. Only A and B will play a role and are given in (A 16) and (A 17). We assume they are non-zero, and that is exactly the non-degeneracy conditions in (A 5) and (A 6).

$$A = \partial_{xyy}Q_0 \frac{\partial_{xt}Q_0 \partial_r Q_0 - \partial_{xr}Q_0 \partial_t Q_0}{\partial_{xx}Q_0 \partial_t Q_0} - \partial_{yyt}Q_0 \frac{\partial_r Q_0}{\partial_t Q_0} + \partial_{yyr}Q_0 \neq 0, \tag{A 16}$$

and

$$B = -3\frac{(\partial_{xyy}Q_0)^2}{\partial_{xx}Q_0} + \partial_{yyyy}Q_0 \neq 0. \tag{A 17}$$

To obtain a parametric representation of the second branch of the bifurcation curve, we put $r = \mu y$ and define

$$F(y,\mu) = \frac{\partial_y Q(X(y,\mu y),y,T(y,\mu y),\mu y)}{y^2}. \tag{A 18}$$

From this definition we notice that $F(-y,-\mu) = -F(y,\mu)$. Therefore, F has the following Taylor expansion based at $(y,r) = (0,0)$,

$$F(y,\mu) = A\mu + By + \mathcal{O}(3). \tag{A 19}$$

Since $F(0,0) = 0$ and $\partial_y F(0,0) = B \neq 0$, the implicit function theorem establishes the existence of a unique solution $y = Y(\mu)$ satisfying that $Y(0) = 0$,

$$F(Y(\mu), \mu) = 0, \tag{A 20}$$

and hence

$$F(-Y(-\mu), \mu) = -F(Y(-\mu), -\mu) = 0. \tag{A 21}$$

By comparing the expressions in (A 20) and (A 21) and based on the uniqueness of Y we conclude that Y is an odd function. From the definition of Y it is clear that $(y, r) = (Y(\mu), \mu Y(\mu))$ is a solution to the equation in (A 12). A second branch of bifurcation points in the (t, r) parameter space can therefore be determined by the parametric equations

$$t = \widetilde{T}(\mu) = T(Y(\mu), \mu Y(\mu)), \tag{A 22}$$

$$r = \widetilde{R}(\mu) = \mu Y(\mu). \tag{A 23}$$

It follows from the definitions of T and Y that $\widetilde{T}(0) = 0$ and $\widetilde{R}(0) = 0$. Furthermore, we see that

$$\widetilde{T}(-\mu) = T(Y(-\mu), -\mu Y(-\mu)) = T(-Y(\mu), \mu Y(\mu)) = T(Y(\mu), \mu Y(\mu)) = \widetilde{T}(\mu) \tag{A 24}$$

and

$$\widetilde{R}(-\mu) = -\mu Y(-\mu) = \mu Y(\mu) = \widetilde{R}(\mu). \tag{A 25}$$

Since both $\widetilde{T}$ and $\widetilde{R}$ are even functions, it follows that $\widetilde{R}'(0) = \widetilde{T}'(0) = 0$ and it is clear that $(t, r) = (0, 0)$ must be a singular point on the curve. The parameter values $\mu > 0$ and $\mu < 0$ correspond to the two branches on either side of the singular point. Since $\widetilde{T}$ and $\widetilde{R}$ are even functions it is clear that the two branches must coincide and $(t, r) = (0, 0)$ is in fact an endpoint of the parametric curve as illustrated in figure 3. The tangent to the curve is not well-defined at the endpoint but we notice that the limiting tangent direction can be computed as

$$\lim_{\mu \to 0} \left(\frac{\widetilde{T}'(\mu)}{\widetilde{R}'(\mu)} \right) = \frac{\widetilde{T}''(0)}{\widetilde{R}''(0)} \tag{A 26}$$

if $\widetilde{R}''(0) \neq 0$. Thus, we must compute the second order derivatives of $\widetilde{T}$ and $\widetilde{R}$ at $\mu = 0$. By implicit differentiating (A 20) we obtain

$$Y'(0) = -\frac{A}{B} \neq 0, \tag{A 27}$$

implying that

$$\widetilde{T}''(0) = 2Y'(0)\partial_r T_0 = -\frac{2A\partial_r Q_0}{B\partial_t Q_0} \neq 0, \tag{A 28}$$

$$\widetilde{R}''(0) = 2Y'(0) = -\frac{2A}{B} \neq 0. \tag{A 29}$$

Summing up we get that

$$\lim_{\mu \to 0} \left(\frac{\widetilde{T}'(\mu)}{\widetilde{R}'(\mu)} \right) = \frac{\dfrac{2A\partial_r Q_0}{B\partial_t Q_0}}{-\dfrac{2A}{B}} = -\frac{\partial_r Q_0}{\partial_t Q_0}, \tag{A 30}$$

which implies that both branches of the bifurcation curve share a common tangent line in $(t, r) = (0, 0)$ as illustrated in figure 3. The orientation of the bifurcation curves and the type of bifurcation on each part of the branches will depend on the signs of the non-degenerate quantities.

REFERENCES

Andersen, M., Schreck, C., Hansen, J. S. & Brøns, M. 2019 Vorticity topology of vortex pair interactions at low reynolds numbers. *European Journal of Mechanics, B/fluids* **74**, 58–67.

Brandt, Laura K. & Nomura, Keiko K. 2010 Characterization of the interactions of two unequal co-rotating vortices. *Journal of Fluid Mechanics* **646**, 233–253.

Chakraborty, P., Balachandar, S. & Adrian, R. J. 2005 On the relationships between local vortex identification schemes. *Journal of Fluid Mechanics* **535**, 189–214.

Chen, Q., Zhong, Q., Qi, M. & Wang, X. 2015 Comparison of vortex identification criteria for planar velocity fields in wall turbulence. *Physics of Fluids* **27** (8), 085101.

Deem, G.S. & Zabusky, N.J. 1978 Vortex waves - stationary v states, interactions, recurrence, and breaking. *Physical Review Letters* **40** (13), 859–862.

Dritschel, D. G. 1985 The stability and energetics of corotating uniform vortices. *Journal of Fluid Mechanics* **157**, 95.

Dritschel, D. G. 1986 Contour surgery: A topological reconnection scheme for extended integrations using contour dynamics. *Journal of Computational Physics* **77** (77), 240–266.

Dritschel, D. G. 1995 A general theory for two-dimensional vortex interactions. *Journal of Fluid Mechanics* **293**, 269.

Dritschel, D. G. & Waugh, D. W. 1992 Quantification of the inelastic interaction of unequal vortices in 2-dimensional vortex dynamics. *Physics of Fluids A-fluid Dynamics* **4** (8), 1737–1744.

E, W. & Liu, J.-G. 1996*a* Finite difference schemes for incompressible flows in vorticity formulations. *ESIAM: Proceedings* **1**, 181–195.

E, W. & Liu, J.-G. 1996*b* Vorticity boundary conditions and related issues for finite difference schemes. *J. Comp. Phys.* **124**, 368–382.

Elsas, J. H. & Moriconi, L. 2017 Vortex identification from local properties of the vorticity field. *Physics of Fluids* **29** (1), 015101.

Folz, P. J.R. & Nomura, K. K. 2017 A quantitative assessment of viscous asymmetric vortex pair interactions. *Journal of Fluid Mechanics* **829**, 1–30.

Gallay, T. 2011 Interaction of vortices in weakly viscous planar flows. *Archive for Rational Mechanics and Analysis* **200** (2), 445–490.

Gallay, T. & Wayne, C. E. 2005 Global stability of vortex solutions of the two-dimensional navier-stokes equation. *Communications in Mathematical Physics* **255** (1), 97–129.

Hansen, J. S. 2011 *GNU Octave - Beginner's Guide*. London: Packt publishing.

Hunt, J. C. R, Wray, A. A. & Moin, P. 1988 Eddies, streams, and convergence zones in turbulent flows. Tech. Rep. CTR-S88. Center for Turbulence Research, Stanford University.

Jalali, M. M. & Dritschel, D. G. 2018 The interaction of two asymmetric quasi-geostrophic vortex patches. *Geophysical and Astrophysical Fluid Dynamics* **112** (6), 375–401.

Jalali, M. M. & Dritschel, D. G. 2020 Stability and evolution of two opposite-signed quasi-geostrophic shallow-water vortex patches. *Geophysical and Astrophysical Fluid Dynamics* **114** (4-5), 561–587.

Jing, F., Kanso, E. & Newton, P. K. 2010 Viscous evolution of point vortex equilibria: The collinear state. *Physics of Fluids* **22** (12), 123102.

Jing, F., Kanso, E. & Newton, P. K. 2012 Insights into symmetric and asymmetric vortex mergers using the core growth model. *Physics of Fluids* **24** (7), 073101.

Kim, S. C. & Sohn, S. I. 2012 Interactions of three viscous point vortices. *Journal of Physics A: Mathematical and Theoretical* **45** (45), 455501.

Leweke, T., Le Dizès, S. & Williamson, C. H.K. 2016 Dynamics and instabilities of vortex pairs. *Annual Review of Fluid Mechanics* **48** (1), 507–541.

Melander, M. V., Zabusky, N. J. & McWilliams, J. C. 1988 Symmetric vortex merger in two dimensions: causes and conditions. *Journal of Fluid Mechanics* **195**, 303–340.

Meunier, P., Ehrenstein, U., Leweke, T. & Rossi, M. 2002 A merging criterion for two-dimensional co-rotating vortices. *Physics of Fluids* **14** (8), 2757–2766.

Nielsen, A. R., Heil, M., Andersen, M. & Brøns, M. 2019 Bifurcation theory for vortices with application to boundary layer eruption. *Journal of Fluid Mechanics* **865**, 831–849.

Overman, E. A. & Zabusky, N. J. 1982 Evolution and merger of isolated vortex structures. *Physics of Fluids* **25** (8), 1297–1305, 1297–1305.

Rutter, J.W. 2000 *Geometry of Curves*. Taylor & Francis.

Saffman, P.G. 1992 *Vortex dynamics*. Cambridge University Press,.

Trieling, R. R., Velasco Fuentes, O. U. & van Heijst, G. J.F. 2005 Interaction of two unequal corotating vortices. *Physics of Fluids* **17** (8), 087103.

Zhang, Y., Liu, K., Xian, H. & Du, X. 2018 A review of methods for vortex identification in hydroturbines. *Renewable and Sustainable Energy Reviews* **81**, 1269–1285.

Chapter 5

Topological bifurcations in the transition from 2S to P+S mode in the wake behind an oscillating cylinder

5.1 Introduction

In the paper presented in this chapter, we revisit the two-dimensional flow past an oscillating cylinder. To the best our knowledge, we are the first to analyse this classical fluid mechanical problem with an approach from topological fluid dynamics. Instead of analysing the flow with the theory we have developed for the Q-criterion in our first two papers, we study the qualitative changes in the vorticity topology as described in section 2.2.2. We have chosen this approach because it previously has been used in a comprehensive study of the flow past the stationary cylinder [27].

In general, the flow past an oscillating object has been the subject of an extensive amount of research. The research has mainly been motivated by the practical problem of vortex-induced vibrations (VIV). Vortex-induced vibrations occur as

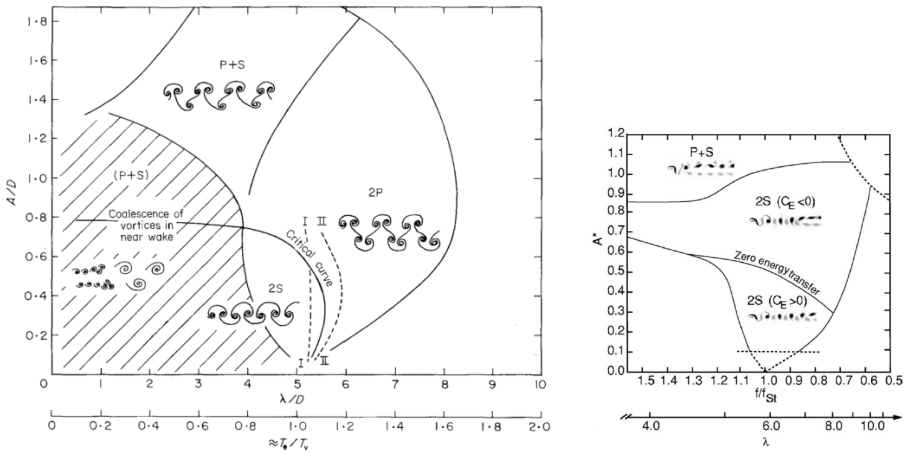

(a) (b)

Figure 5.1: A non-dimensionalised frequency-amplitude map of the vortex synchronisation patterns from two previous studies. (a) the experimental results from Williamson and Roshko (1988) where a cylinder is towed sinusoidally in a water tank at $300 < \mathrm{Re} < 1000$ [58], and (b) the numerical results from Leontini *et al.* (2006) were two-dimensional simulations where conducted at $\mathrm{Re} = 100$ [36].

a result of the time-dependent forces associated with the formation of a wake of vortices behind a so-called bluff body. VIV are relevant to a wide range of applications, including the construction of deepwater risers for extraction of ocean oil [60], the design of wind turbine blades [28], and the optimisation of energy harvesting from vibrating cables [2]. See Williamson and Govardhan (2004) for a comprehensive review of VIV [59]

The flow past a circular cylinder is considered a basic case for flows with more complex geometries, and it contributes to the understanding of vortex-induced vibrations in general bluff bodies. The VIV phenomenon is a fascinating feedback between body motion and vortex motion. Previous studies has emphasised how forced cylinder oscillations can be important in understanding and predicting VIV, see for example [43]. With this approach, the cylinder moves with a prescribed frequency f and amplitude A in a flow with a specified inflow velocity U. Although much of the underlying motivation for forced oscillation studies is related to vortex-induced vibrations, there is a extensive amount of research that focuses solely on the forced oscillations and the resulting wake structure. Williamson and Roshko (1988) conducted an extensive experimental study of the wake structure behind a cylinder over a large range of frequency

and amplitude values [58]. A similar two-dimensional computational study was conducted by Leontini *et al.* (2006) [36]. Some main results of the two studies by are summarised in figure 5.1 showing two frequency-amplitude maps of the observed wake patterns. In both diagrams they use a symbolic code of letters and numbers to describe vortex patterns such as P+S, 2S, and 2P, where S denote a single vortex, and P denote a pair of counter-rotating vortices.

It is common to the two studies that the wake mode is determined only by visual inspection. It is therefore not clearly defined when a vortex is actually present in the computed vorticity field or in the flow visualisation using aluminium particles. An accurate quantification of the topology, including a vortex definition, is required to analyse the flow with a topological fluid dynamics approach. In the paper presented in the following section, we focus on the primary synchroination region where the flow is periodic and the cylinder oscillates with a frequency that is similar to its Strouhal frequency f_{St}. At four different frequency values we give a complete topological description of the transition from 2S to P+S mode in a two-dimensional flow with Re = 100. This is done by keeping track of the vorticity extrema and monitoring cusp bifurcations in the vorticity field during a complete oscillation cycle. This process is repeated for simulations where the amplitude is varied. During our studies, we found a bistable region where different initial conditions resulted in two different types of wake pattern for the exact same parameter values. This bistable region turned out to be completely consistent with results of a very recent paper by Matharu *et al.* (2021) [39]. They compute the time periodic solutions with a space-time discretisation and show that the break in symmetry is due to a subcritical pitchfork bifurcation of the Navier-Stokes equations. It is the fact that the bifurcation is subcritical that causes the bistable region where multiple solutions to occur. Our research has been conducted simultaneously with the research presented by Matharu *et al.* (2021). We have therefore decided to write the following paper as a natural continuation of their findings. In the paper, we describe how the symmetry-breaking pitchfork bifurcation identified Matharu *et al.*(2021) is important in the topological transition from 2S to P+S mode, but it cannot explain all the structural changes we observe. Furthermore, we argue that we need to extend the usual symbolic coding of wake patterns to be able to describe the vortex structure accurately but also to understand the topological changes in the transition.

5.2 Paper III

The paper in this section is an unpublished manuscript which will be submitted for publication after minor revisions.

Topological bifurcations in the transition from 2S to P+S mode in the wake behind an oscillating cylinder

Anne R. Nielsen[1], Puneet S. Matharu[2] and Morten Brøns[1]

[1]Department of Applied Mathematics and Computer Science, Technical University of Denmark, 2800 Lyngby, Denmark

[2]School of Mathematics, University of Manchester, Oxford Road, Manchester M13 9PL, UK

Abstract

We explore the two-dimensional flow past a cylinder undergoing forced transversal oscillations with the aim of elucidating the topology of the wake under variation of the amplitude. In particular, we study the change from two single vortices (2S mode) to a pair and a single vortex (P+S mode) being shed per period. Matharu et al. (J. Fluid Mech. 918 (2021), A21) showed that a dynamical symmetry-breaking pitchfork bifurcation occurs in this transition. We show that in addition to this bifurcation a number of topological bifurcations in the vorticity field occur, both on the (anti-)symmetric 2S branch and the asymmetric P+S branch. Hence, the transition is a process taking place over an interval of forcing amplitudes rather than a single bifurcation event. The topological bifurcations are cusp bifurcations where an extremum of vorticity is created or destroyed. To describe the effect of the topological bifurcations we introduce an extended symbolic classification of the wake modes to account for the spatial variations of the vortex patterns that occur in the transition process. We identify four values of the amplitude that define critical stages in the transition, and obtain a complete qualitative picture of the transition from 2S to P+S mode.

1. Introduction

In the analysis of any fluid mechanical problem it is a natural starting point to make it clear what parameters the problem depends on. Under variation of these external parameters, a flow may undergo some changes which can be understood using bifurcation theory. A bifurcation occurs when a smooth change in the parameter values causes a sudden qualitative or topological change in a dynamical system. In this paper, we draw our attention to the classical fluid mechanical problem of the flow past a circular cylinder undergoing forced oscillations. The problem is characterised by three non-dimensional parameters: the amplitude, A, the wavelength, λ and the Reynolds number, Re. The problem is considered a basic case for bluff bodies with more complex geometries, and it contributes to the understanding of vortex-induced oscillations. In a landmark and much-cited paper Williamson & Roshko (1988) experimentally studied the forced transverse cylinder problem. Their paper was the first to provide a comprehensive study of the differnet flow regimes that occur when varying the wavelength λ and the amplitude A of the cylinder oscillations. They identified several vortex shedding patterns more complex than the well-known von Kármán vortex street behind a stationary cylinder. In later studies, these complicated wake patterns have become known as exotic wakes (Aref *et al.* 2006; Ponta & Aref 2006). Williamson & Roshko (1988) introduced a terminology to

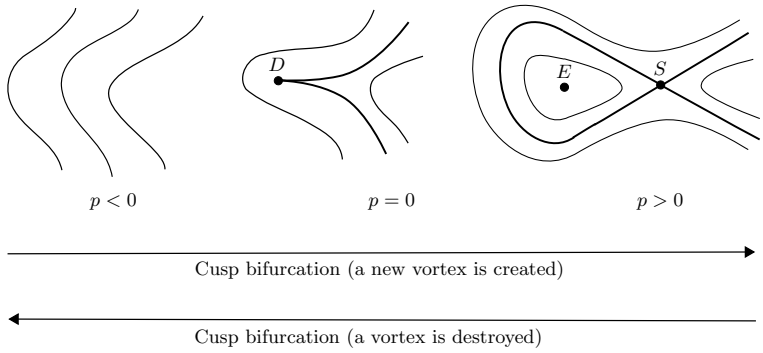

Figure 1: Illustration of the vorticity topology during a cusp bifurcation. The bifurcation parameter p is assumed to take the value zero at the bifurcation point. As p increases, the level curves of the vorticity deform to create an ordinary cusp singularity at the degenerate critical point (D). When p increases further a saddle (S) and an extremum (E) emerge which result in the formation of a vortex.

characterise the vortex pattern in these exotic wakes. They use a symbolic code of letters and numbers to describe vortex patterns such as P+S, 2S, and 2P, where S denotes a single vortex, and P denote a pair of vortices of opposite signs. A pattern such as P+S is one where a pair of vortices and a single vortex are shed in each oscillation cycle. Adopting this natation, the von Kármán vortex street is referred to as a 2S wake. In §4 we argue that an extended classification is needed to give a complete description of the vortex structure in the wake and to understand the topological changes that leads to a change in the wake pattern.

The 2S wake preserves a spatio-temporal Z_2 symmetry Blackburn *et al.* (2005), which means that if the flow is evolved forward in time by half a period, and is reflected spatially about the wake centerline, then the original wake pattern is recovered. In terms of the vorticity field, it means that

$$\omega(x, y, t) = -\omega(x, -y, t + 1/2), \tag{1.1}$$

when the period of cylinder oscillations is normalised to one. On the contrary, it is clear that a P+S wake pattern cannot satisfy the same (anti-)symmetry condition as it alternates between a single vortex or a pair of vortices being shed in every half period. In a very recent paper by Matharu *et al.* (2021) the two-dimensional flow past a transversely oscillating cylinder is revisited. They consider the fundamental lock-in region where the cylinder oscillates with exactly the Strouhal frequency of the cylinder. With a space-time approach they were able to show that the loss of symmetry is due to a subcritical pitchfork bifurcation. In the present paper, we re-examine the two-dimensional flow around the oscillating cylinder with the aim of elucidating the topological changes of the flow field that occur in the transition from 2S to P+S mode. In order to be able to describe the topological changes, we need a clear definition of the topological structure of a given wake. Here, we analyse the topology of the flow field in terms of the vorticity field ω. Since we consider a two-dimensional flow, ω is a scalar field whose topology is described by the level curves and the critical points at which $\partial_x\omega = \partial_y\omega = 0$. The type of a critical

point is determined by the determinant of the Hessian matrix

$$|\boldsymbol{H}^{\omega}| = \partial_{xx}\omega\partial_{yy}\omega - (\partial_{xy}\omega)^2. \tag{1.2}$$

If $|\boldsymbol{H}^{\omega}| > 0$ the critical point is an extremum point and if $|\boldsymbol{H}^{\omega}| < 0$ it is a saddle point. An extremum point in the vorticity field is encircled by closed level curves, and such a region is often identified as a vortex. In this study we choose a vortex criterion where the existence of an extremum of vorticity is a so-called feature point for a vortex (Kasten *et al.* 2016). Extremum points and saddle points are both robust, which means that they persist as they are advected with the flow; see Brøns & Bisgaard (2010) for a derivation of their equations of motion. To locate any topological changes of the vorticity field we must therefore locate the degenerate critical points where $|\boldsymbol{H}^{\omega}| = 0$. Under generic assumptions on higher-order derivatives of ω it can be shown (Brøns 2007) that the simplest possible change in the topology is a cusp bifurcation (also known as a saddle-centre bifurcation). The level curves and the critical points of the vorticity field during a cusp bifurcation is illustrated in figure 1. The bifurcation parameter named p could be any parameter on which the problem depends. In our case the cusp bifurcation could occur as a result of variations in either A, λ or Re. As we shall see, the symmetry-breaking subcritical pitchfork bifurcation cannot itself explain all the topological changes we observe in the transition from 2S to P+S mode. It is therefore necessary to emphasise that bifurcations can occur at two different levels in fluid dynamical problems: at a dynamical level or at a topological level.

At a dynamical level, we consider the Navier-Stokes equations as a dynamical system and the bifurcations occur in an infinite-dimensional function space of velocity fields. In this case a fixed point corresponds to a steady flow and a limit cycle to a periodic flow. A classical example of a dynamical bifurcation is the supercritical Hopf bifurcation that occur when the steady flow past a stationary cylinder loses its stability to a time-periodic solution at $Re \approx 46$ (see, e.g. Dusek *et al.* (1994); Noack & Eckelmann (1994)). At a topological level, we consider a family of flow fields that are already available from solving Navier-Stokes equations at different parameter values. Bifurcations at a topological level are not associated with any loss of stability, but result in changes of the topology of the streamlines or the vorticity level curves in the physical space. An example of a topological bifurcation is the creation of the two symmetric recirculation zones in the flow past a stationary cylinder when $Re \approx 5$ (see, e.g. Brøns *et al.* (2007)). Bifurcations can occur at both levels, but in general they are not related. Heil *et al.* (2017) show that the formation of the famous Kármán-vortex street is a result of both types of bifurcations that occur at two distinct values of Reynolds numbers. As mentioned above the transition from a steady to a time-periodic flow is a dynamical bifurcation, however, it turns out that the transition of the shear layer into individual vortices is a topological bifurcation of the vorticity field.

The symmetry-breaking subcritical pitchfork bifurcation that occur in the transition from 2S to P+S mode is another example of a dynamical bifurcation. In §5 we prove that in this specific problem the existence of a dynamical bifurcation will under certain conditions lead to a particular type of topological bifurcation. By monitoring the structural changes of the vorticity field we show that the transition is a result of a sequence of topological bifurcations where some of them occur while the wake remains (anti-)symmetrical.

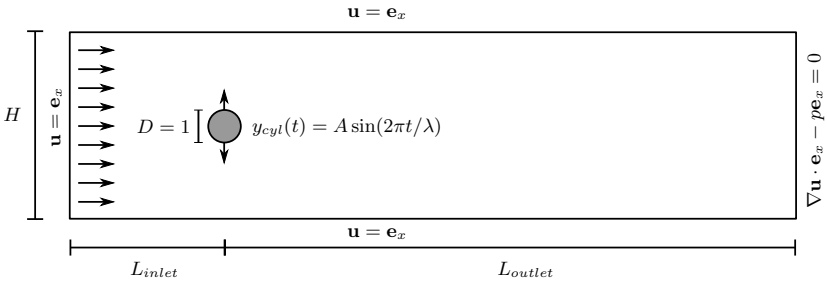

Figure 2: Sketch of the problem setup and the boundary conditions, all expressed in non-dimensional variables. The setup is described by a Cartesian coordinate system where the origin is located at the centre of the cylinder at $t = 0$.

2. Problem setup

We study the two-dimensional flow past a transversely oscillating cylinder in a finite channel. The cylinder is prescribed to move at particular values of frequency f and amplitude A for a specified inflow velocity U. Instead of the frequency the wavelength $\lambda = U/f$ as a equivalent parameter. The wavelength correspond to the length of sine wave trajectory along which the cylinder travels relative to the fluid. Figure 2 shows a sketch of the setup in the frame moving with the horizontal velocity of the cylinder, U. We non-dimensionalise the velocity field $\mathbf{u}$ by rescaling with U. All lengths including the amplitude A and the wavelength λ are non-dimensionalised on the diameter of the cylinder, D. The pressure p is scaled on the associated viscous scale, $\mu U/D$, where μ is the dynamic viscosity of the fluid, and time is scaled on the advective timescale, D/U. The flow (in the moving frame of reference) is then governed by the non-dimensional Navier-Stokes equations

$$Re\left(\frac{\partial \mathbf{u}}{\partial t} + (\mathbf{u}\cdot\nabla)\mathbf{u}\right) = -\nabla p + \nabla^2\mathbf{u} \quad \text{and} \quad \nabla\cdot\mathbf{u} = 0, \tag{2.1}$$

where the Reynolds number is $Re = \rho UD/\mu$, with ρ being the density of the fluid. In the moving frame of reference we use a Cartesian coordinate system, in which the center of the cylinder is located at

$$x_{cyl}(t) = 0, \quad y_{cyl}(t) = A\sin(2\pi t/\lambda). \tag{2.2}$$

On the surface of the moving cylinder we impose the no-slip condition

$$u = 0, \quad v = (2\pi A/\lambda)\cos(2\pi t/\lambda). \tag{2.3}$$

We also impose the boundary conditions

$$u = 1, \quad v = 0, \quad \text{at } x = -L_{inlet} \text{ and at } y = \pm H/2, \tag{2.4}$$

corresponding to a uniform inflow and a no-slip condition relative to the moving channel walls. Furthermore we allow the outlet to remain (pseudo-)traction free i.e.

$$\begin{pmatrix} -p + \partial u/\partial x \\ \partial v/\partial x \end{pmatrix} = \begin{pmatrix} 0 \\ 0 \end{pmatrix} \quad \text{at } x = L_{outlet}. \tag{2.5}$$

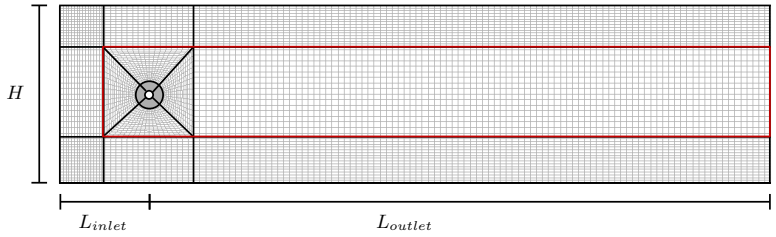

Figure 3: Illustration of the mesh we have used. The thicker lines is the base mesh and the thinner lines show the mesh after 4 uniform refinements. In the actual simulations the computational domain was uniformly refined 5 times in the central region marked with a red box but 3 times outside this region.

Throughout our study, we fix the Reynolds number to be 100. With this Reynolds number at the corresponding flow in a physical experiment is two-dimensional (Griffin 1971). We have chosen the exact value of $Re = 100$ to be able to directly compare with the recent study by Matharu *et al.* (2021) and an earlier study by Leontini *et al.* (2006).

Our aim is to find time-periodic solutions of (2.1)-(2.5). For a given solution $\mathbf{u}(x, y, t; A, \lambda)$ the corresponding vorticity field can be computed as

$$\omega(x, y, t; A, \lambda) = \nabla \times \mathbf{u}(x, y, t; A, \lambda). \tag{2.6}$$

To investigate topological bifurcation in the vorticity field, simulations have been performed at four different values of the wavelength: $\lambda = 5.5$, 6.0851, 6.5 and 6.7. The value $\lambda_{st} = 6.0851$ is chosen so that

$$T/T_{st} = \lambda_{st} St = 1, \tag{2.7}$$

where T is the period of the imposed cylinder oscillations and T_{st} is the period at which vortices are shed in the same flow past a stationary cylinder, i.e. the Strouhal period. The Reynolds number of $Re = 100$ corresponds to the Strouhal number $St = 0.164335$ when using the Reynolds-Strouhal number relationship given by Williamson (1988). The wavelength $\lambda_{st} = 6.0851$ therefore corresponds to the cylinder oscillating exactly with the Strouhal frequency f_{st} and the results for $\lambda = \lambda_{st}$ can be compared directly with the studies by Matharu *et al.* (2021). Having selected the value of the two free parameters, Re and λ, we monitor the cusp bifurcations in the vorticity field during a complete oscillation and repeat this as the amplitude is varied.

3. Numerical method

We performed our numerical simulations using the open-source finite-element library `oomph-lib` (Heil & Hazel 2006). The Navier-Stokes equations were spatially discretised with quadrilateral Taylor-Hood elements, within which the velocities and the pressure are represented by quadratic and piecewise linear polynomials, respectively. For the time-integration of the problem we employ the second-order accurate BDF2 scheme with 320 time steps per period of the imposed oscillations. The simulations were performed on a computational domain with dimensions $H = 20$, $L_{inlet} = 10$ and $L_{outlet} = 70$. The

mesh was built from a coarse base mesh and uniformly refined 5 times. The base mesh is shown with thicker lines in figure 3. In the square central box the nodal positions in the mesh are updated for every time step according to the imposed cylinder oscillations. The annular region with unit radius is surrounding the cylinder hole is made rigid so no compression occurs in this part of the mesh as the cylinder oscillates. To reduce the computational cost some of our simulations were performed on a mesh where only the central down stream region and the square central box (marked with a red box in figure 3) were uniformly refined 5 times while the remainder was refined only 3 times. Upon comparison of mesh types we find no qualitative difference in the vorticity topology.

The simulations are initiated by computing the steady solution with a fixed cylinder at $Re = 0$. We use this result as an initial guess to compute the solution for a slightly higher Reynolds number and continue in this manner until we reach $Re = 100$. This solution is used as an initial condition for the oscillating cylinder simulations where the amplitude of the oscillations are gradually increased in the first two periods. The time-periodicity of the solution was assessed by computing the L^2-norm of the change in the velocity components over one period of the cylinder oscillation. We consider the simulations as converged to periodic solutions when the relative change in the L^2-norm of the velocity components drops below 10^{-6}. We have chosen this threshold value by comparing with simulations where the relative change has instead dropped below 10^{-8}. In the cases examined, we observe no topological difference between the two associated vorticity fields, at least not to the level of precision at which we keep track of the cusp bifurcation points. To meet our convergence criterion, we had to run the simulations between 50 and 2000 periods.

To compute the vorticity field and its derivatives we need the derivatives of the velocity field. As the solution between the elements are only required to be continuous, these derivatives might be discontinuous. To compute smooth approximations of the required derivatives we use oomph-lib's derivative recovery techniques (see Heil *et al.* (2017) for details). As mentioned in the introduction we consider an extremum of vorticity as a feature point for a vortex. The extrema (and saddle points) are located as the intersection point between the nullclines $\partial\omega/\partial x = 0$ and $\partial\omega/\partial y = 0$.

4. An extended classification of wakes with topological variations downstream

When characterising a wake pattern, it is common to use the terminology introduced by Williamson & Roshko (1988). However, because their classification method assumes that the entire wake can be classified as a single type of pattern, it is expected that, once formed, all vortices are translated downstream without any change in the topology. In this section, we will argue that a more detailed classification is necessary to be able to describe the vortex structure accurately but also to understand the topological changes in the transition from 2S to P + S. Two snapshots of different vorticity fields are shown in figure 4. The vorticity fields are computed for an oscillating cylinder with the same wavelength but different amplitudes A. The feature points for vortices, i.e. the vorticity extrema, are marked with black dots. For $A = 0.80$, we see that two single vortices are shed in each oscillation cycle, and this structure is preserved when the vortices are advected downstream. Therefore, we classify the wake pattern as a full 2S wake. For a larger amplitude $A = 1.110$ we similarly see a P+S wake pattern that is translated downstream. In these examples the terminology introduced by Williamson & Roshko (1988) is fully sufficient for classifying the wake pattern. However, this is not always the case. Figure 5 shows four snapshots of the vorticity field for $A = 1.085$, a value between

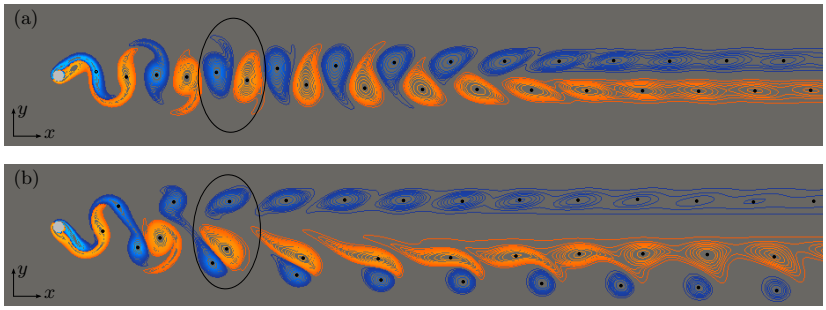

Figure 4: Snapshots of the vorticity field computed for $\lambda = 6.0851$ and (a) $A = 0.80$, (b) $A = 1.110$. All extrema of vorticity are marked with black dots. The black curves encircle a set of vortices that are shed in a single oscillation cycle. Note that part of the computational domain is shown.

the cases in figure 4. From the number of vorticity extrema we conclude that two pairs of vortices are shed during one oscillation cycle, suggesting that vortex shedding pattern looks like a 2P mode in the near wake. One of the vortices in each pair is much weaker than the other, and it quickly disappears. In figure 5 the black curves highlights a set of vortices that are shed during an oscillation cycle. In the first snapshot, the highlighted vortices consist of two pairs of vortices. Figure 5(b) shows the vorticity field in the last time step before one of the highlighted vortices disappears via a cusp bifurcation with a saddle point. Exactly half a period later, a second cusp bifurcation occurs, and the set of highlighted vortices then consists of two single vortices. The snapshot in figure 5(d) shows the last time step before the second cusp bifurcation occurs. Despite the fact that we observe topological bifurcations as the vortices move downstream, the spatio-temporal Z_2 symmetry is preserved throughout the process. Therefore, we conclude that the bifurcations do not occur as a result of symmetry breaking.

In order to describe the topological variations of the vorticity field downstream, we introduce an extended classification where we write down the observed types of wake patterns and indicate with a superscript $n \in \mathbb{N}$ how long the pattern persists. If the pattern exists for more than $n-1$ periods but less than n periods, we designate the superscript n. In the example in figure 5(b) the vortices that originate from the same cycle are grouped together with dashed and dotted lines. A dashed line indicates that the group consists of two pairs of vortices while a dotted line indicates that the group consists of two single vortices. We observe that three groups with a 2P pattern are present in the vorticity field just before the first of the two weaker vortices disappears. Hence, we conclude that the vortices in a 2P group move downstream for between two and three periods before any topological bifurcation occur. The wake in figure 5 therefore has a $(2P)^3(2S)^\infty$ vortex pattern. Here ∞ denotes that no further bifurcations are observed. Also, we do not address the changes in the wake structure that occur far downstream. It is well-known the primary vortex street breaks down into a nearly parallel shear flow of Gaussian profile at a certain downstream distance, before a secondary vortex street of larger scale may appear further downstream (Karasudani & Funakoshi (1994)). Note, that in the extended classification, the standard 2S and P+S wakes are denoted $(2S)^\infty$ and $(P+S)^\infty$, respectively.

Figure 6 shows a snapshot of a vorticity field computed for an oscillating cylinder with

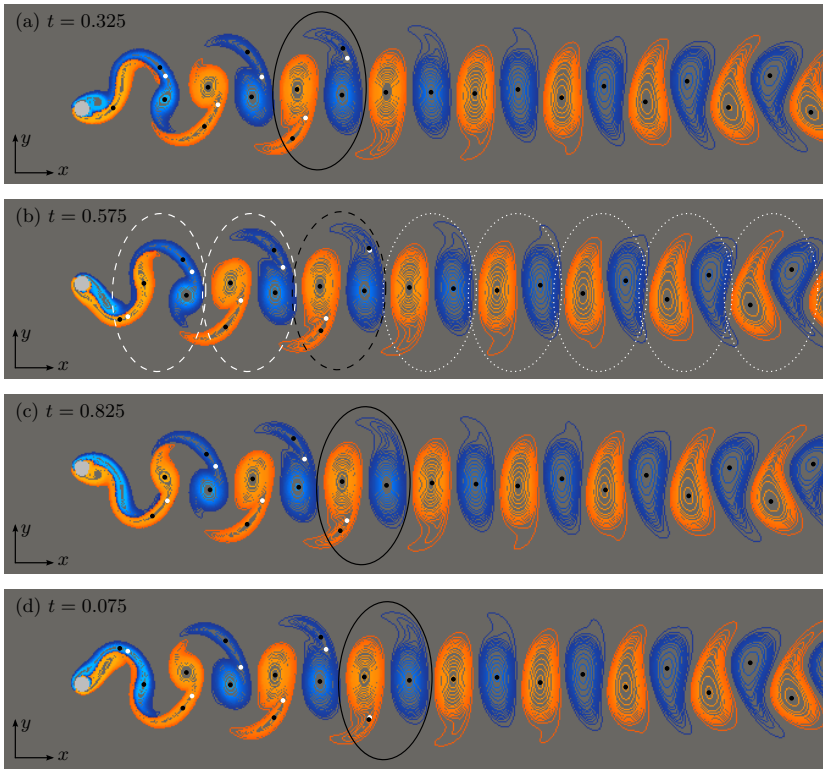

Figure 5: Four snapshots of a vorticity field computed for $\lambda = 6.0851$ and $A = 1.085$. The noted times indicate when the snapshots were taken during a period of cylinder oscillations that is normalized to one. All extrema of vorticity are marked with black dots and saddle points are marked with white dots. The black curves highlight how the vortices that are shed in one oscillation cycle move downstream during a period of oscillation. The vortices that originate from the same cycle are grouped together in (b). A dashed line indicates that the group consists of two pairs of vortices while a dotted line indicates that the group consists of two single vortices. Note that part of the computational domain is shown.

$\lambda = 6.7$ and $A = 1.140$. This vorticity field is an example of another wake pattern with topological variations downstream. The snapshot is taken at the last time step before the weaker vortex in the lower pair disappears in a cusp bifurcation. Since this is the only topological bifurcation that occur, the wake is classified as mode $(2P)^2(P+S)^\infty$. One could argue that the wake patterns in figure 5 and figure 6 are really just 2S and P+S modes, and the extra vortices that our classification detect in the shear layers have no significant impact. But as we will see in §5, it is precisely these vortices that become important when describing the topological development from a 2S to a P+S wake.

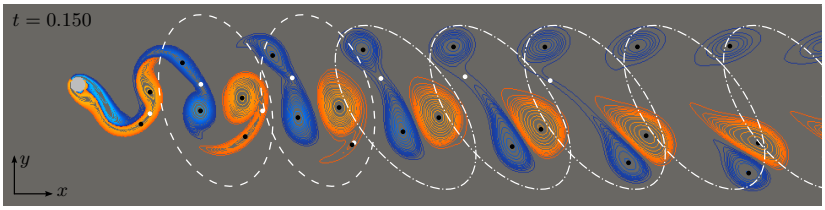

Figure 6: A snapshot of a vorticity field computed for $\lambda = 6.7$ and $A = 1.140$. All extrema of vorticity are marked with black dots and saddle points are marked with white dots. The snapshot is taken at the last time step before the cusp bifurcation occur. The vortices that originate from the same cycle are grouped together. A dashed line indicates that the group consists of two pairs of vortices while a dash-dotted line indicates that the group consists of a pair of and a single vortex. Only part of the computational domain is shown.

5. Topological bifurcations of the vorticity field at the symmetry-breaking pitchfork bifurcation point

As mentioned in the introduction, a very recent paper by Matharu *et al.* (2021) shows that the break in symmetry that occur in the transition from 2S to P+S mode is due to a dynamical bifurcation, namely a subcritical pitchfork bifurcation. As described, the 2S wake pattern preserves a spatio-temporal (anti-)symmetry condtion, where the vorticity field satisfies that

$$\omega(x, y, t) = -\omega(x, -y, t + 1/2). \tag{5.1}$$

Matharu *et al.* (2021) analyse simulations with increasing amplitude values and evaluate whether the (anti-)symmetry condition is satisfied by measuring the difference between $\omega(x, y, t)$ and $-\omega(x, -y, t + 1/2)$ as

$$\varepsilon = \frac{1}{2}\|\omega(x, y, t) + \omega(x, -y, t + 1/2)\|. \tag{5.2}$$

A sketch of their resulting bifurcation diagram is shown in figure 7. At $A = A_2$, a subcritical pitchfork bifurcation that occurs, creating two branches of asymmetric periodic solutions ω^+, ω^-. Each of these subsequently gain stability in fold bifurcations at $A = A_1$. The stable branch associated with $\varepsilon = 0$ corresponds to time periodic solutions where the wake pattern satisfies the (anti-)symmetry condition (5.1). The 2S wake pattern shown in figure 4(a) is an example of a stable solution that clearly satisfies that $\varepsilon = 0$. At the two outer branches in the pitchfork the (anti-)symmetry condition is broken, meaning that $\varepsilon \neq 0$. However, as the pitchfork is symmetrical, a solution on the positive branch ω^+ has a conjugate solution on the negative branch ω^- satisfying

$$\omega^+(x, y, t) = -\omega^-(x, -y, t + 1/2) \tag{5.3}$$

The P+S wake pattern shown in figure 4(b) is an example of a wake pattern on the stable part of the outer branch of the pitchfork. We notice that the physical setup is completely symmetrical around the centerline and there is nothing to indicate why the pair of vortices appear below the centerline. Hence, there must exist a conjugate time-periodic solution where the pair of vortices are instead shed above the centerline. The history of the cylinder motion determines entirely which of the two conjugate solutions

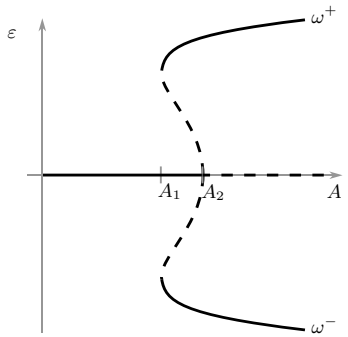

Figure 7: A sketch of the bifurcation diagram illustrating the subcritical pitchfork bifurcation at $A = A_2$ and secondary fold bifurcations at $A = A_1$. In the specific case where the cylinder oscillates with $\lambda = 6.0851$, Matharu *et al.* (2021) determined the bifurcation parameter values to be $A_1 \approx 1.0680$ and $A_2 \approx 1.0855$.

a simulation converges to. By reversing the initial motion of the cylinder, we obtain the solution belonging to the opposite branch in the bifurcation diagram. These conjugate solutions correspond to the two solutions on the outer branch of the pitchfork satisfying the condition in (5.3).

In this section, we will analyse the topological bifurcation of the vorticity field that occurs as a direct result of the dynamical bifurcation. As a starting point for the analysis, we introduce a parameter σ moving along the outer branches in the bifurcation diagram as illustrated in figure 8(a). For the sake of simplicity we let $\sigma = 0$ correspond to the (anti-)symmetric vorticity field located at the pitchfork bifurcation point. Since the two outer branches correspond to the two conjugate solutions it follows that

$$\omega(x, y, t; \sigma) = -\omega(x, -y, t + 1/2; -\sigma). \tag{5.4}$$

We start by considering a non-degenerate critical point in the vorticity field corresponding to $\sigma = 0$, i.e. a point (x^*, y^*, t^*) satisfying

$$\begin{aligned} \partial_x \omega(x^*, y^*, t^*, 0) &= 0, \\ \partial_y \omega(x^*, y^*, t^*, 0) &= 0, \\ |\boldsymbol{H}^\omega(x^*, y^*, t^*, 0)| &\neq 0. \end{aligned}$$

The implicit function theorem ensures that the critical point is preserved for sufficiently small values of $|\sigma|$. Furthermore, the continuity of $\boldsymbol{H}^\omega$ guarantees that $|\boldsymbol{H}^\omega|$ will not change sign, which means that a critical point identified as a vortex will persist. In the case where all critical points in the (anti-)symmetric vorticity field are non-degenerate, all vortices persist when the symmetry is broken and no topological bifurcations occur as a direct result of the dynamical bifurcation.

If, on the other hand, we assume that the (anti-)symmetric vorticity field at $\sigma = 0$ has topological variations downstream, then there exist a cusp bifurcation point (x^*, y^*, t^*) satisfying

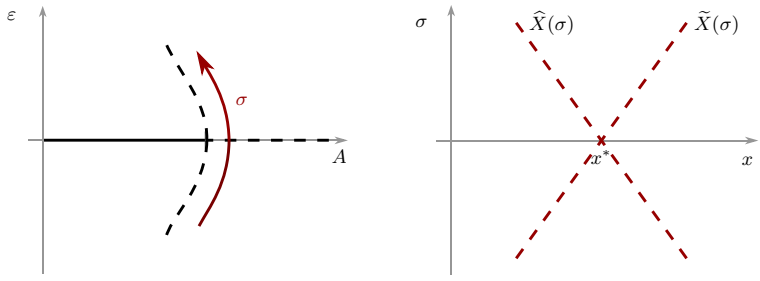

Figure 8: (a) A bifurcation diagram illustrating the subcritical pitchfork bifurcation. The branches of stable and unstable solutions are represented by thick lines and dashed lines, respectively. (b) Thwe bifurcation diagram in a neighbourhood of $(x, \sigma) = (x^*, 0)$. Two different cusp bifurcation curves are parameterised by $\widehat{X}$ and $\widetilde{X}$.

$$\begin{aligned}\partial_x\omega(x^*, y^*, t^*, 0) &= 0,\\ \partial_y\omega(x^*, y^*, t^*, 0) &= 0,\\ |\boldsymbol{H}^\omega(x^*, y^*, t^*, 0)| &= 0,\\ \operatorname{tr}(\boldsymbol{H}^\omega(x^*, y^*, t^*, 0)) &\neq 0.\end{aligned}$$

To characterise the topological changes that occur at $\sigma = 0$ we need to assume some regularity at the cusp bifurcation point (x^*, y^*, t^*). First we consider the following Jacobian

$$\boldsymbol{J}_* = \begin{pmatrix} \partial_{xx}\omega & \partial_{xy}\omega & \partial_{xt}\omega \\ \partial_{xy}\omega & \partial_{yy}\omega & \partial_{yt}\omega \\ \partial_x|\boldsymbol{H}^\omega| & \partial_y|\boldsymbol{H}^\omega| & \partial_t|\boldsymbol{H}^\omega| \end{pmatrix}\Bigg|_{(x^*, y^*, t^*, 0)}. \tag{5.5}$$

If the determinant of $\boldsymbol{J}_*$ is non-zero, i.e.

$$\left(-\begin{vmatrix} \partial_{xx}\omega & \partial_{xy}\omega \\ \partial_x|\boldsymbol{H}^\omega| & \partial_y|\boldsymbol{H}^\omega| \end{vmatrix}\partial_{yt}\omega + \begin{vmatrix} \partial_{xy}\omega & \partial_{yy}\omega \\ \partial_x|\boldsymbol{H}^\omega| & \partial_y|\boldsymbol{H}^\omega| \end{vmatrix}\partial_{xt}\omega\right)\Bigg|_{(x^*, y^*, t^*, 0)} \neq 0, \tag{5.6}$$

then we can apply the implicit function theorem. Based on the above assumptions, we will now analyse the structure of the bifurcation curves in a neighbourhood of the pitchfork bifurcation point. From applying the implicit function theorem we conclude that there exist unique local functions $x = \widehat{X}(\sigma), y = \widehat{Y}(\sigma), t = \widehat{T}(\sigma)$ satisfying

$$\widehat{X}(0) = x^*, \quad \widehat{Y}(0) = y^*, \quad \widehat{T}(0) = t^*, \tag{5.7}$$

and

$$\begin{aligned}\partial_x\omega(\widehat{X}(\sigma), \widehat{Y}(\sigma), \widehat{T}(\sigma), \sigma) &= 0,\\ \partial_y\omega(\widehat{X}(\sigma), \widehat{Y}(\sigma), \widehat{T}(\sigma), \sigma) &= 0,\\ |\boldsymbol{H}^\omega(\widehat{X}(\sigma), \widehat{Y}(\sigma), \widehat{T}(\sigma), \sigma)| &= 0.\end{aligned} \tag{5.8}$$

The functions $\widehat{X}$, $\widehat{Y}$ and $\widehat{T}$ give a parametric representation of the bifurcation curve. The shape of the bifurcation curve is given by the derivatives of $\widehat{X}$, $\widehat{Y}$ and $\widehat{T}$ at the bifurcation

point $\sigma = 0$. By implicit differentiating the equations in (5.8) we obtain the following system of equations,

$$\boldsymbol{J}_* \begin{pmatrix} \widehat{X}'(0) \\ \widehat{Y}'(0) \\ \widehat{T}'(0) \end{pmatrix} = \begin{pmatrix} \partial_{x\sigma}\omega(x^*, y^*, t^*, 0) \\ \partial_{y\sigma}\omega(x^*, y^*, t^*, 0) \\ \partial_\sigma |\boldsymbol{H}^\omega(x^*, y^*, t^*, 0)| \end{pmatrix}. \tag{5.9}$$

Since $\boldsymbol{J}_*$ is non-singular the explicit expressions of $\widehat{X}'(0)$, $\widehat{Y}'(0)$ and $\widehat{T}'(0)$ are well-defined as a combination of the elements in the Jacobian and the right-hand side of (5.9). Instead computing the explicit expressions, we consider a second bifurcation point that is a necessary result of the (anti-)symmetry when $\sigma = 0$. From the condition in (5.4) it follows that

$$\begin{aligned} \partial_x\omega(x^*, -y^*, t^* + 1/2, 0) &= -\partial_x\omega(x^*, y^*, t^*, 0) = 0 \\ \partial_y\omega(x^*, -y^*, t^* + 1/2, 0) &= \partial_y\omega(x^*, y^*, t^*, 0) = 0 \\ |\boldsymbol{H}^\omega(x^*, -y^*, t^* + 1/2, 0)| &= |\boldsymbol{H}^\omega(x^*, y^*, t^*, 0)| = 0 \\ \operatorname{tr}(\boldsymbol{H}^\omega(x^*, -y^*, t^* + 1/2, 0)) &= -\operatorname{tr}(\boldsymbol{H}^\omega(x^*, y^*, t^*, 0)) \neq 0. \end{aligned}$$

and

$$\begin{aligned} &\left(-\begin{vmatrix} \partial_{xx}\omega & \partial_{xy}\omega \\ \partial_x|\boldsymbol{H}^\omega| & \partial_y|\boldsymbol{H}^\omega| \end{vmatrix}\partial_{yt}\omega + \begin{vmatrix} \partial_{xy}\omega & \partial_{yy}\omega \\ \partial_x|\boldsymbol{H}^\omega| & \partial_y|\boldsymbol{H}^\omega| \end{vmatrix}\partial_{xt}\omega\right)\Bigg|_{(x^*,-y^*,t^*+1/2,0)} = \\ &\left(-\begin{vmatrix} -\partial_{xx}\omega & \partial_{xy}\omega \\ \partial_x|\boldsymbol{H}^\omega| & -\partial_y|\boldsymbol{H}^\omega| \end{vmatrix}\partial_{yt}\omega + \begin{vmatrix} \partial_{xy}\omega & -\partial_{yy}\omega \\ \partial_x|\boldsymbol{H}^\omega| & -\partial_y|\boldsymbol{H}^\omega| \end{vmatrix}(-\partial_{xt}\omega)\right)\Bigg|_{(x^*,y^*,t^*,0)} = \\ &\left(-\begin{vmatrix} \partial_{xx}\omega & \partial_{xy}\omega \\ \partial_x|\boldsymbol{H}^\omega| & \partial_y|\boldsymbol{H}^\omega| \end{vmatrix}\partial_{yt}\omega + \begin{vmatrix} \partial_{xy}\omega & \partial_{yy}\omega \\ \partial_x|\boldsymbol{H}^\omega| & \partial_y|\boldsymbol{H}^\omega| \end{vmatrix}\partial_{xt}\omega\right)\Bigg|_{(x^*,y^*,t^*,0)} \neq 0. \end{aligned}$$

As expected we can therefore conclude that $(x^*, -y^*, t^* + 1/2)$ is a cusp bifurcation point satisfying all the same conditions as (x^*, y^*, t^*). By an argument completely similar to the above, there exists functions $x = \widetilde{X}(\sigma)$, $y = \widetilde{Y}(\sigma)$ and $t = \widetilde{T}(\sigma)$ that provide a parametric representation of a bifurcation curve through the point $(x, y, t, \sigma) = (x^*, -y^*, t^* + 1/2, 0)$. By implicit differentiation we obtain the following system of equations

$$\begin{pmatrix} \partial_{xx}\omega & \partial_{xy}\omega & \partial_{xt}\omega \\ \partial_{xy}\omega & \partial_{yy}\omega & \partial_{yt}\omega \\ \partial_x|\boldsymbol{H}^\omega| & \partial_y|\boldsymbol{H}^\omega| & \partial_t|\boldsymbol{H}^\omega| \end{pmatrix} \begin{pmatrix} \widetilde{X}'(0) \\ \widetilde{Y}'(0) \\ \widetilde{T}'(0) \end{pmatrix} = \begin{pmatrix} \partial_{x\sigma}\omega \\ \partial_{y\sigma}\omega \\ \partial_\sigma|\boldsymbol{H}^\omega| \end{pmatrix}\Bigg|_{(x^*,-y^*,t^*+1/2,0)}, \tag{5.10}$$

which by the (anti-)symmetry condition (5.4) can be rewritten as,

$$\begin{pmatrix} -\partial_{xx}\omega & \partial_{xy}\omega & -\partial_{xt}\omega \\ \partial_{xy}\omega & -\partial_{yy}\omega & \partial_{yt}\omega \\ \partial_x|\boldsymbol{H}^\omega| & -\partial_y|\boldsymbol{H}^\omega| & \partial_t|\boldsymbol{H}^\omega| \end{pmatrix} \begin{pmatrix} \widetilde{X}'(0) \\ \widetilde{Y}'(0) \\ \widetilde{T}'(0) \end{pmatrix} = \begin{pmatrix} \partial_{x\sigma}\omega \\ -\partial_{y\sigma}\omega \\ -\partial_\sigma|\boldsymbol{H}^\omega| \end{pmatrix}\Bigg|_{(x^*,y^*,t^*,0)}. \tag{5.11}$$

By comparing with the system of equations in (5.9), we note that the sign of some elements in the Jacobian and the right-hand side is the only thing that differs. Hence it is easy to show that the parametric representations of the two bifurcation curves are

related in the following way,

$$\widetilde{X}'(0) = -\widehat{X}'(0),$$
$$\widetilde{Y}'(0) = \widehat{Y}'(0),$$
$$\widetilde{T}'(0) = -\widehat{T}'(0).$$

There are no conditions on the derivatives of ω that make us expect that the explicit expressions of $\widehat{X}'(0)$, $\widehat{Y}'(0)$ and $\widehat{T}'(0)$ are zero. Therefore we assume that this is not the case in general. In figure 8(b) the two parametric representations of the x-coordinates of the bifurcation curves are illustrated in a neighbourhood of $(x, \sigma) = (x^*, 0)$. As shown in the figure, the x-coordinates of the cusp bifurcation points separates as σ is increased (or decreased) from zero. It is therefore only in the (anti-)symmetric vorticity field where the two cusp bifurcations occur at the same distance downstream. As soon as the symmetry is broken, one of the cusp bifurcation points moves upstream and the other moves downstream.

We remind ourselves that Matharu *et al.* (2021) only consider the case where the cylinder oscillates exactly with the Strouhal frequency, i.e. $\lambda = 6.0851$. It is therefore a possibility that the break in symmetry for other frequency values will instead occur as a result of a supercritical pitchfork bifurcation. Although we have chosen to depict a subcritical bifurcation in the sketches within this section, the analysis does not depend on the critically of the bifurcation.

6. Numerical results

With the numerical method described in §3 we perform simulations where the cylinder oscillates with an amplitude in the range $0.8 \leqslant A \leqslant 1.2$ and with one of the four selected wavelengths $\lambda = 5.5$, 6.0851, 6.5 and 6.7. In each simulation we keep track of the vorticity extrema during a complete oscillation cycle, and each time we observe a cusp bifurcation, we write down the coordinate set of the bifurcation point (x^*, y^*, t^*). It is not possible to plot a bifurcation diagram where all three coordinates are depicted as a function of the bifurcation parameter A. Since we are interested in describing the topological variations downstream, the x-coordinates of the bifurcation points are the most meaningful to depict. For each of the four selected wavelength values we perform simulations with more than 30 different amplitude values and we mark the cusp bifurcation points in the (x, A) parameter plane. The constructed bifurcation diagrams are presented in figure 9(c)-(j). From Matharu *et al.* (2021) we know that a bistable region with three stable solutions exists for $\lambda = 6.0851$, however, only two of the solutions are qualitatively different. To resolve both of these solutions, we construct two different bifurcation diagrams for each of the four wavelengths. To construct the diagrams in the left column, we use a solution obtained for $A < A_1$ as initial condition for the solution at a larger A, as illustrated in figure 9(a). The diagrams in the right column are constructed in a similar way but from simulations where the amplitude value is decreased, as illustrated in figure 9(b). In all four cases, the bifurcation diagrams in the left and right columns differ in a small region, implying that a bistable region exists for all the four wavelengths. In other words, the bifurcation remains subcritical. The red lines at A_1 and A_2 mark the lower and upper limits of the bistable regions. In this specific case where the cylinder oscillates with $\lambda = 6.0851$ we found that $A_1 \approx 1.0775$ and $A_2 \approx 1.0925$. These values are comparable to, but not exactly the same as, those determined by Matharu *et al.* (2021), i.e. $A_1 \approx 1.0680$ and $A_2 \approx 1.0855$. The small difference may be due to the difference in the numerical method used and the fact that we use different lengths of the domain. As expected,

each pair of bifurcation diagrams are identical outside the bistable region. When A is increased (or decreased), we recall that the solutions obtained for $A < A_2$ (or $A < A_1$) satisfy the (anti-)symmetry condition (5.1). This implies that two cusp bifurcations occur with exactly half a period in between at the same downstream position at bifurcation points marked in the (x, A) parameter plane.

As illustrated in figure 3 we use a non-uniformly refined mesh in the region close to the cylinder, but our method of computing the derivatives of the vorticity is only accurate on a uniform mesh. Therefore, we can not resolve the cusp bifurcations that occur for $x < 5$ where the vortices are initially created. We only show the region for $x < 40$, as no topological bifurcations are observed beyond that limit.

The four pairs of bifurcation diagrams in figure 9 are qualitatively very similar. We start by considering the case where the cylinder oscillates with exactly the Strouhal frequency, i.e. $\lambda = 6.0851$, and explain in details the corresponding pair of bifurcation diagrams in figure 9(e) and (f). The bifurcation curves and the upper/lower limits of the bistable region separate the (x, A) parameter plane into three different regions. The labels indicate whether a specific part of the wake has a 2S, 2P or a P+S topology. Let us describe the transition we observe for increasing amplitude values, as illustrated in figure 9(e). For amplitude values below the dashed blue line we observe a 2S pattern that persists in the downstream wake and hence we classify the wake mode as $(2S)^\infty$. At the dashed blue line, a degenerate critical point appears (at $x \approx 16$) and immediate disappears. As a consequence of the (anti-)symmetry condition in (5.1) a degenerate critical point also appears half a period later at the same downstream position. For amplitude values above the dashed blue line, we observe two cusp bifurcations every half period, which means that two additional vortices are created and subsequently destroyed in each period. Because these vortices persist for less than a period, we classify the wake pattern as as $(2S)^2(2P)^1(2S)^\infty$. As we increase the amplitude past the dashed blue line, the first cusp bifurcation point moves upstream and eventually out of the domain we consider. This implies that the two extra vortices in the 2P groups are created further upstream and hence they persist longer. When they persist for more than an entire period the local pattern changes from $(2P)^1$ to $(2P)^2$ and when the amplitude increases further it changes again to a $(2P)^3$ pattern. For $A = 1.05$ the extra vortices in the 2P groups are created outside our domain and they move downstream for between two and three periods before they disappear in a cusp bifurcation. We therefore classify the topological structure of the wake as $(2P)^3(2S)^\infty$. At an amplitude of $A = A_2$, we observe a jump from one solution branch to another accompanied by a discontinuous change in the topology to a wake that we classify as $(P+S)^1(2P)^1(P+S)^\infty$. This discontinuity is due to the jump from one solution branch to another. As we increase the amplitude further and reach the dashed green line the two cusp bifurcation points that bound the 2P region merge and disappear. For amplitude values above this dashed green line, we observe a P+S pattern that persists in the downstream wake. Hence we classify the wake mode as $(P+S)^\infty$.

For decreasing amplitude values the transition form $(P+S)^\infty$ to $(2S)^\infty$ is illustrated in figure 9(f). The transition is essentially the reverse of the process described above. The only difference is that the discontinuous change in the topology occurs at $A = A_1$ and hence the $(P+S)^n(2P)^m(P+S)^\infty$ patterns exist only above that value of A. The remaining three pairs of bifurcation diagrams in figure 9 are constructed from simulations where the wavelength is either decreased or increased from $\lambda = 6.0851$. In all four cases we observe similar wake patterns with the same topological transitions. In general, we only observe a $(2S)^\infty$ pattern below the dashed blue lines and we only observe a $(P+S)^\infty$ above the dashed green lines. For amplitude values in the range between these boundaries, an

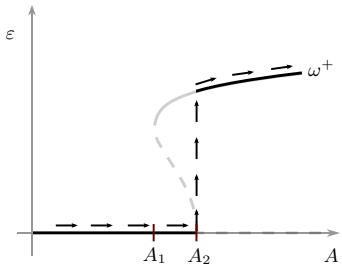

(a) Increasing A.

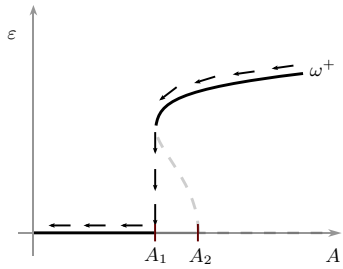

(b) Decreasing A.

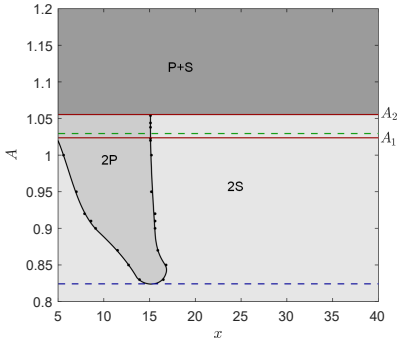

(c) $\lambda = 5.5$, increasing A.

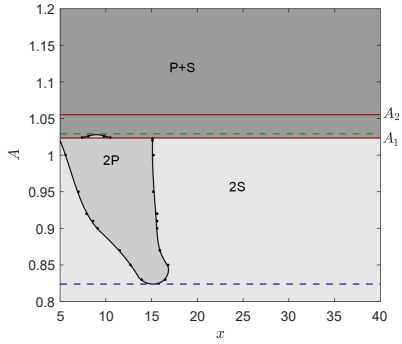

(d) $\lambda = 5.5$, decreasing A.

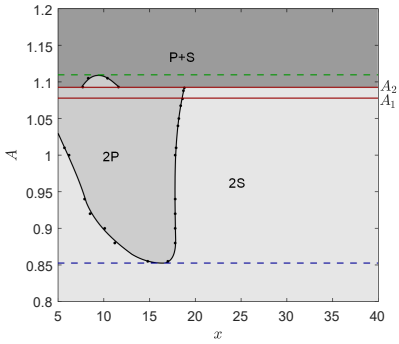

(e) $\lambda = 6.0851$, increasing A.

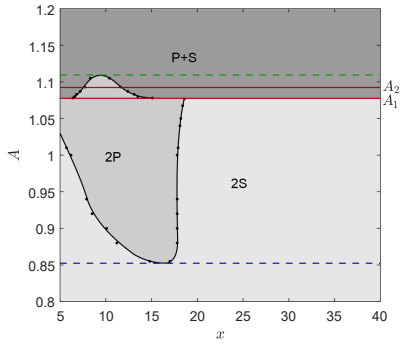

(f) $\lambda = 6.0851$, decreasing A.

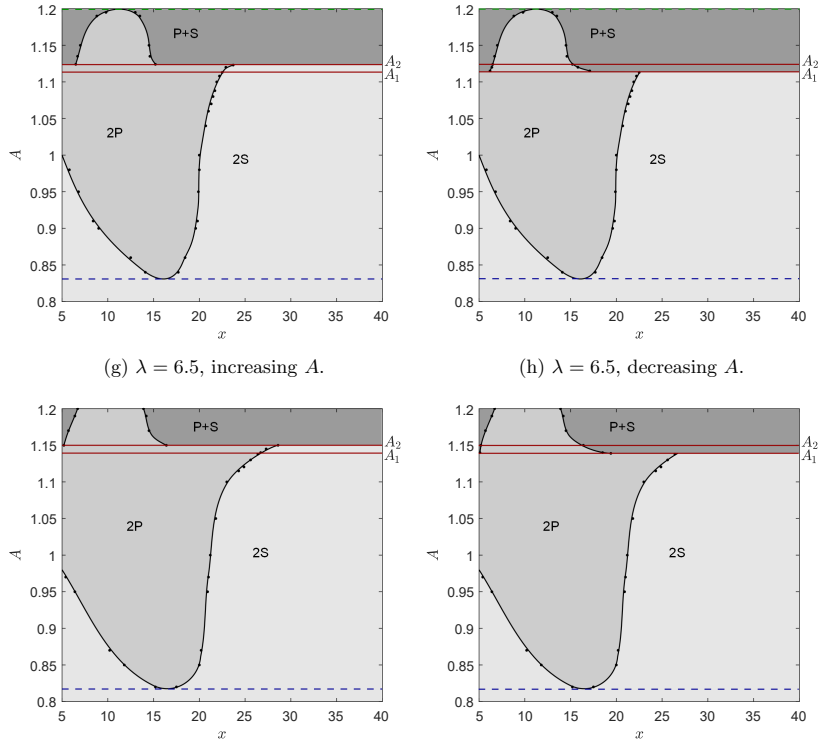

(g) $\lambda = 6.5$, increasing A.

(h) $\lambda = 6.5$, decreasing A.

(i) $\lambda = 6.7$, increasing A.

(j) $\lambda = 6.7$, decreasing A.

Figure 9: (a)-(b) A sketch of the dynamical bifurcation diagram illustrating one of the solution branches in the subcritical pitchfork bifurcation. The solid black lines highlight the section of the solution curve that we explore with the simulations obtained by either increasing or decreasing the amplitude from a previous simulation. (c)-(j) Four pairs of bifurcation diagrams constructed from simulations with different wavelengths. The black dots, connected by solid lines, mark the topological bifurcation points observed in the simulations. The red lines at A_1 and A_2 indicate the upper and lower limits of the bistable region. The dashed blue line indicates the limit below which we observe a $(2S)^{\infty}$ pattern. The dashed green line indicates the limit above which we observe a $(P+S)^{\infty}$ pattern.

alternative description of the wake pattern is required due to the observed topological variations in the downstream wake.

In previous studies, the transition between different wake modes are typically marked with a single critical boundary, indicating that there is a sharp change from one mode to another. Due to the discontinuous jump in the vorticity topology, it is natural that the transition has been interpreted in this way in studies where the overall pattern is determined from visual inspection. In figure 10(a), we show a region of the parameter space explored by Leontini *et al.* (2006). The sharp boundary that the authors used to

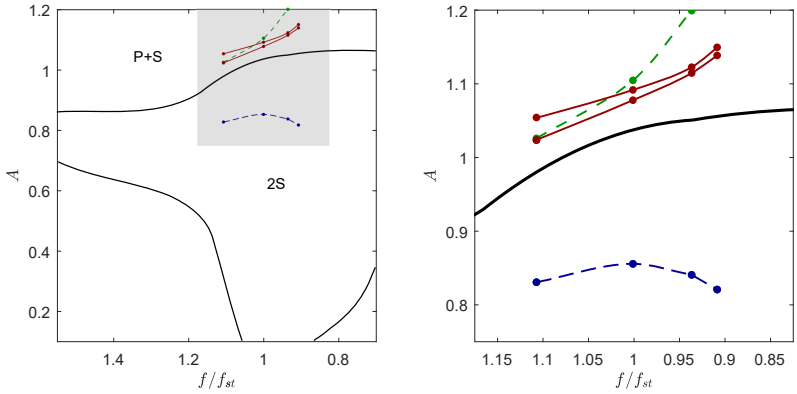

(a) (b)

Figure 10: (a) A region of the parameter space explored by Leontini *et al.* (2006). The solid black lines are the boundaries of the primary synchronization region and the boundary defining the transition from 2S to P+S, as identified by Leontini *et al.* (2006). Four characteristic amplitude values are marked with colors corresponding to the colors in figure 9; the red dots indicate the upper and lower limits of the bistable region, the blue dots indicate the limit below which we observe a $(2S)^\infty$ pattern and the green dots indicate the limit above which we observe a $(P+S)^\infty$ pattern. (b) A close-up of the grey region in (a).

demarcate the transition between the 2S and P+S wake mode is drawn with a solid black line. In our search for a complete topological description of the transition, we have found that four characteristic amplitude values play an important role: the limit below which we observe $(2S)^\infty$, the upper and lower limits of the bistable region and the limit above which we observe $(P+S)^\infty$. Since the results of Leontini *et al.* (2006) also derive from simulations at $\mathrm{Re} = 100$, they should be directly comparable to ours. In figure 10(a) we have marked the four characteristic amplitude values for each of our wavelength values (or equivalently the corresponding frequencies). The colored dots, connected by solid or dashed lines, defines a region of the parameter space in which the transition occur. It is only above and below all these lines that we can classify the pattern as a full P+S or 2S pattern.

Since the symmetry-breaking pitchfork bifurcation at A_2 is subcritical, we do not observe a continuous evolution of the vorticity field in the transition from 2S to P+S. This is because part of the continuous evolution takes place along the unstable solution branch. However, based on the theoretical considerations in §5, we can still give a complete qualitative picture of the topological changes in the transition from 2S to P + S. We introduce a parameter γ that moves from the stable (anti-)symmetric branch onto the unstable outer branch when reaching the pitchfork bifurcation point at $A = A_2$, see figure 11(a). In figure 11(b) we illustrate the (x, γ) parameter plane in the case where $\lambda = 6.0851$. The solutions for $\gamma < \gamma_{A_2}$ and $\gamma > \gamma_{A_1}$ lie on the stable branches and are topologically described by the preceding analysis of the numerical simulations. The bifurcation curves drawn as solid lines in figure 11(b) are therefore identical to those

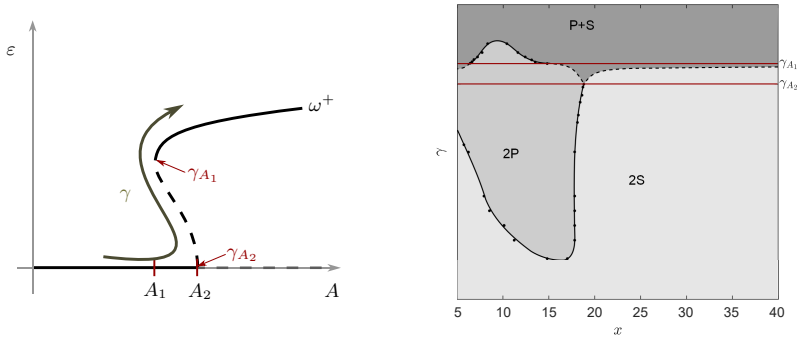

(a) (b)

Figure 11: (a) A sketch of the dynamical bifurcation diagram near $A = A_2$ reparameterised by the parameter γ. (b) A bifurcation diagram in the (x, γ) parameter plane. The black dots, connected by solid lines, mark the bifurcation points observed in the simulations with $\lambda = 6.0851$. The dashed lines in the range $\gamma_{A_2} < \gamma < \gamma_{A_1}$ are examples of how the bifurcation curves could possibly evolve along the unstable solution branch.

shown in figure 9(e) and (f). The time-periodic solutions in the region $\gamma_{A_2} < \gamma < \gamma_{A_1}$ lie on the unstable branch. Based on the result in §5, we know that as soon as the symmetry is broken at $\gamma = \gamma_{A_2}$, one of the cusp bifurcation points moves upstream and the other moves downstream. These points correspond to the two dashed black curves in figure 11(b) that split up at $\gamma = \gamma_{A_2}$. In the time-periodic solutions in the region $\gamma > \gamma_{A_1}$, we only observe a single cusp bifurcation point that corresponds to the destruction of a vortex. Since this point has moved upstream, the second cusp bifurcation must have moved rapidly downstream and disappeared from our domain within the unstable region. The bifurcation curves drawn as dashed lines in figure 11(b) are therefore a qualitatively correct illustration of expected topological changes in the unstable region.

With this extended bifurcation diagram we have complete qualitative picture of the topological changes in the transition from 2S to P+S. A significant part of the transition is invisible since the topological changes take place along the unstable branch. Although the dynamical symmetry-breaking bifurcation identified by Matharu *et al.* (2021) is a key component of the transition, it alone cannot provide the complete topological picture

7. Discussion

We have investigated the topological changes of the vorticity field in the transition from 2S to P+S wake mode. Based on numerical simulations, we have shown that the transition cannot be fully described with a single critical boundary. Instead of a sharp change from one mode to another, we determine a range of amplitude values where the corresponding wake has a mixed pattern with topological variations downstream. We show that the symmetry-breaking pitchfork bifurcation identified by Matharu *et al.* (2021) plays an important role in the transition, but at the same time it does not provide the complete description, as topological changes occur even before this bifurcation point.

In general, the transition can be described as follows: through a continuous evolution of the vorticity field, a 2P-like pattern arises in near wake. The extra two vortices that we detect in the shear layers arise through cusp bifurcations and move downstream for up to three periods before disappearing again in two reverse cusp bifurcations. We prove that the topological role of the pitchfork bifurcation is to relax the condition that these two cusp bifurcations must occur with a temporal spacing of exactly half a period. The breaking of symmetry allows one of the cusp bifurcations to move rapidly downstream, implying that one of the extra vortices persist in the downstream wake. As the second cusp bifurcation moves upstream the 2P-like pattern in the near wake disappears and the wake has a clear P+S structure. Since the symmetry-breaking pitchfork bifurcation is subcritical, a significant part of the continuous evolution of the vorticity field takes place along the unstable solution branch. This part of the evolution is not visible in our simulations, but based on the theoretical considerations in §5 we are still able to give a complete qualitative picture of the continuous transition from 2S to P + S. In all the cases we have examined the bistable region is very narrow. For higher values of λ, for other values of Re, or for other shapes of the oscillating body, the pitchfork bifurcation may change from subcritical to supercritical. In that case, the qualitative description will be the same and the entire continuous evolution will be visible in the simulations.

In all four cases that we have examined, the bistable region is so narrow that the criticality of the pitchfork bifurcation may change form subcritical to supercritical when the wavelength increases further, the Reynolds number changes or the shape of the cylinder changes. If it turns out that there are some parameter values where the transition is supercritical, then the qualitative description will be the same and the entire continuous evolution will be visible in the simulations.

Generally, it is clear that the topological structure of a given wake pattern must depends on the way we identify vortices. In most previous studies, including those of Leontini *et al.* (2006) and Williamson & Roshko (1988), the wake mode is determined simply by visual inspection. It is therefore not clearly defined when a vortex is actually present in a given flow visualisation. It is clear that the topological description of the transition must be inextricably linked to the way we choose to define vortices mathematically, see e.g. Nielsen *et al.* (2021). A mathematical definition of a vortex forms the basis of a topological analysis of how a given vortex pattern arises. In this study we consider extremal points of to vorticity be feature points for vortices and by monitoring the vorticity extrema and saddle points, it is possible to define exactly where in the downstream wake a vortex disappears. In general, a topological approach always requires a global knowledge of the flow field, regardless of which vortex identification method is used. In a recent study, Colvert *et al.* (2018) use a completely different approach where the flow pattern is classified only on the basis of local vorticity measurements. They train a neural network to uncover the salient features of different wake types and aim to distinguish wake types are not readily recognizable by visual inspection.

Acknowledgements. Financial support from Independent Research Fund Denmark, grant no. 6108-00246B, is gratefully acknowledged. We also wish to acknowledge Professor Matthias Heil from University of Manchester who has supported the numerical part of the study and participated in many fruitful discussions.

Declaration of interests. The authors report no conflict of interest.

REFERENCES

Aref, H., Stremler, M. A. & Ponta, F. L. 2006 Exotic vortex wakes-point vortex solutions. *Journal of Fluids and Structures* **22** (6-7), 929–940.

Blackburn, H. M., Marques, F. & Lopez, J. M. 2005 Symmetry breaking of two-dimensional time-periodic wakes. *Journal of Fluid Mechanics* **522**, 395–411.

Brøns, M. 2007 Streamline topology: Patterns in fluid flows and their bifurcations. *Advances in Applied Mechanics* **41**, 1–42.

Brøns, M. & Bisgaard, A. V. 2010 Topology of vortex creation in the cylinder wake. *Theoretical and Computational Fluid Dynamics* **24** (1-4), 299–303.

Brøns, M., Jakobsen, B., Niss, K., Bisgaard, A. & Voigt, L. K. 2007 Streamline topology in the near wake of a circular cylinder at moderate Reynolds numbers. *Journal of Fluid Mechanics* **584**, 23–43.

Colvert, B., Alsalman, M. & Kanso, E. 2018 Classifying vortex wakes using neural networks. *Bioinspiration and Biomimetics* **13** (2), 025003.

Dusek, J., Le Gal, P. & Fraunie, P. 1994 A numerical and theoretical study of the first Hopf bifurcation in a cylinder wake. *Journal of Fluid Mechanics* **264**, 59–80.

Griffin, O. M. 1971 The unsteady wake of an oscillating cylinder at low Reynolds number. *Transactions of the ASME. Series E, Journal of Applied Mechanics* **38** (4), 729–738.

Heil, M. & Hazel, A. L. 2006 oomph-lib - an object-oriented multi-physics finite-element library. *Lecture Notes in Computational Science and Engineering* **53**, 19–49.

Heil, M., Rosso, J., Hazel, A. L. & Brøns, M. 2017 Topological fluid mechanics of the formation of the Kármán-vortex street. *Journal of Fluid Mechanics* **812**, 199–221.

Karasudani, T. & Funakoshi, M. 1994 Evolution of a vortex street in the far wake of a cylinder. *Fluid Dynamics Research* **14** (6), 331–352.

Kasten, J., Reininghaus, J., Hotz, I., Hege, H. C., Noack, B. R., Daviller, G. & Morzyński, M. 2016 Acceleration feature points of unsteady shear flows. *Archives of Mechanics* **68** (1), 55–80.

Leontini, J. S., Stewart, B. E., Thompson, M. C. & Hourigan, K. 2006 Wake state and energy transitions of an oscillating cylinder at low Reynolds number. *Physics of Fluids* **18** (6), 067101.

Matharu, P. S., Hazel, A. L. & Heil, M. 2021 Spatio-temporal symmetry breaking in the flow past an oscillating cylinder. *Journal of Fluid Mechanics* **918**, A42.

Nielsen, A. R., Andersen, M., Hansen, J. S., Brøns, M. & Nielsen, Anne R. 2021 Topological bifurcations of vortex pair interactions. *Journal of Fluid Mechanics* **917** (917), 2100191.

Noack, B.R. & Eckelmann, H. 1994 A global stability analysis of the steady and periodic cylinder wake. *Journal of Fluid Mechanics* **270**, 297–330.

Ponta, F. L. & Aref, H. 2006 Numerical experiments on vortex shedding from an oscillating cylinder. *Journal of Fluids and Structures* **22** (3), 327–344.

Williamson, C.H.K. 1988 Defining a universal and continuous Strouhal-Reynolds number relationship for the laminar vortex shedding of a circular-cylinder. *Physics of Fluids* **31** (10), 2742–2744.

Williamson, C. H. K. & Roshko, A. 1988 Vortex formation in the wake of an oscillating cylinder. *Journal of Fluids and Structures* **2**, 355–381.

Chapter 6

Numerical and experimental comparison of the flow past an oscillating cylinder

The work presented in this chapter was mainly conducted during my external research stay with professor Mark Stremler at the Department of Biomedical Engineering and Mechanics at Virginia Tech. Mark Stremler and his Ph.D student Emad Masroor had prior to my visit developed an experimental setup consisting of a gravity-driven flowing soap film channel. The soap film experiments we present in this chapter were all performed in close collaboration with Emad Masroor. In section 6.1.1 we give an introduction to this experimental setup which is very similar to the setup described in [61]. In section 6.2 we compare some selected soap film experiments with numerical simulations performed at the exact same parameter values.

6.1 Introduction to soap film experiments

When soap is added to water, the solution can form thin membranes, with typical thickness of order $\sim 5\mu$m. If we consider a flow that takes place on a spatial scale L that is much larger than the thickness of the soap film, the system provides a good approximation to a two-dimensional flow in many respects. Based on the assumption on the length scale, one can show that the equations

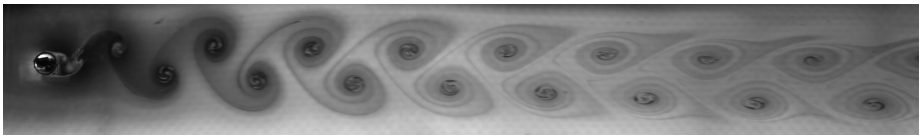

Figure 6.1: Flow visualisation of the wake behind the disk oscillating with amplitude $A = 1$mm and frequency $f = 25.8$Hz.

describing the motion in a flowing soap film are analogous to the two-dimensional incompressible Navier–Stokes equations if the typical flow velocity U is very small compared to the elastic wave velocity v_e (or, equivalently, the elastic Mach number $M_e = U/v_e \ll 1$) [15, 4]. Soap film systems are therefore well established as a useful tool for investigating two-dimensional flows and have been used by several different research groups for analysing the wake structure. Couder & Basdevant showed more than three decades ago that an oscillating cylinder can generate a $2P$ wake in a soap film [16]. Schnipper et al. conducted an extensive parametric analysis of the flow past a flapping foil and observed a variety of wake structures with up to 46 vortices per oscillation period [51]. Yang & Stremler found experimental values of critical spacing between tandem cylinders and showed a good agreement with two-dimensional simulations [62]. Conducting experiments with a flow past an oscillating cylinder in a gravity-driven soap film can be considered as a complement to the three-dimensional experimental work of Williamson & Roshko [58]. The soap film experiments are ideal for comparison with two-dimensional computational studies.

6.1.1 Experimental setup

A schematic overview of the experimental setup is shown in figure 6.2. The soap solution consisting of 1.5% soap mixed in water is continually pumped into the top reservoir to maintain a constant level throughout each experiment. The soap film is developed between two nylon wires (with diameter 1mm) and the volumetric flow rate out of the reservoir is controlled by a valve at the outlet.

In the experiments presented in this chapter, we oscillate a very thin disk instead of an acrylic cylinder which was used in [61]. We choose the disk instead of the cylinder to reduce the size of the meniscus surrounding the cylinder/disk. Since the meniscus is towed with the cylinder it may result in a small region close to the cylinder where the third dimension cannot be neglected. We use a disk with diameter $D = 4$mm and thickness $\sim 75\mu$m which is attached to a metal rod so that the disk penetrated the soap film at a 90° angle. The oscillating

motion is driven by a Scotch-yoke mechanism converting the circular motion of the shaft of a motor to a sinusoidal translation of the disk. The frequency of the oscillation is changed by varying the amount of power provided to the motor and the amplitude of the oscillation is changed by using yokes with different eccentricities.

A monochromatic light source is placed perpendicular to the flowing soap film as illustrated in figure 6.2. The oscillation of the disk causes variations in the thickness of the soap film. Since the monochromatic light is reflected off the top and the bottom surfaces of the soap film an interference patterns is caused by variations in the thickness. The reflected patterns of light are recorded with a high-speed camera positioned near the light source. We document the wake pattern by recording a 10 seconds videos with 200 frames per second. Each frame has an image resolution of 2352×400 pixels. An example of a frame is shown in figure 6.1. It is important to keep in mind that the observed scalar field of light intensity is caused by variations in the thickness of the soap film, it does not measure the flow field itself. An obvious question arises in this context: How is the thickness field correlated to the velocity field? There is no exact theoretical connection between the two fields but Rivera *et al.* [49] try to answer the question by preforming instantaneous experimental measurements of the velocity, vorticity, and thickness fields of turbulent flowing soap films using a modified particle image velocimetry (PIV) technique. They found that the observed thickness and vorticity fields are strongly coupled. In a recent study by Gillissen *et al.* [22] they develop a mathematical method for reconstructing the velocity field from the soap film visualisation within 10% of PIV measurements. Although there is no direct mathematical connection, it is clear that the thickness field must be closely related to the flow field itself. In conclusion, we can trust that a vortex region exists in the two-dimensional flow of the soap film when we observe a region where the thickness of the soap film is significantly increased.

6.1.2 Parameter estimation

As described in chapter 5, the oscillating cylinder problem can be characterised by the following three dimensionless parameters: the normalised oscillation amplitude $A^* = A/D$; the frequency ratio $f^* = f/f_{St}$; and the Reynolds number $Re = UD/\nu$, where ν is the kinematic viscosity of the fluid and U is the background flow speed. In some studies, the wavelength ratio, $\lambda^* = \lambda/D$ is used instead of f^*.

The oscillation amplitude A was determined by measuring the distance from the motor's rotation axis to the center axis of the disk. In the experimental setup we

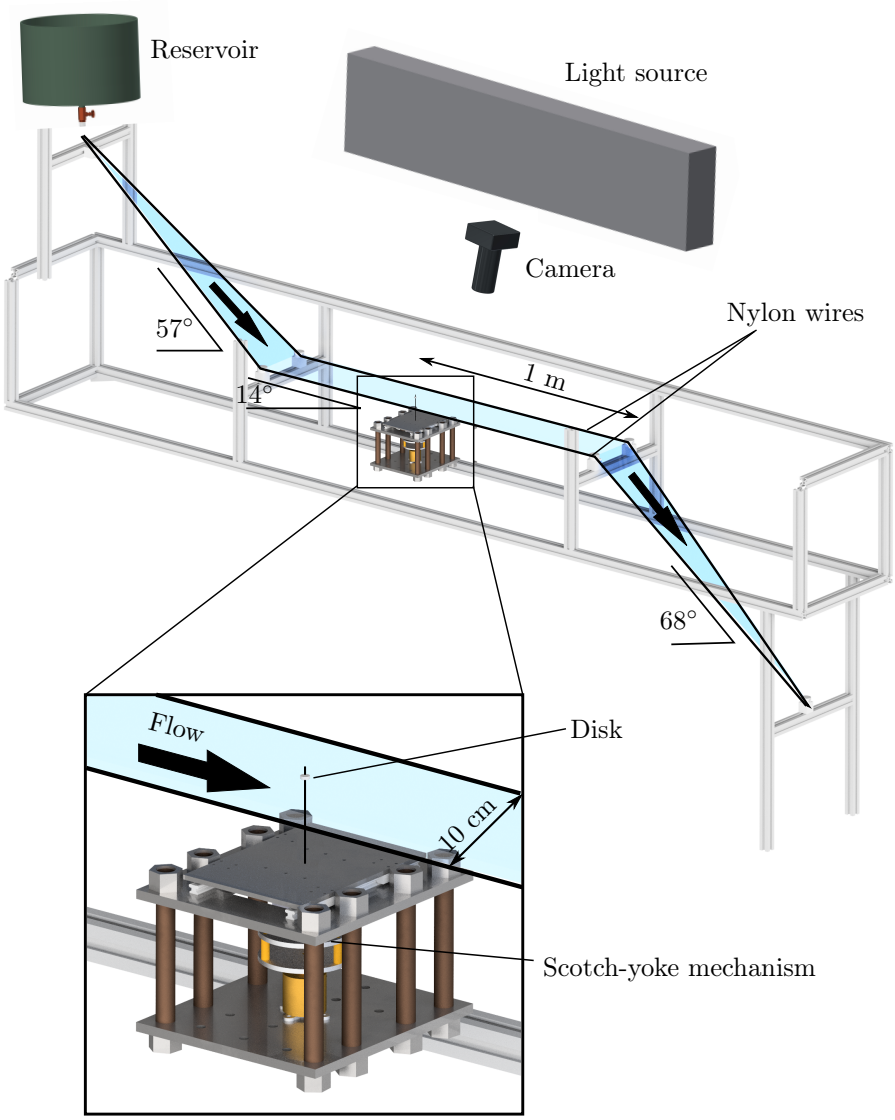

Figure 6.2: A schematic of the experimental setup (adapted from [61]). The translucent blue area represents the (approximately) two-dimensional region with flowing soap film.

had a total of nine different yokes available, corresponding to the amplitude values $A \in \{1.0\text{mm}, 1.5\text{mm}, 2.0\text{mm}, 2.5\text{mm}, 3.0\text{mm}, 3.5\text{mm}, 4.0\text{mm}, 4.5\text{mm}, 5.0\text{mm}\}$. The corresponding normalised amplitude values were calculated as $A^* = A/4\text{mm}$.

The oscillation frequency was changed by varying the amount of power provided to the motor. The corresponding frequency value, f, was determined by using a Fast Fourier Transform (FFT) on the frame region containing the oscillating disk. The natural frequency of vortex shedding from a stationary cylinder/disk, f_{St}, depends on the background flow speed of the soap film, U. It was not possible to control the background flow speed precisely enough by varying the valve at the outlet. As a result, f_{St} varies from experiment to experiment. To determine f_{St} in a given experiment, we recorded a 10 seconds video of the flow past the stationary disk right before starting the oscillations. The vortex shedding frequency of the stationary disk was then estimated by using a FFT on a small frame region containing a part of the wake pattern. By assuming that f_{St} remain constant when the disk is oscillated immediately after the recording of the stationary disk, the frequency ratio was computed as $f^* = f/f_{St}$.

In a flowing soap film, the viscosity ν depends strongly on the thickness of the film [52]. For the very thin films generated in soap film experiments, the thickness is difficult to measure and hence it is difficult to calculate the Reynolds number accurately enough. For the results presented in this chapter, we estimate the Reynolds number by following the approach suggested in [21]. First we determine the Strouhal number $St = f_{St}D/U$, and then we estimate the Reynolds number using an empirically-known relationship between Re and St. We have already described how we find the value of f_{St}, but to calculate the Strouhal number we also need to determine the background flow speed U.

The background flow speed in a flowing soap film is often measured directly using Particle Tracking Velocimetry (PTV), where particles are seeded in the soap film solution and the individual particles are tracked. Since the seeded particles become visible in the soap film visualisation, we found it impractical to measure the flow speed when conducting the oscillation experiments. Instead we conducted a series of 55 experiments with a stationary disk, where we estimated both the flow speed and the vortex shedding frequency in a soap film solution seeded with 10μm-diameter hollow glass spheres. The flow speed was estimated by identifying the particles in successive video frames and computing the average distance travelled by these particle per unit time. The 55 data points from the experiments in our system are shown in the coordinate system in figure 6.3. U and f_{St} are clearly correlated and we found that the relationship can be represented by the linear fit

$$U = (0.0168\text{m})f_{St} + (0.1138\text{m/s}), \tag{6.1}$$

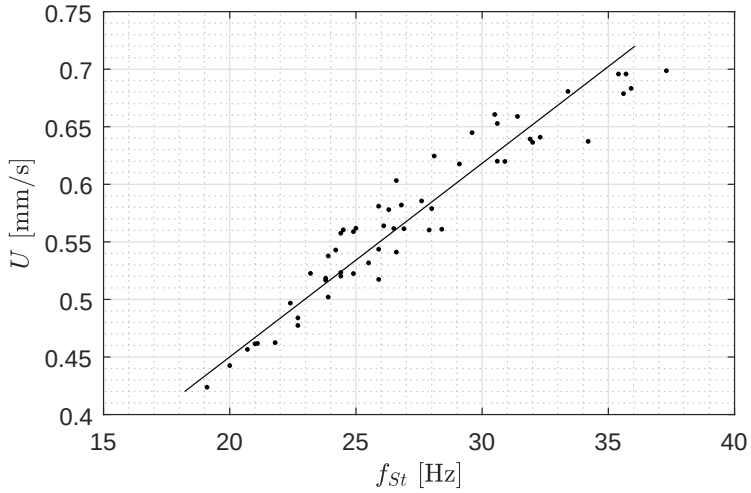

Figure 6.3: Data points representing the estimated vortex shedding frequency f_{St} and background flow speed U in a series of 55 experiments with a stationary disk with diameter $D = 4$mm. The solid line is the linear fit given in (6.1).

with correlation coefficient $R^2 = 0.9136$. For the oscillation experiments, we determine the vortex shedding frequency f_{St} as described above and estimate the background flow speed using the relationship in (6.1). We calculate the Strouhal number $St = f_{St}D/U$ and then we estimate the Reynolds number by using the empirically-known $St - Re$ relationship from [57]

$$St = 0.2731 - \frac{1.1129}{\sqrt{Re}} + \frac{0.4821}{Re}. \tag{6.2}$$

In the numerical study presented in presented in Paper III we describe the problem in terms of the the wavelength ratio, $\lambda^* = \lambda/D$ instead of f^*. Having determined the frequency ratio and the Strouhal number, λ^* can be directly determined as,

$$\lambda^* = \frac{\lambda}{D} = \frac{U}{fD} = \frac{U}{f^* f_{St} D} = \frac{1}{f^* St}. \tag{6.3}$$

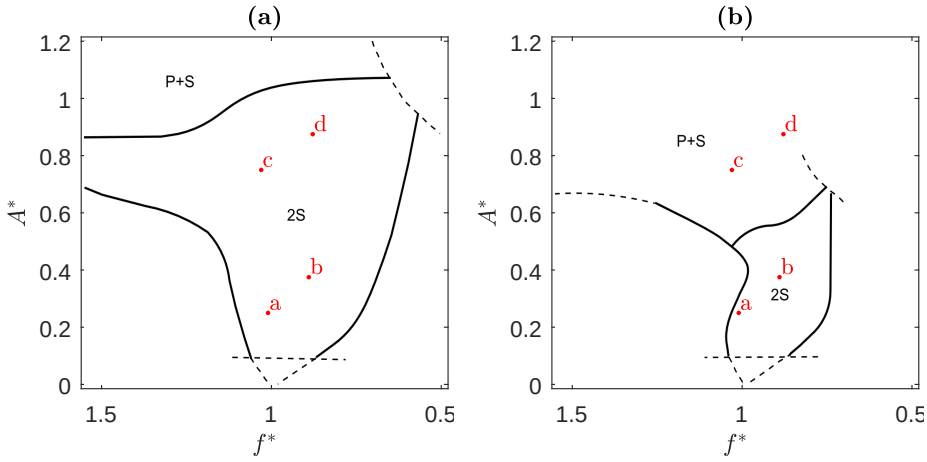

Figure 6.4: Region of the parameter space explored by Leontini *et al.* (2006) for (a) $Re = 100$ and (b) $Re = 300$. The two maps of the flow regimes are redrawn using data from [36]. The red dots marked with a letter correspond to the selected soap film experiments shown in figure 6.5 (a)-(d).

6.2 Results

In this section, we want to investigate how the transition from 2S to P+S mode appears in soap film experiments. As described above, we have only a limited number of amplitude values available in our experimental setup. Furthermore, it is not possible to keep either the oscillation frequency or the Reynolds number constant when we are varying the amplitude. Therefore, it is in no way possible to carry out experiments which can be compared directly with the computational results presented in chapter 5. Instead, we have chosen to present some selected soap film experiments that clearly belong to different flow regimes and confirm that some wake patterns in the transition from 2S to P+S mode have topological variations downstream. We have selected four experiments with increasing amplitude values; $A^* = 0.25, 0.375, 0.75$, and 0.875 and comparable frequency values in the range $0.878 \leq f^* \leq 1.028$. To make it probable that the our two-dimensional flow would resemble the corresponding flow in a three-dimensional setup, we have tried to obtain a Reynolds number that is as low as possible in our soap film experiments. In the selected experiments, the Reynolds numbers are within the range $149.2 \leq Re \leq 161.3$. To our knowledge, there is no comprehensive numerical study of the wake patterns available for $Re \approx 150$. For comparison, the four selected soap experiments are therefore marked on top of the (A^*, f^*) parameter spaces corresponding to numerical studies with

(a) $Re = 100$ and (b) $Re = 300$ (see figure 6.4). The two phase diagrams are redrawn using data from Leontini *et al.* (2006) [36]. They clearly show that the transition from 2S to P+S wake mode occurs at a lower amplitude value when the Reynolds number increases. For simulations with $Re \approx 150$ we therefore expect that the transition is somewhere in between the two cases. This is confirmed by our own numerical simulation in figure 6.6.

To present the results from our soap film experiments, we have selected a snapshot of each of the four experiments, which we consider to be a representative visualisation of the wake pattern. The four snapshots are shown in figure 6.5 (a)-(d) and the corresponding parameter values are noted in the caption of the figure. The wake pattern in figure 6.5(a) has a clean 2S structure with no variations down stream. The experiment presented in figure 6.5(d) is an example of a P+S wake pattern, in which three vortices are shed per oscillation cycle and persist downstream. The very small additional vortices appearing in some oscillation cycles are not part of a regular pattern and we ignore these when we classify the wake pattern as P+S mode. In general, the P+S wakes we observe in the experiments were not as regular as the 2S wake patterns. In the two most extreme cases; (a) and (d), the observed wake structure agree well with our prior expectations based on the comparison with numerical results in figure 6.4. From the results in chapter 5, we expect a 'mixed' wake pattern somewhere in the transition from the case in (a) to the case in (d). The experiments in (b) and (c) have been selected to show some representative examples of the intermediate wake patterns with topological variations downstream. In both cases two pairs of vortices are shed per oscillation cycle resulting in a 2P wake pattern in the near wake. In (b) each pair consists of a weak and a strong vortex, the two weaker vortices does not persist downstream which result in a 2S wake pattern in the mid/far wake. This type of pattern is denoted as a 'weak 2P' mode in the studie described in [61]. In (c), one of the secondary vortices persist in the downstream wake, resulting in a P+S pattern in the mid/far wake.

It is important to keep in mind that the repeatable wake patterns in soap film experiments are not completely periodic. In the experiments we observe that the soap film is quite sensitive to perturbations and would often become significantly distorted in the mid/far wake. The selected snapshots are considered to be a visualisation of the flow, which is representative for the pattern we see in the majority of the recorded video. Furthermore, we have no way of detecting exactly how far downstream in the wake the secondary vortices disappear. One could therefore argue that it is too detailed to use our extended classification when specifying the type of wake pattern in the soap film experiments. If we were to try anyway, we would classify the four wakes patterns in 6.5 (a)-(d) as $(2S)^{\infty}$, $(2P)^3(P+S)^2(2S)^{\infty}$, $(2P)^3(P+S)^{\infty}$ and $(P+S)^{\infty}$, respectively.

As mentioned, it has not been possible to carry out a comprehensive study of the

transition from 2S to P+S mode with the available experimental setup. However, although we can not directly compare with the results in chapter 5, the few examples we have presented here are consistent with the main conclusions. We see that the change in wake structure does not occur as a single abrupt change but we observe a 'transition zone' where the wake has topological variations downstream. The transition is therefore not as simple as indicated by the boundaries in figure 6.4, and the experiments confirm that an extended classification of the wake pattern is needed to describe the topological variations downstream. We still expect that the break in symmetry occur as a result of a pitchfork bifurcation somewhere in the transition zone. However, this assumption has not been possible to confirm solely on the basis of our experiments.

One of the advantages of performing numerical simulations rather than experiments is that the parameter values always can be selected with a desired accuracy. We have used this opportunity to make a direct comparison between the four selected soap film experiments and numerical simulations performed at the exact same parameter values. The simulations were performed with the numerical method described i Paper III. A single snapshot from each simulation is shown in figure 6.6 (a)-(d) and the corresponding parameter values are noted in the caption of the figure. Even though we only show a single snapshot here, we know the entire periodic development of the wake and we can classify the wake pattern by monitoring the cusp bifurcations in the vorticity field as described in Paper III. The wake pattern in figure 6.6(a) has a clear 2S structure with no variations downstream and we would classify the pattern as $(2S)^{\infty}$. In the second example in (b) we see that two weaker vortices are formed in the 'tail' of vorticity behind the two main vortices, however, these quickly disappear again and we classify the pattern as $(2S)^2(2P)^1(2S)^{\infty}$. The simulation represented by the snapshot in (c) has a wake pattern where two pairs of vortices are shed per oscillation cycle. The two weaker vortices does not persist downstream but they reappear in the 'tail' of vorticity behind the main vortices, resulting in a $(2P)^2(2S)^2(2P)^{\infty}$ wake pattern. The last example in (d) show a wake pattern where the main vortices forms a P+S structure that persist down stream. Just like in the corresponding soap film experiment, we observe some small extra vortices. Since we are sure that the simulation is fully converged to a periodic solution, these extra vortices are actually a part of the 'true wake pattern'. If we were to use our classification method rigorously, the pattern would be therefore be classified as $(P+S)^1(P+2S)^2(P+S)^1(P+2S)^2(P+S)^{\infty}$.

When we compare the patterns in figures 6.5 and figure 6.6, we see many similarities especially in the most extreme cases; (a) and (d). In the two intermediate cases; (b) and (c), we observe topological variations downstream in the soap film experiments as well as in the numerical simulations but the final classifications turn out to be very different. This is because the computed vorticity fields

satisfy the (anti-)symmetry condition,

$$\omega(x, y, t) = -\omega(x, -y, t + 1/2), \tag{6.4}$$

as described in Paper III. This (anti-)symmetry is not structurally stable and an arbitrary perturbation of the soap film system could easily break the symmetry slightly. This is exactly what we see in the example in figure 6.5 (b) where one of the weaker vortices disappears before the other. We first see a clear break of symmetry in the last example where $A^* = 0.875$, and we therefore believe that the expected symmetry-breaking pitchfork bifurcation occurs for parameter values somewhere between example (c) and (d).

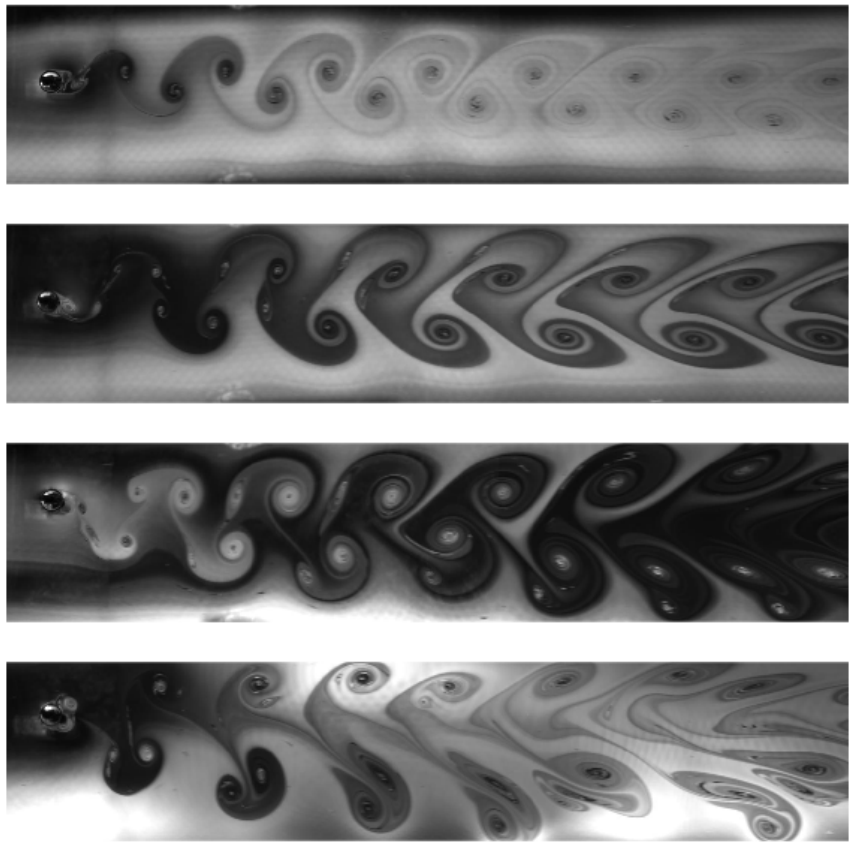

Figure 6.5: Visualisations of the wake behind the oscillating disk in soap film experiments with the following parameter values:
(a) $A^* = 0.250$, $f^* \approx 1.010$ (or $\lambda^* \approx 5.27$) and $Re \approx 161.3$.
(b) $A^* = 0.375$, $f^* \approx 0.891$ (or $\lambda^* \approx 6.06$) and $Re \approx 149.2$.
(c) $A^* = 0.750$, $f^* \approx 1.028$ (or $\lambda^* \approx 5.20$) and $Re \approx 155.9$.
(d) $A^* = 0.875$, $f^* \approx 0.878$ (or $\lambda^* \approx 6.06$) and $Re \approx 159.5$.

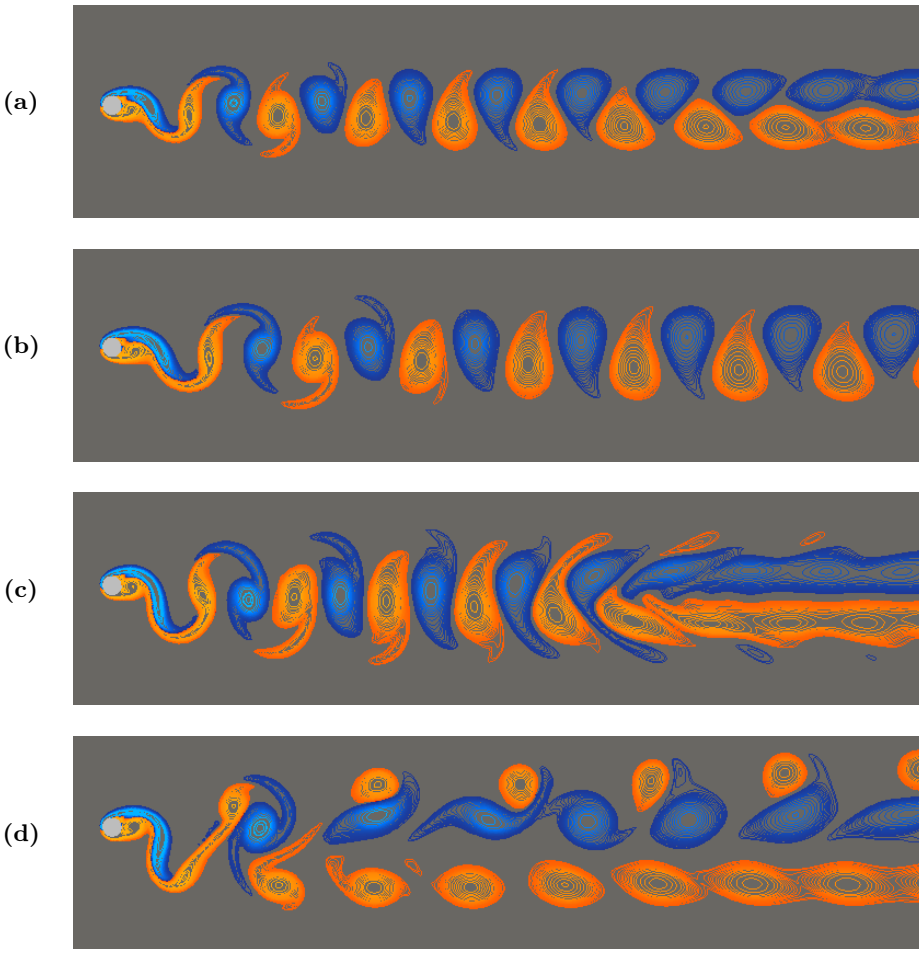

Figure 6.6: Snapshots of the vorticity field computed for following parameter values:
(a) $A^* = 0.250$, $\lambda^* = 5.27$ and $Re = 161.3$.
(b) $A^* = 0.375$, $\lambda^* = 6.06$ and $Re = 149.2$.
(c) $A^* = 0.750$, $\lambda^* = 5.20$ and $Re = 155.9$.
(d) $A^* = 0.875$, $\lambda^* = 6.06$ and $Re = 159.5$.

Chapter 7

Summary and future work

In this thesis, we have described a systematic approach for analysing spatial structures in fluid dynamical problems at a great level of detail. Although the two vortex criteria we have used in our studies are very different, the overall approach is the same; the structural changes are identified as topological bifurcations of a quantity describing the flow structure. We therefore believe that a similar approach can be applied when the flow structure is defined in a different way. Numerical simulations of a fluid dynamical problem can only give us information that is discretized with respect to the parameters in the problem. In order to construct a bifurcation diagram describing a given problem, it is therefore necessary to know the possible structural changes that may occur when a given number of parameters are varied. A bifurcation theory, like the one we developed for the Q-criterion, provides a list of the possible vortex bifurcation events and hence it facilitate the construction of a bifurcation diagram.

In this thesis, we have focused on developing theory and applying the results to some relatively simple case studies. An obvious opportunity for future studies would be to use our approach to analyse fluid dynamical problems that are more complex and depends on more external parameters. Depending on the complexity of the problem, it may be necessary to expand our theory to include bifurcations of higher codimension.

Another obvious research question is to consider fluid dynamical problems in three dimensions. In a three-dimensional flow, the vorticity field is a vector field and it is therefore not meaningful to identify vortices as extremal points of the

vorticity field. A natural generalisation would be to consider the maxima of the magnitude of the vorticity field $|\boldsymbol{\omega}|$. Jeong & Hussain [30] discuss, however, that this definition can be misleading when a vortex is present in a three dimensional a shear flow.

In contrast to the vorticity criterion, the Q-criterion is three-dimensional in its general form and it is therefore easier to generalize our bifurcation theory for Q-vortices to three-dimensional flows. In this case the zero contours of Q are surfaces in three dimensions and the three-dimensional version of the Morse Lemma should be applied in the analysis. A three dimensional bifurcation theory for Q-vortices would also be directly applicable for vortices defined by the Δ-criterion, the λ_2-criterion [30] or any other criterion that define a vortex as a region where some scalar valued function is positive.

There is no simple connection between vortices defined as extremal points of vorticity and vortices defined by the Q-criterion. In this thesis, we do not try to answer the question of how to define a vortex in a flow. Instead, we introduce an approach for giving a detailed analysis of the vortex structure once a specific criterion has been selected. The results in section 3.3 illustrate that a topological description of a fluid dynamical problem may be highly dependent on the chosen definition of a vortex.

Bibliography

[1] M. Andersen, C. Schreck, J. Schmidt Hansen, and M. Brøns. Vorticity topology of vortex pair interactions at low Reynolds numbers. *European Journal of Mechanics, B/fluids*, 74:58–67, 2019.

[2] G. O. Antoine, E. De Langre, and S. Michelin. Optimal energy harvesting from vortex-induced vibrations of cables. *Proceedings of the Royal Society A: Mathematical, Physical and Engineering Sciences*, 472:20160583, 2016.

[3] H. Aref, M. A. Stremler, and F. L. Ponta. Exotic vortex wakes-point vortex solutions. *Journal of Fluids and Structures*, 22(6-7):929–940, 2006.

[4] M. I. Auliel, F. Castro, R. Sosa, and G. Artana. Gravity-driven soap film dynamics in subcritical regimes. *Physical Review E - Statistical, Nonlinear, and Soft Matter Physics*, 92(4):043009, 2015.

[5] P. G. Bakker. *Bifurcations in Flow Patterns : Some Applications of the Qualitative Theory of Differential Equations in Fluid Dynamics*. Klüwer Academic Publishers, 1991.

[6] A. Balci, M. Andersen, M. C. Thompson, and M. Brøns. Codimension three bifurcation of streamline patterns close to a no-slip wall: A topological description of boundary layer eruption. *Physics of Fluids*, 27(5):053603, 2015.

[7] The USGS EROS Data Center Satellite Systems Branch. *Alexander Selkirk Island*. https://earthobservatory.nasa.gov/images/2613/von-karman-vortices, 1999.

[8] L. K. Brandt and K. K. Nomura. Characterization of the interactions of two unequal co-rotating vortices. *Journal of Fluid Mechanics*, 646:233–253, 2010.

[9] M. Brøns. Streamline topology: Patterns in fluid flows and their bifurcations. *Advances in Applied Mechanics*, 41:1–42, 2007.

[10] M. Brøns and A. Bisgaard. Bifurcation of vortex breakdown patterns in a circular cylinder with two rotating covers. *Journal of Fluid Mechanics*, 568:329–349, 2006.

[11] M. Brøns and A. V. Bisgaard. Topology of vortex creation in the cylinder wake. *Theoretical and Computational Fluid Dynamics*, 24(1-4):299–303, 2010.

[12] M. Brøns and J. N. Hartnack. Streamline topologies near simple degenerate critical points in two-dimensional flow away from boundaries. *Physics of Fluids*, 11(2):314–324, 1999.

[13] M. Brøns, A. R. Nielsen, M. Andersen, and M. Heil. Dynamics and bifurcations of critical points of vorticity. *In preparation*, 2021.

[14] M. Brøns, L. P. K. Voigt, and J. N. Sørensen. Streamline topology of steady axisymmetric vortex breakdown in a cylinder with co- and counter-rotating end-covers. *Journal of Fluid Mechanics*, 401:275–292, 1999.

[15] J. M. Chomaz. The dynamics of a viscous soap film with soluble surfactant. *Journal of Fluid Mechanics*, 442:387–409, 2001.

[16] Y. Couder and C. Basdevant. Experimental and numerical study of vortex couples in two-dimensional flows. *Journal of Fluid Mechanics*, 173:225–51, 1986.

[17] A. Davey. Boundary-layer flow at a saddle point of attachment. *Journal of Fluid Mechanics*, 10(4):593–610, 1961.

[18] W. R. Dean. Note on the motion of liquid near a position of separation. *Proceedings of the Cambridge Philosophical Society*, 46(2):293–306, 1950.

[19] T. L. Doligalski and J. D. A. Walker. The boundary-layer induced by a convected two-dimensional vortex. *Journal of Fluid Mechanics*, 139:1–28, 1984.

[20] D. G. Dritschel and D. W. Waugh. Quantification of the inelastic interaction of unequal vortices in 2-dimensional vortex dynamics. *Physics of Fluids A-fluid Dynamics*, 4(8):1737–1744, 1992.

[21] M. Gharib and P. Derango. A liquid-film (soap film) tunnel to study two-dimensional laminar and turbulent shear flows. *Physica D*, 37(1-3):406–416, 1989.

[22] J. J. J. Gillissen, A. Vilquin, H. Kellay, R. Bouffanais, and D. K.P. Yue. A space-time integral minimisation method for the reconstruction of velocity fields from measured scalar fields. *Journal of Fluid Mechanics*, 854:348–366, 2018.

[23] G. Haller. An objective definition of a vortex. *Journal of Fluid Mechanics*, 525:1–26, 2005.

[24] G. Haller, A. Hadjighasem, M. Farazmand, and F. Huhn. Defining coherent vortices objectively from the vorticity. *Journal of Fluid Mechanics*, 795:136–173, 2016.

[25] J. N. Hartnack. Streamline topologies near a fixed wall using normal forms. *Acta Mechanica*, 136(1-2):55–75, 1999.

[26] J. N. Hartnack. *Structural Changes in Incompressible Flow Patterns.* PhD thesis, Department of Mathematics,Technical University of Denmark, 1999.

[27] M. Heil, J. Rosso, A. L. Hazel, and M. Brøns. Topological fluid mechanics of the formation of the Kármán-vortex street. *Journal of Fluid Mechanics*, 812:199–221, 2017.

[28] J. C. Heinz, N. N. Sørensen, F. Zahle, and W. R. Skrzypinski. Vortex-induced vibrations on a modern wind turbine blade. *Wind Energy*, 19(11):2041–2051, 2016.

[29] J. C. R Hunt, A. A. Wray, and P. Moin. Eddies, streams, and convergence zones in turbulent flows. Tech. Rep. CTR-S88, Center for Turbulence Research, Stanford University, 1988.

[30] J. Jeong and F. Hussain. On the identification of a vortex. *Journal of Fluid Mechanics*, 285:69–94, 1995.

[31] F. Jing, E. Kanso, and P. K. Newton. Viscous evolution of point vortex equilibria: The collinear state. *Physics of Fluids*, 22(12):123102, 2010.

[32] F. Jing, E. Kanso, and P. K. Newton. Insights into symmetric and asymmetric vortex mergers using the core growth model. *Physics of Fluids*, 24(7):073101, 2012.

[33] J. Kasten, J. Reininghaus, I. Hotz, H. C. Hege, B. R. Noack, G. Daviller, and M. Morzyński. Acceleration feature points of unsteady shear flows. *Archives of Mechanics*, 68(1):55–80, 2016.

[34] S. C. Kim and S. I. Sohn. Interactions of three viscous point vortices. *Journal of Physics A: Mathematical and Theoretical*, 45(45):455501, 2012.

[35] B. Lautrup. *Physics of continuous matter, second edition: Exotic and everyday phenomena in the macroscopic world*. CRC Press, 2011.

[36] Justin S. Leontini, B. E. Stewart, M. C. Thompson, and K. Hourigan. Wake state and energy transitions of an oscillating cylinder at low reynolds number. *Physics of Fluids*, 18(6):067101, 2006.

[37] T. Leweke, S. Le Dizès, and C. H. K. Williamson. Dynamics and instabilities of vortex pairs. *Annual Review of Fluid Mechanics*, 48(1):507–541, 2016.

[38] J. E. Marsden, R. Abraham, and T. S. Ratiu. *Manifolds, tensor analysis, and applications*, volume 2. Addison-Wesley, 1983.

[39] P. S. Matharu, A. L. Hazel, and M. Heil. Spatio-temporal symmetry breaking in the flow past an oscillating cylinder. *Journal of Fluid Mechanics*, 918:A42, 2021.

[40] J. D. Meiss. *Differential Dynamical Systems (Monographs on Mathematical Modeling and Computation)*. Society for Industrial and Applied Mathematics, 11 2007.

[41] P. Meunier, U. Ehrenstein, T. Leweke, and M. Rossi. A merging criterion for two-dimensional co-rotating vortices. *Physics of Fluids*, 14(8):2757–2766, 2002.

[42] P. Meunier, S. Le Dizès, and T. Leweke. Physics of vortex merging. *Comptes Rendus Physique*, 6(4-5):431–450, 2005.

[43] T. L. Morse and C. H. K. Williamson. Employing controlled vibrations to predict fluid forces on a cylinder undergoing vortex-induced vibration. *Journal of Fluids and Structures*, 22(6-7):877–884, 2006.

[44] NASA Langley Research Center (NASA-LaRC). *Wake Vortex Study at Wallops Island*. https://commons.wikimedia.org/wiki/File:Airplane_vortex_edit.jpg/media/File:Airplane_vortex.jpg, 1990.

[45] A. R. Nielsen. Dynamics and topology of boundary layer eruption. Master's thesis, Department of Mathematics,Technical University of Denmark, 2017.

[46] A. R. Nielsen, M. Andersen, J. S. Hansen, and M. Brøns. Topological bifurcations of vortex pair interactions. *Journal of Fluid Mechanics*, 917:A11, 2021.

[47] A. R. Nielsen, M. Heil, M. Andersen, and M. Brøns. Bifurcation theory for vortices with application to boundary layer eruption. *Journal of Fluid Mechanics*, 865(865):831–849, 2019.

[48] F. L. Ponta and H. Aref. Numerical experiments on vortex shedding from an oscillating cylinder. *Journal of Fluids and Structures*, 22(3):327–344, 2006.

[49] M. Rivera, P. Vorobieff, and R. E. Ecke. Turbulence in flowing soap films: Velocity, vorticity, and thickness fields. *Physical Review Letters*, 81(7):1417–1420, 1998.

[50] J. W. Rutter. *Geometry of Curves*. Chapman Hall/CRC Mathematics Series. Taylor & Francis, 2000.

[51] T. Schnipper, A. P. Andersen, and T. Bohr. Vortex wakes of a flapping foil. *Journal of Fluid Mechanics*, 633:411–423, 2009.

[52] A.A. Trapeznikov. Application of the method of two-dimensional viscosity and shear strength to the investigation of the structure and composition of two-sided films and surface layers in solutions of soaps and saponins. *Proceedings of the 2nd International Congress on Surface Activity*, page 242–258, 1957.

[53] R. R. Trieling, O. U. Velasco Fuentes, and G. J.F. van Heijst. Interaction of two unequal corotating vortices. *Physics of Fluids*, 17(8):087103, 2005.

[54] Z. U. A. Warsi. *Fluid Dynamics: Theoretical and Computational Approaches, Third Edition*. Mechanical Engineering. Taylor & Francis, 2005.

[55] F. White. *Viscous fluid flow. McGraw-Hill series in mechanical engineering*. McGraw-Hill New York, 1974.

[56] S. Wiggins. *Introduction to Applied Nonlinear Dynamical Systems and Chaos*. Texts in Applied Mathematics. Springer New York, 2003.

[57] C. H. K. Williamson and G. L. Brown. A series in 1/root Re to represent the Strouhal-Reynolds number relationship of the cylinder wake. *Journal of Fluids and Structures*, 12(8):1073–1085, 1998.

[58] C. H. K. Williamson and A. Roshko. Vortex formation in the wake of an oscillating cylinder. *Journal of Fluids and Structures*, 2:355–381, 1988.

[59] C. H.K. Williamson and R. Govardhan. Vortex-induced vibrations. *Annual Review of Fluid Mechanics*, 36(1):413–455, 2004.

[60] H. Wu, D. P. Sun, L. Lu, B. Teng, G. Q. Tang, and J. N. Song. Experimental investigation on the suppression of vortex-induced vibration of long flexible riser by multiple control rods. *Journal of Fluids and Structures*, 30:115–132, 2012.

[61] W. Yang, E. Masroor, and M. A. Stremler. The wake of a transversely oscillating circular cylinder in a flowing soap film at low Reynolds number. *Submitted to Journal of Fluids and Structures*, 2020.

[62] W. Yang and M. A. Stremler. Critical spacing of stationary tandem circular cylinders at Re $\approx$ 100. *Journal of Fluids and Structures*, 89:49–60, 2019.

[63] Y. Zhang, K. Liu, H. Xian, and X. Du. A review of methods for vortex identification in hydroturbines. *Renewable and Sustainable Energy Reviews*, 81:1269–1285, 2018.

[64] Q. Zhong, Q. Chen, H. Chen, and D. Li. A topological method for vortex identification in turbulent flows. *Fluid Dynamics Research*, 49(1):015509, 2017.

[65] J. Zhou, R. J. Adrian, S. Balachandar, and T. M. Kendall. Mechanisms for generating coherent packets of hairpin vortices in channel flow. *Journal of Fluid Mechanics*, 387:353–396, 1999.